An Interferometric Study of Spreading Liquid Films

by

Hossein Pirouz Kavehpour

B.S. Mechanical Engineering
Sharif University of Technology, 1991
M.S. Mechanical Engineering and Applied Mechanics
University of Rhode Island, 1998

Submitted to the Department of Mechanical Engineering
in partial fulfillment of the requirements for the degree of

Doctor of Philosophy in Mechanical Engineering

at the

MASSACHUSETTS INSTITUTE OF TECHNOLOGY

January 2003

Author ....
Department of Mechanical Engineering
January 31, 2003

Certified by..
Gareth H. McKinley
Professor of Mechanical Engineering
Thesis Supervisor

Accepted by ....
Ain A. Sonin
Professor of Mechanical Engineering
Graduate Officer

An Interferometric Study of Spreading Liquid Films

by

Hossein Pirouz Kavehpour

Submitted to the Department of Mechanical Engineering
on January 31, 2003, in partial fulfillment of the
requirements for the degree of
Doctor of Philosophy in Mechanical Engineering

Abstract

Moving contact line problems involving polymeric materials and other complex fluids are encountered in many applications such as coating flows, gravity-driven drainage, and spin-coating operations. Viscous, capillary, inertial and gravitational forces can all be important in these flows depending on the scale and speed of the spreading process. In this research, a number of benchmark problems involving moving contact lines of viscous Newtonian and non-Newtonian polymeric fluids have been studied using non-invasive optical techniques.

A detailed study of viscous Newtonian and non-volatile liquids spreading on smooth horizontal and inclined substrates is presented. A phase-modulated interference microscope was used to enable the simultaneous measurement of both the inner (microscopic) length scale and the outer (macroscopic) flow scale in addition to the intermediate matching region. The resulting measurements of both the apparent contact angle and lateral scale of the precursor wetting film agree quantitatively with theoretical predictions for the spreading of a van der Waals fluid over a wide range of capillary numbers ($10^{-6} < Ca < 10^{-1}$). It is also shown that the dynamic contact angle of a perfectly wetting Newtonian fluid is not only a function of the capillary number (the Hoffman-Voinov-Tanner law), but also depends on a logarithmic correction to this relationship, which is often overlooked. It is shown that both the microscopic and macroscopic length scales affect this logarithmic correction. Our measurements are in good quantitative agreement with available theoretical predictions.

In addition to the steady, isothermal spreading of fluids, we have studied instabilities of volatile liquid films spreading on thermally conductive surfaces. When a drop of volatile silicone oil is deposited on the surface of a smooth silicon wafer, its thickness decreases with time in a power-law form as it spreads under the action of capillarity. At a critical thickness, traveling waves can be observed on the free surface of the film, and a confocal microscope was used to measure the amplitude, frequency, and non-linear evolution of these waves. We interpret these waves in terms of Marangoni instabilities induced by surface tension gradients close to the contact line, generated by liquid evaporation.

The spreading of highly entangled polymer melts ($Z > 10$) on a solid surface is also considered. Our experiments confirm the existence of a non-Newtonian 'foot' region in the vicinity of the moving contact line for highly entangled polymer melts. Our experimental results of the lateral and vertical scales of this 'foot' are in fair agreement with available theoretical predictions. The transient spreading motion of an ideal elastic 'Boger' fluid (consisting of a dilute solution of high molecular weight polymer dissolved in a viscous Newtonian solvent) is also investigated. It is shown that the spreading rate of this model elastic fluid is smaller than is observed for corresponding Newtonian fluid drops of similar size and viscosity due to the viscoelastic effects. A foot-like structure is detected at the leading edge of the droplet for these unentangled, elastic fluids as well. We argue that this structure arises from large viscoelastic effects and the differential mobility of the large polymer molecules and smaller oligomeric solvent molecules across the solid substrate close to the moving contact line.

Thesis Supervisor: Gareth H. McKinley
Title: Professor of Mechanical Engineering

I dedicate this thesis to my family for all they have taught me:

My mother for striving to excel,
My father for tirelessness,
Kaveh for love of physics,
and,
Siamak for humor.

Acknowledgments

There are a few people I would like to thank for my professional, financial and personal support they have given me through these years.

First, I would like to express my deepest gratitude to my advisor Professor Gareth H. McKinley. This work would not have been possible without his expert advice and patient guidance. It was a privilege for me to work with him.

Without a doubt, the person to whom I owe the largest debt of gratitude is my wife and soul mate, Faranak. She not has only supported me with her love, but also been involved in scientific discussion with me for all these years. I would not be able to fulfill this dream without her.

I would like to thank my family for their support throughout these years. My brother Kaveh and my brother-in-law Farivar support and encouragement enabled me to reach this goal.

Thanks to all my friends in the lab who made the days go by so quickly: Carlos, Christian, Darryl, Freddy, Jeffery, Jeremy, Jonathan, Jose, Karen, Ryan, Suraj, Tim, Virginie and every other member of the Fluid Mechanics Laboratory at MIT. I thank you for your advice, friendship, and listening when I needed someone to talk to. I will never forget my times in the fluids lab.

To my thesis committee, George Barbastathis, Nicolas Hadjiconstantinou, and Ben Ovryn, I would like to thank you for your advice, and discussions. Finally, I thank the NASA Glenn Microgravity Research Program for financial support of my graduate studies.

Contents

List of Figures

List of Tables

Chapter 1

Introduction

Understanding the dynamics of liquids spreading on solids is of importance in a wide variety of industrial applications such as coating processes, soldering technology, and the printing of inks. When two immiscible fluids are brought into contact with a solid substrate, one of the fluids may spread spontaneously to form a thin film. Alternatively, the final state may leave both of the fluids simultaneously in contact with each other and the solid surface at a line of three-phase contact as shown in figure 1-1. This line of three phase contact is usually called the *contact line*, and the angle between the fluid interface and the solid substrate is called the *contact angle*. When one fluid displaces the other, the contact line is considered to move across the surface of the solid. Studies of the motion of a spreading axisymmetric drop on a smooth horizontal substrate provide a good benchmark model for many of these types of problems [69, 35]. The final equilibrium configuration of the drop may be a thin uniform film covering the substrate (perfect wetting), or a drop of finite lateral extent (partial wetting) depending on the relative magnitudes of the interfacial tensions between the solid, liquid and vapor acting at the three phase contact line [2]. Let's define σ_{SL} and σ_{SV} as the surface tensions between the solid and fluid, and solid and vapor, respectively. A force balance in the horizontal direction when the phases are in equilibrium leads to:

$$\sigma_{SV} - \sigma_{SL} = \sigma_{LV} \cos\theta \tag{1.1}$$

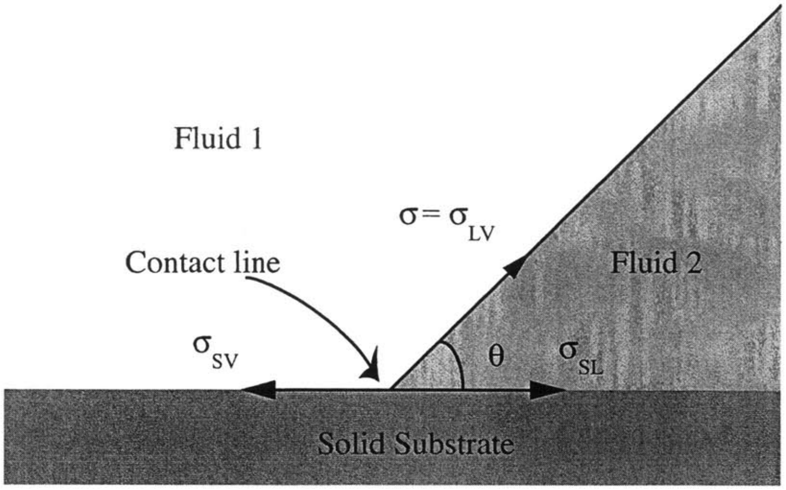

Figure 1-1: Schematic of the three phase contact region and the contact angle.

Equation 1.1 is commonly referred to as the Young equation [121]. An important parameter in spreading is the spreading coefficient S which is the free energy change per unit area for the spreading of liquid film on the solid and is defined as:

$$S = \sigma_{SV} - \sigma_{LV} - \sigma_{SL} \tag{1.2}$$

If $S > 0$, the spreading is spontaneous due to the decreasing of the free energy of the system.

In addition to studies of the final static shape and equilibrium energetic configuration, considerable interest exists in understanding the dynamical process of the spreading of the liquid droplets because, in the majority of commercial processes, a wetting or partially-wetting droplet is rarely deposited in its final equilibrium shape. Most experimental studies of wetting are concerned with the contact angle at a moving contact line. The contact angle associated with the moving contact line, which is advancing across the substrate, is usually called the *dynamic contact angle*, θ_a.

There are several important parameters that govern the dynamical process of spreading and the final shape of the drop. These include the initial drop volume, Ω, the shear viscosity, μ, surface tension, σ, the spreading coefficient S between the liquid and the surface, and the density, ρ, of the liquid plus the surface roughness of substrate, ϵ. Other parameters such as the volatility of the liquid and the temperature

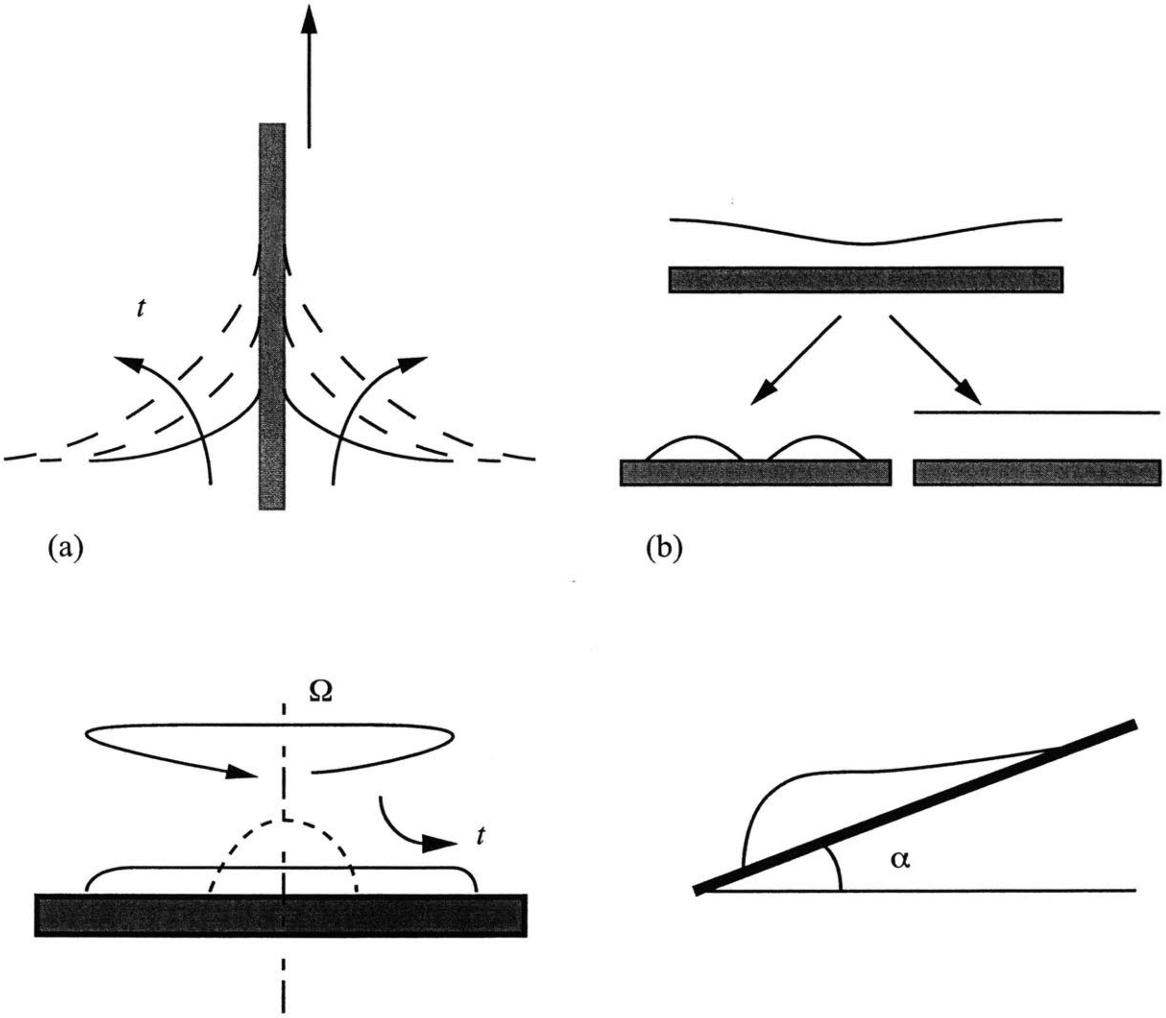

(a)

(b)

(c)

(d)

Figure 1-2: Examples of coating flows in which the motion of the dynamic contact line and non-Newtonian rheology of the fluid are important; (a) dip-coating; (b) leveling and stability of fluid films; (c) spin-coating; (d) drainage of a drop down an inclined plane.

difference between the substrate and the droplet can also be very important since the thermophysical properties of liquids can be a strong function of temperature.

In trying to understand the mechanism by which a liquid wets a solid, the overall theoretical challenge is to interpret the observed wetting behavior in terms of the underlying fluid physics and chemistry of surfaces and spreading fluids. However, this has proved difficult, and despite increasing attention, the problem remains only partially solved. As a result of hydrodynamic studies, it is now widely recognized that it is necessary to relax the classical no-slip boundary condition at the wall and allow limited slip between fluid and solid in the immediate vicinity of the contact line. Without slip, classical continuum hydrodynamics for Newtonian fluid of constant viscosity makes the unacceptable prediction that the force exerted by the fluid on the solid is locally unbounded. Nevertheless, the physical basis for slip and appropriate form of slip condition remain a matter of great speculation.

In many of the commercially important operations indicated in figure 1-2, the rheology of the film coating may be non-Newtonian (i.e. it may exhibit shear-thinning in the viscosity or presence of additional viscoelastic normal stresses) which can have a very important effect in the region of high shear rate and complex two-dimensional flow near the advancing contact line due to the singularity at the moving contact line. Pioneering works on spreading of non-Newtonian fluids such as polymer melts were done by Schonhorn et al.[101] and Ogarrev et al. [83]. Their experimental data have shown different behaviors of non-Newtonian fluids during spreading compared to those observed Newtonian fluids.

A fluid droplet deposited on a substrate rapidly forms a thin film with a lateral extent $R(t)$ greatly exceeding its characteristic thickness $h(t)$ and consequently lubrication analysis can often be used to understand the dynamics of the spreading process. Experiments and analysis show that the lateral size of the spreading droplet and the steady rate of spreading are frequently a power-law function of elapsed time [16]. A common example is the "Hoffman-Voinov-Tanner law" [59, 116, 110] which relates the lateral rate of spreading, $\dot{R}(t)$, to the dynamic contact angle of the interface, θ_a. The power-law exponent characterizing this spreading is a sensitive function

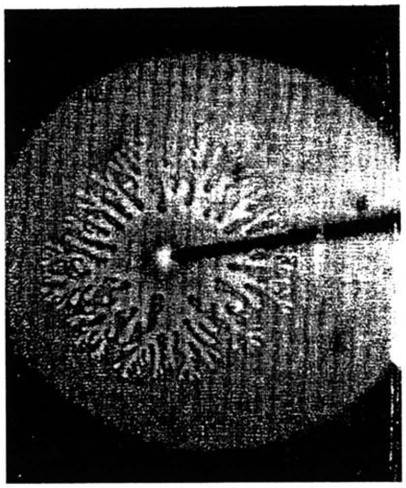

Figure 1-3: Patterns in fingering instabilities on a liquid film with of a surfactant solution on a horizontal surface (from [112]).

of the dominant physical forces (e.g. capillary, viscous, inertia, and gravitational) that are driving and resisting the spreading. A detailed review of these regimes is provided by Oron et al. [84] and will be discussed in chapter 3 of this thesis.

Inertial effects in a spreading film can be neglected if the dimensionless Ohnesorge number, $Oh = \mu/\sqrt{\rho R \sigma}$, which is the ratio of the viscous force to the inertia force in the presence of capillary forces, is much greater than one. The spreading regime then depends on the relative lateral extent, R, and characteristic height of the drop, h, compared to the intrinsic capillary length of the system, $\ell_{cap} = \sqrt{\sigma/\rho g}$, over which gravitational effects are important. Huppert [65] and Cazabat & Cohen Stuart [18] have examined these regimes extensively. When inertial effects are important, different power-laws are obtained. This situation was considered quite early in the context of oil films spreading rapidly on the ocean (see [41, 61] for additional details).

Other experiments have been performed to show the effects of the substrate on the motion of the three-phase contact line and the rate of spreading. For example, Ehrhard [38] investigated the dynamical changes induced by a non-isothermal substrate and Cazabat & Cohen Stuart [18] demonstrated the effect of surface roughness on the power-law spreading of liquid drops. The studies discussed above have all assumed that the spreading profile of the liquid drop is stable in time and remains

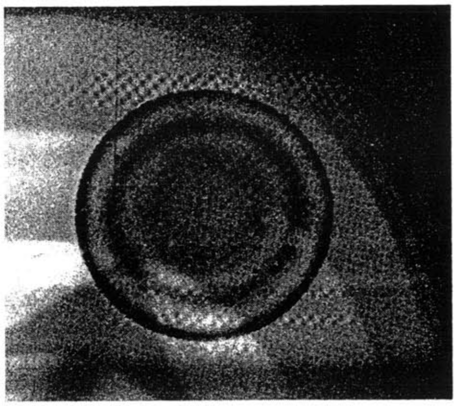

Figure 1-4: Patterns in 'festoon' instabilities on a PDMS film on a horizontal surface (from [96]).

axisymmetric as spreading proceeds. However it is also frequently observed that the spreading film may become unstable and develop a spatially-periodic fingering pattern due to the surface tension gradients induced by surfactants [40, 112] (figure 1-3) and so-called 'festoon instability' as reported by Redon et al. [96]. This instability is due to surface tension gradients caused by higher evaporation rate at the moving contact line (figure 1-4) and leads to elimination or control of such hydrodynamic instabilities is important in painting, coating and inkjet printing which all involve solvent evaporation and mass transfer during the drying process. Another important application of this family of instabilities are the 'orange peel' instabilities which affect the quality of the finished painted surface.

These interfacial instabilities are frequently driven by local lateral variations in the surface tension, $\sigma(x)$, which controls the rate of spreading. Such variations can arise naturally due to the dependence of the surface tension on the temperature field [8] and on the concentration of dissolved solutes. The resulting phenomena are collectively referred to as Marangoni effects [102]. When unsteady flows arise as a result of surface tension gradients dependent on from thermal variations perpendicular to the fluid interface the resulting unsteady flows are usually called Marangoni instabilities. The classical example is Marangoni-Bènard convection [82] as shown in figure 1-5.If instability occurs because surface tension gradients arising from an applied temperature field parallel to the interface of the liquid film, the motion is typically referred to

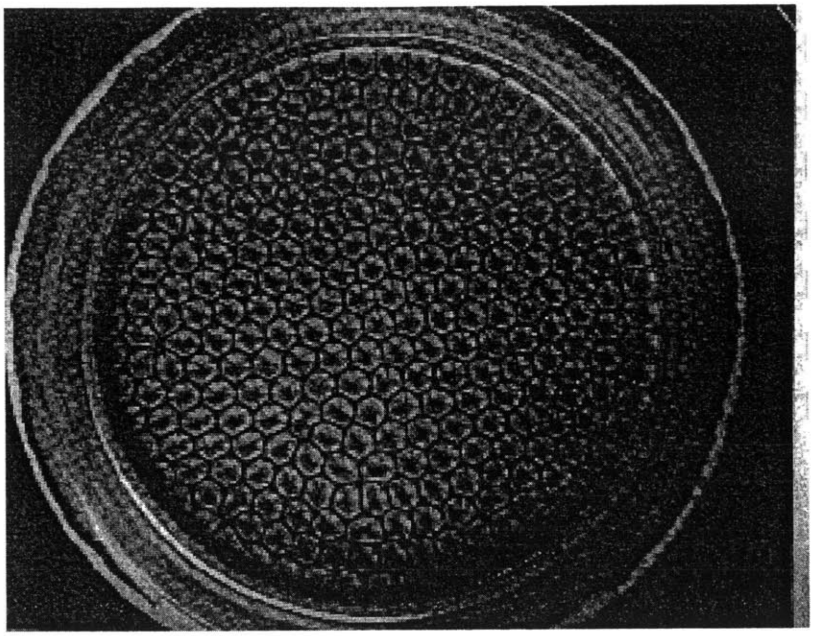

Figure 1-5: Patterns in Bénard instabilities on a liquid film on a horizontal hot substrate (from [34]).

as hydrothermal instability (See for example the studies of Smith & Davis [106, 107]). Detailed reviews of both of these classes of instabilities can be found in [27] and [100]. A separate class of Marangoni flows arises from evaporation. Thermal energy is removed from the liquid resulting in local changes in the temperature and thus also in surface tension. Because the more volatile components of a mixture evaporate most rapidly, concentration gradients also develop. Furthermore, since the evaporative flux is largest near a contact line, spatial gradients in the concentration and/or temperature can drive strong secondary flows. Such evaporatively-driven Marangoni flows lead to formation of coffee rings [31] and also wine tears and tear ducts [60]. These flows also been have been proposed as a way to elongate DNA chains for subsequent sequencing analysis [62, 63](figure 1-6) and enhance heat transfer from menisci in inclined capillary tubes [80].

Such instabilities have been studied in the past in static geometries for which the base flow is stationary and consequently both experimental and theoretical analysis is more tractable. However, evaporatively-driven Marangoni instabilities may also spontaneously arise in spreading droplets, especially if the drops are small so that

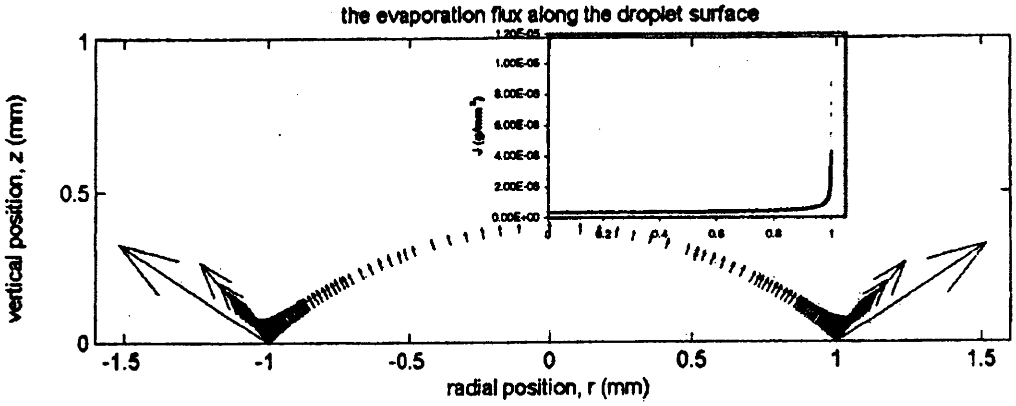

Figure 1-6: Evaporating of spreading droplet on a solid surface. The length and direction of the arrows are the magnitude and direction of the evaporative mass flux from the free surface of the liquid drop. The inset is the mass flux as a function of the radius of the drop (from [63]).

the surface area/volume ratio is large or if the droplets are polymeric in composition and have poor thermal conductivities. We will present studies of these phenomena in chapter 6 of this thesis.

In order to successfully investigate the steady and transient motion of spreading fluids, it is necessary to develop non-invasive techniques for rapidly and accurately probing the surface profiles of fluid microdroplets. Optical techniques are obviously well suited for such tasks. Ellipsometry has been used in the past to spatially resolve the shape and thickness of spreading liquid films but the authors reported major errors, which they speculated arose from surface heating by the laser and subsequently drove Marangoni instabilities [45].

The determination of the static or dynamic shape of a transparent sample on a solid substrate and the thickness of a coating for industrial applications are common goal of many areas of surface science. A detailed understanding of dynamic wetting phenomena and contact angle measurements frequently involve either visual or mathematical extrapolations of the macroscopic interfaces. However, it might seem unwise to expect the extrapolated dynamic contact angle to be preserved at very small distances from the solid surface. Since the force singularity predicted by macroscopic

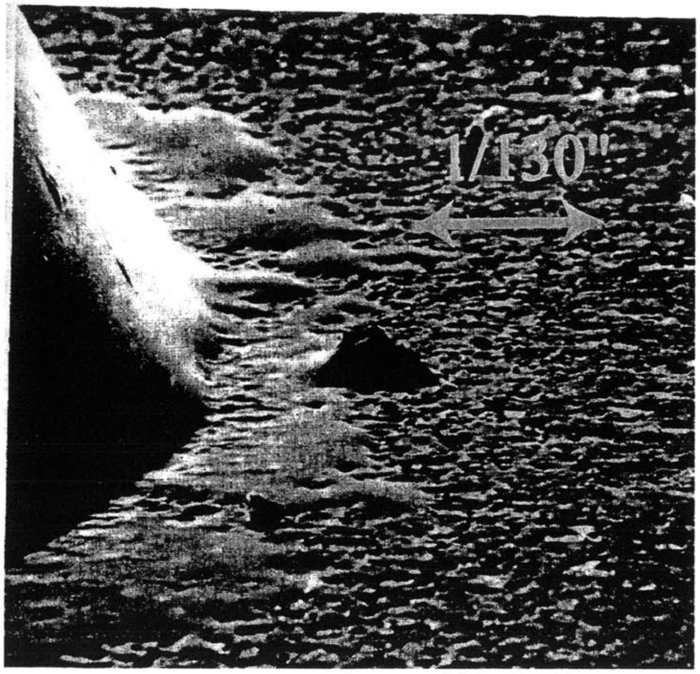

Figure 1-7: Microscopic features close to the contact line [2]. SEM picture of drop of cooled glass on Fernico metal with same coefficient of thermal expansion as glass.

Newtonian hydrodynamic must be relieved on some macroscopic scale, many authors stress this by referring to the observed angle as the apparent dynamic contact angle but their caution derives from theoretical considerations, not experiment. Examined through an optical microscope, the fluid/fluid interface appears to meet the solid surface with a well-defined slope. This is true in both the static and dynamic cases. Observations made with a scanning electron microscope have given important insight into effects of surface roughness and heterogeneity on wetting behavior. Nevertheless, the technique reveals no sudden changes in meniscus curvature down to distances as small as 0.5 μm from a moving wetting line.

When techniques with higher vertical resolution than optical microscopy are used, new microscopic features are detected which a optical microscope can not detect. For systems in which the liquid spreads spontaneously to give a nominally zero contact angle ($S > 0$), optical techniques such as ellipsometry and interferometry have shown *a precursor or primary film* which moves ahead of the main body of liquid [6, 7, 73]. A representative precursor film is shown in figure 1-7. Precursor films form when the intermolecular forces of attraction between the solid and liquid are sufficiently strong to create positive spreading coefficients and disjoining pressures. These related properties provide the driving force for spreading and the released energy is dissipated by viscous drag as the film spreads. The disjoining pressure, which is defined as $\Pi(h) = A/6\pi h^3$ where A is the Hamaker constant and h is the film thickness, is a steep, inverse function of film thickness and therefore creates a correspondingly steep, negative pressure gradient between the bulk liquid and the thin periphery of the film. Hence, the liquid is drawn out of the bulk and into the film (figure 1-8). In cases when the disjoining pressures are large and the viscosity small, the precursor films may spread quite rapidly for significant distances ahead of the bulk liquid.

A simplifying feature of wetting via a precursor film is that flow within the film is virtually one-dimensional. More significantly, the motion of the bulk liquid is decoupled from the wetting line, hence the liquid may be considered to spread across an already pre-wetted surface. Under these conditions, the hydrodynamic equations can be solved explicitly, the velocity dependence of the apparent contact angle is predicted to follow a simple cubic law (the Hoffman-Voinov-Tanner law), $\theta_a^3 \sim U$, where θ_a is the dynamic contact angle and U is velocity of the advancing contact line. The free surface of the spreading drop is governed by a nonlinear differential equation ,$h^2 d^3h/dx^3 = 3\mu U/\sigma$ [30]. This equation has the property that the free surface profile has an inflection point. The existence of this inflection point is a requirement for drops with small apparent contact angles and is discussed in chapter 3.

In this thesis, I will address both the macroscopic and the microscopic characteristics of a spreading drop on a solid substrate through a detailed experimental and theoretical investigation. In chapter 2, two non-invasive optical techniques (confocal surface metrology and phase-shifted laser feedback interferometry) which are used in this research are presented. The theories behind the instruments are summarized and calibration techniques utilized to evaluate the accuracy and repeatability of the optical systems are presented.

In chapter 3, a number of different regimes of spreading of liquid films on a solid substrates are reviewed. When a viscous drop of wetting liquid is placed on a solid

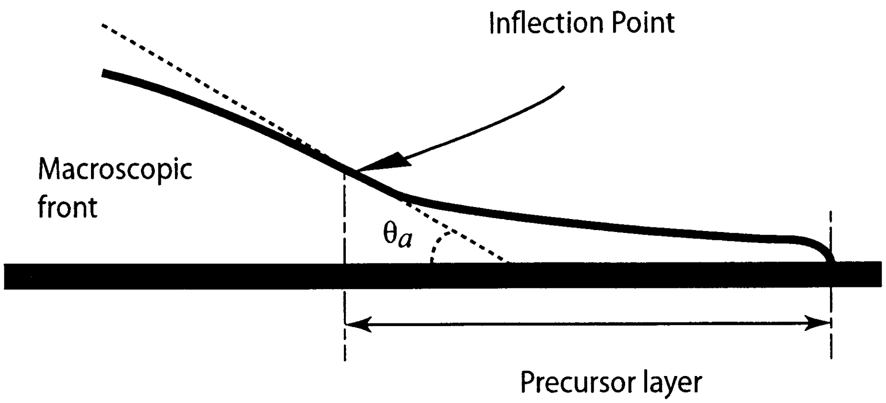

Figure 1-8: Schematic of microscopic features close to the contact line.

surface, the evolution of the droplet shape depends on its physical properties and its initial volume. For the conditions considered in the present study, the impact velocity has negligible effects. The Ohnesorge number, $Oh = \mu/\sqrt{\rho R \sigma}$, scales the forces that resist the spreading. For $Oh \gg 1$ the spreading is resisted primarily by viscous stresses in the fluid, whereas for $Oh \ll 1$ the spreading is retarded principally by fluid inertial effects. The dominant force driving the spreading depends on the relative size of the drop compared to the capillary length, $\ell_{cap} = \sqrt{\sigma/\rho g}$. In chapter 3, we characterize three regimes for the evolution of spreading viscous droplets. The three regimes for a viscous drop with $Oh \gg 1$ depend on the relative magnitudes of the height, $h(t)$, the radius, $R(t)$, as compared to the capillary length. If the characteristic length scale for a drop of volume,Ω is taken as $(\Omega/\pi)^{1/3}$ then an appropriate measure of the dimensionless drop size is $\phi = (\Omega/\pi)^{1/3}/\ell_{cap}$. For small viscous drops ($\phi < 1$), the spreading is driven by capillary force imbalance at the contact line, and resisted by viscosity (for $Oh \gg 1$). However for larger viscous drops ($\phi > 1$), spreading is initially driven by the gravitational body force instead of capillary forces. For $Oh \ll 1$, the spreading is driven by the capillary force and resisted by the inertial force.

Studies of dynamic wetting phenomena and contact angle measurements frequently involve precise measurement of the macroscopic interfaces due to the difficulties inherent in quantitatively measuring the microscopic fluid physics that arise near the moving contact line. We have developed a phase-shifted laser feedback interferometer (psLFI) that can be used to rapidly and non-invasively measure the interfacial profile in the vicinity of moving contact lines of simple Newtonian (chapter $3-5$) and complex fluids (chapter 7). By utilizing an XY stage, we are able to measure the profile of a spreading drops by scanning the free surface of the drop with a constant speed.

The work presented in chapters $3-5$, is intended to constitute a comprehensive set of quantitative measurements to which theoretical analyses can be compared. To meet this goal, a set of experiments have been performed for a variety of liquids.

The test fluids used in chapter 4 are constant-viscosity silicone oils (Gelest Inc.) which perfectly wet the smooth silicon substrate. The viscosities are varied in order to explore a wide range of capillary numbers, Ca. For wetting systems (in which the liquid spreads spontaneously to give a nominally zero contact angle) a precursor or primary film moves ahead of the main body of liquid. By utilizing our optical system, we are able to not only investigate the macroscopic features of the wetting front (such as the dynamic contact angle, θ_a) but also to probe the structure of the microscopic front (precursor layer). In this chapter, the connection between the macroscopic and microscopic regions of the spreading liquid drop is shown. We also show the effect of the capillary number, Ca, on each of the different characteristic length scales that are present in these regions.

In chapter 5, the characteristics of liquid drops spreading on inclined plates are presented. Large drops ($\phi > 1$), spread on inclined plate under the gravitational driving force while viscous forces (and sometimes surface tension forces) resist the spreading. In this chapter we present the experimental and theoretical results of macroscopic features of this process (i.e. the shape of the free surface of the drop) and microscopic features such as the existence of precursor film and dynamic contact angle of the drop.

During our experiments on spreading drops it was noticed that if a drop of volatile wetting liquid was deposited on a surface and allowed to spread, then, after a few seconds, periodic fluctuations at the free surface of the liquid film were detected using the confocal measuring system. In chapter 6, a series of experiments are described which show that these instabilities arise as a result of the volatility of the liquid and the non-uniform evaporation rate across the drop. A linear stability analysis shows that the critical onset conditions for this evaporatively-driven instability can be characterized by a dimensionless interfacial resistance, $\mathcal{R}$ which has to be a larger than a critical value at the onset of instability.

Finally, in chapter 7, the effects of fluid viscoelasticity on the dynamics of the moving contact line are presented. The test fluids used in this chapter are a dilute constant viscosity elastic fluid (i.e. a Boger fluid [13]), and highly entangled polymer melts. As noted above, the importance of non-Newtonian fluids in the coating and paint industries increases the demand for such research studies.

Boger fluids are special dilute solutions which are composed of low concentrations of high molecular weight flexible polymer dissolved in a very viscous, yet Newtonian, liquid, such as a low molecular weight polymer, or oligomer. The high molecular weight of the polymer, combined with the high viscosity of the solvent, boosts the polymer relaxation time into the range of around 1 second or so. With such long relaxation times, strongly nonlinear effects are brought into the range of shear rates of conventional torsional-flow rheometers and typical spreading processes. Boger fluids have been extensively used as model fluids to investigate complex viscoelastic flows, but this is the first study of free surface spreading flows using such fluids.

Finally, at higher concentrations or in the melt state, fluids containing long polymer molecules become extremely viscous due to entanglement. At a characteristic molecular weight, denoted M_c, the shear viscosity begins to rise more rapidly than linearly with molecular weight. Below M_c, the zero-shear viscosity is found to depend roughly linearly on molecular weight as expected by the Rouse theory [71], while above M_c it rises with a much higher power-law exponent (typically $\eta \sim M_w^{3.4}$). The steep increase of viscosity with molecular weight for $M > M_c$ is caused by entanglements, which are topological restrictions on molecular motion resulting form the fact that the individual chains cannot pass through each other. As a result if these entanglements, a long molecule surrounded by other such molecules cannot move very far in directions perpendicular to its own molecular contour. Therefore, molecular diffusion or relaxation is limited to a snake-like motion called reptation [28].

We show that during the spreading of these fluids, there exist an additional regime (a so called 'foot region') at the vicinity of the moving contact line as predicted by Brochard & de Gennes [16] for highly entangled polymer melts spreading on a solid surface. Comparison between the available theoretical predictions and our experimental results is also presented. Finally, the effects of viscoelasticity in the wetting process and on the profile of spreading drop near the moving contact line are presented.

Chapter 8 summarizes the contributions of this thesis to the physics of wetting and moving contact lines and to the understanding of the spreading behavior of Newtonian and non-Newtonian fluids, concluding with some comments on potential future research directions.

Chapter 2

Non-invasive optical measurement Techniques

2.1 Introduction

Characterization of the profile of a solid surface, measurement of amplitude and frequency measurement of waves and disturbances on vibrating surfaces, fluid flow characterization, and measurement of flame velocity in combustion chamber are examples of the use of optical techniques for fluid flow applications in scientific and industrial research. Optical techniques are usually preferred to other conventional methods for following reasons:

- High spatial and temporal resolution of the optical techniques as compared to other methods.

- Optical methods are usually non-invasive. This is a huge advantage since one can operate the measurement system without affecting the dynamics of the experiment.

- Optical techniques can be used for almost any material. There are typically no limitation for electrical conductivity, thermal conductivity, and other physical properties of the sample.

- Dynamic range of optical methods are much higher than other methods.
- Compatibility of these systems to be a part of a feedback control system due to the short response time of these systems..

Among all of the applications for optical techniques, our specific interest in this thesis is to select a system with ability to measure the characteristics of a spreading liquid drop on a solid surface. These features as mentioned in the previous chapter, have a wide range in size (from nanometers to hundreds of microns in thickness) and time scale of the phenomena can be as small as milliseconds. In the following section, these features and commonly used measurement techniques are reviewed.

2.1.1 Measurement methods for spreading liquid films

Since the early 20th century, a number of methods have been used to characterize the liquid spreading phenomena. Important features of interest for spreading drops include the radius of drop, R, the local thickness of drop, h, and the dynamic contact angle, θ_a. Direct imaging of drop was the first method used to study the spreading phenomena. Using photographic techniques, one would take pictures of the drop over a span of time and from those photos the radius $R(t)$ and the surface profile, h, were measured. The dynamic contact angle θ_a were calculated by dedifferentiation of the regression fit to for $h(x)$ at the point where $h = 0$ [1]. This method has some limitations that have made scientists look for alternative methods. Local thickness of drop could not be derived from these photos and contact angle measurements were very inconsistent. As it will be explained in detail in chapter 4, the profile of free surface of the drop does not follow the same relation as the macroscopic part of it due to the long-range forces. Therefore, calculating the contact angle from a global curve fit would not yield an accurate value.

Later on, scientists came up with other methods to measure these desired features. The capacitance probe technique was developed which is based on the differing electrical properties of the substrate and the liquid. By producing an electrical potential between the substrate and a probe, one can calibrate the thickness of a liquid as

Table 2.1: Capability of different optical measurement systems.

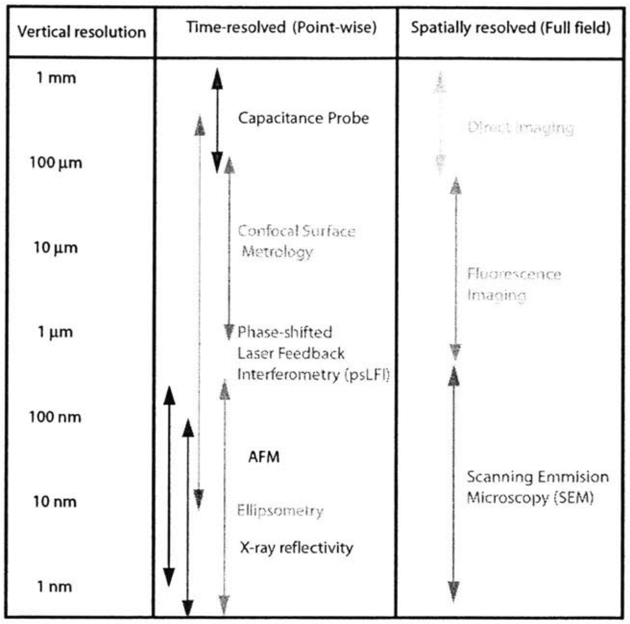

it passes between two electrodes by measuring the capacitance of the system as the function of time. This methods has a very good vertical resolution ($\sim 100\mu$m) [70], however there are several issues regarding the lateral resolution: in particular lateral resolution of this system is strong function of the size of the probe which is usually on the order of 10mm. Also electrical properties of substrate and spreading liquid can effect the measurements.

Methods such as Atomic Force Microscopy (AFM) [94, 42], ellipsometry [7], and X-ray reflectivity [26] have also been used in recent years. In table 2.1, the dynamic range of some of the optical methods commonly used for probing the shape and size of spreading liquid droplets have been compared. As indicated, systems such as direct imaging or capacitance probe do not have a good vertical resolution. Also systems like ellipsometry or AFM, have a very good vertical resolution but what they lack is dynamic range. These system can not measure features larger than 1μm.

An ideal selection for an instrument for liquid film characterization is one which is non-invasive, with high lateral and temporal resolution, and very broad dynamic

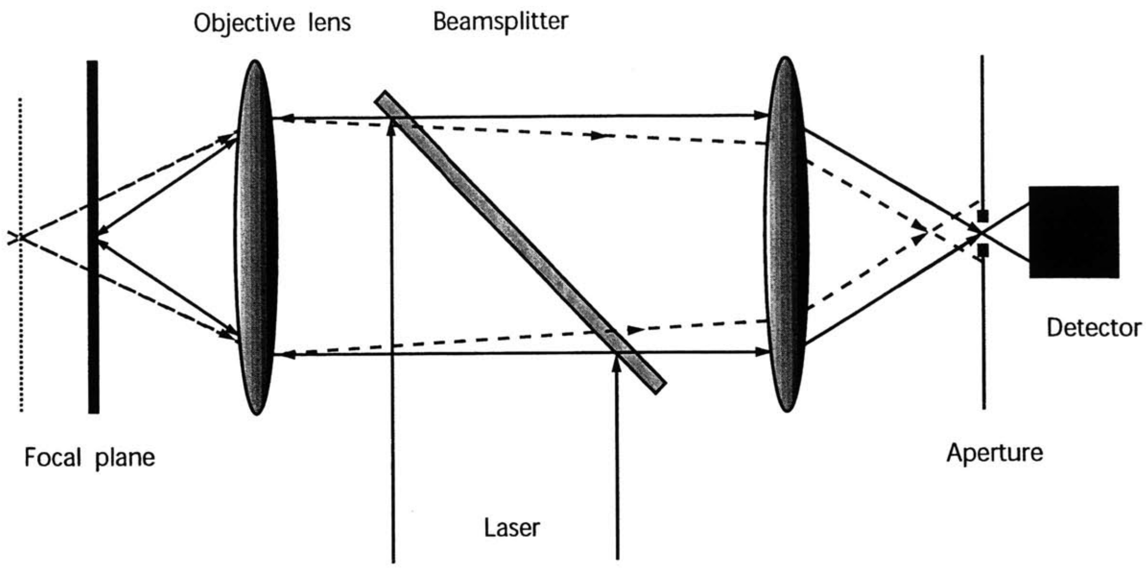

Figure 2-1: The schematic of a confocal system.

range. Such a system not only enable the user to measure the radius and thickness of the drop at any location, but also the variation of these parameters in time can be quantified. As seen in table 2.1, the psLFI system has a wide range of measurement ($1\text{nm} \leq h \leq 500\mu\text{m}$) and high vertical and lateral resolution.

For my experiments, I have used two optical systems:

(i) a laser confocal displacement meter.

(ii) a phase-shifted laser feedback interferometer.

In the following sections these systems are described in detail.

2.2 Laser confocal displacement meter

2.2.1 The confocal principle

Confocal microscopy is a very common technique for high-resolution optical measurements and is utilized in many applications from non-invasive study of biological tissues to measurements of surface roughness [23, 113, 114].

The basic optical principle behind a confocal laser microscope is to scan the target with an illuminating spot, and at the same time have a small detector aperture follow that illuminating spot. This is usually achieved by having a laser as the illumination source and placing a pinhole or other small aperture in front of the detector. A schematic of a simplified optical path can be seen in figure 2-1. The laser beam enters from below in the center of this figure. It is first reflected to the left by a beamsplitter. Then the laser beam focused to a spot by a microscope objective lens. An illuminating spot is formed in the focal plane of the objective. Reflected light travels through the objective lens and most of it passes through the beam splitter. One or more optical lenses focus the light onto the detector aperture. The path indicated with dashed lines shows how light from out of focus objects propagates through the optical system. In this configuration the illuminating spot is defocused, thus illuminating a larger area with a weaker intensity. This is indicated at the left of the figure with the dotted focal position within the specimen. The reflected light takes a different path through the objective lens, beamsplitter and the detector aperture. In this way the depth discriminating properties of the system are achieved. Light from out of focus parts of the specimen give rise to little or no signal from detector.

This principle is utilized together with addition of moving parts and a feedback control system to construct the laser confocal displacement meter. This system is based on a dynamic focus-detection technique together with a closed-loop feedback system. This system differs from a conventional optical or confocal microscope in that it illuminates and images the sample one point at a time through a pinhole. A laser beam that passes through the beamsplitter is focused by a high numerical aperture objective lens to a diffraction-limited spot at the focal plane. If the light spot is focused on a surface by adjusting the objective lens vertically during the scanning process, then the displacement of the objective lens determines the vertical dimension of the surface topography. In the present system, the objective lens is dynamically refocused by a tuning fork in order to automatically maintain an optimal focus of the laser spot on the surface. Whenever the surface is in focus, the intensity of reflected

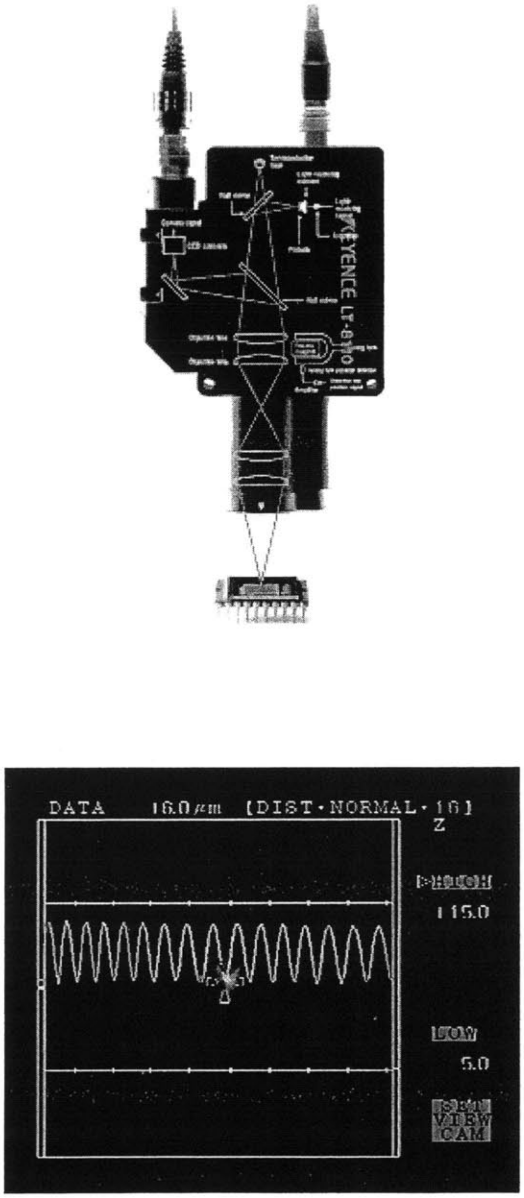

(a)

(b)

Figure 2-2: (a)The confocal surface metrology system, Keyence LT-8110. (b) Measurement of surface waves using LT-8110 (chapter 6.)

light passing through the pinhole and received by the light-receiving photodetector is maximized. When the surface is not in focus, the spot size reflected onto the detector plane, containing the pinhole, becomes larger and the transmitted intensity is less. A feedback loop is then used to maintain the maximum intensity.

2.2.2 Specifications

The confocal surface metrology system that we used in our experiments manufactured by Keyence Inc.(LT-8110) is shown in figure 2-2(a). The displacement data can either collected as a voltage output (4 mV= 1μm), or observed on the system's video monitor. In figure 2-2(b) the appearance of surface waves due to the onset Marangoni instabilities (as discussed in chapter 6) are shown on the monitor output.

Calibration tests using micromachined silicon targets show the resolution of this method is approximately 0.5 μm for measurements normal to the surface and the diameter spot at best focus is approximately 7 μm. The response time of the feedback system is 2.2 ms. The power output of the laser is 20 μW.

In our experiments, the confocal measurement system was focused on the free surface of a spreading drop at the desired point. The analog output of the measuring instrument is digitized using an A/D card controlled by the LabView program and corresponds to the evolution of the local deviation of height as a function of time. The substrate can be translated laterally either in discrete increments or at constant velocity using an automated XY stage (Compumotor, ZETA4 drive with encoder) with a positioning resolution of ±0.5 μm. A step made on a silicon wafer using wet etching process is measured by LT-8110. By scanning the surface with the XY stage (0.1 μm/s), we were able to accurately measure the height of the step (figure 2-3).

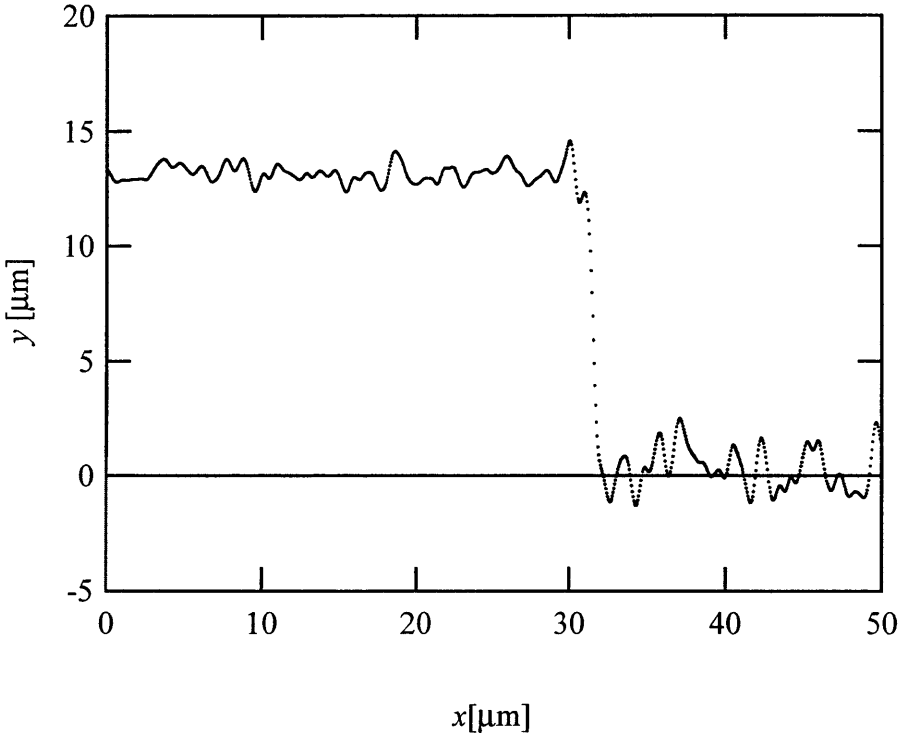

Figure 2-3: Measurement of a 13 μm step etched on a silicon wafer obtained by scanning the surface using the LT-8110.

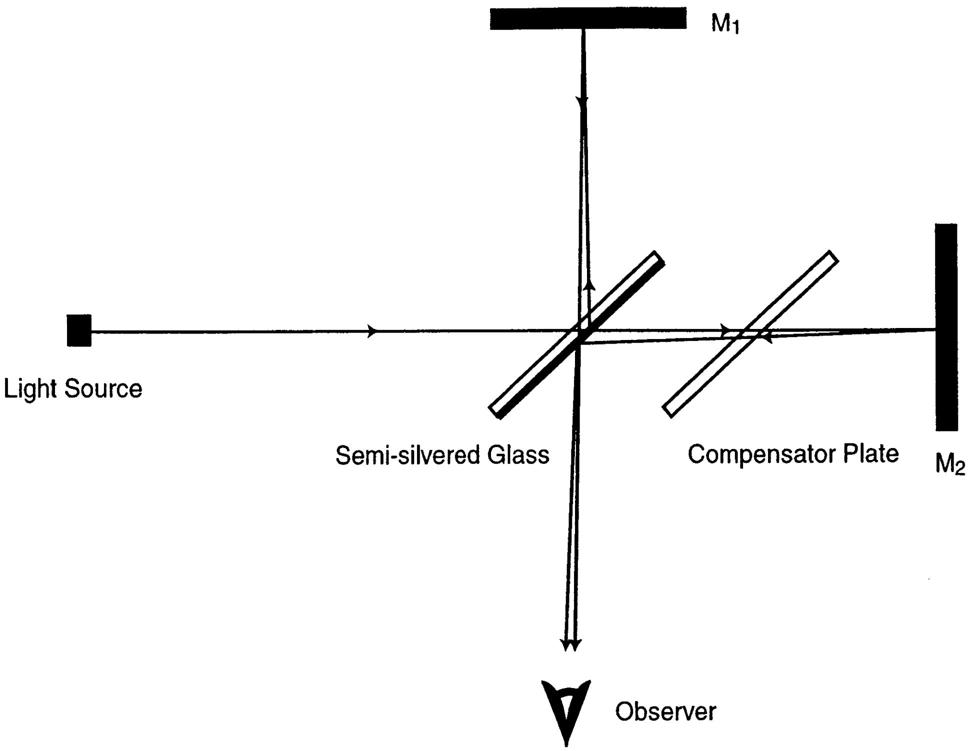

Figure 2-4: The schematic diagram of a Michelson interferometer.

2.3 Phase-shifted laser feedback interferometry

2.3.1 Interferometer

An interferometer is a device that uses optical interference of coherent light to make precise measurements of distances in terms of the wavelength of the light. Around 1880, A. A. Michelson invented the instrument, which its schematic diagram is shown in figure 2-4. Light from a monochromatic source is partly reflected and partly transmitted by a glass plate that is semi-silvered on one surface. Approximately half the incident light goes to mirror, M_1, is reflected there, and then travels through the semi-silvered glass to reach the observer. The light from the source that is transmitted by the semi-silvered glass is reflected by the mirror M_2 and then reaches the observer after being reflected by semi-silvered glass. The distances form the semi-silvered glass to M_1 and M_2 are called the arms of the interferometer. The compensator plate makes the distance traveled through the glass the same for both beams. If light travels travels slightly different distances to the mirrors, the resulting phase difference may lead to constructive or destructive interference.

Michelson's interferometer is useful because one mirror can be moved on a finely threaded screw, so that the arm length can be adjustable. This arm is usually called the reference arm of the interferometer. If M_1 moves back by $\lambda/4$, a path difference of $\lambda/2$ is added for the light traveling in this arm. Thus, at any given point on the fringe pattern, a bright fringe is replaced by a dark fringe and vice versa. By counting the number of fringes that move past the reference point, one can determine the distance traveled by one mirror to within a fraction of the wavelength of light. An interferometer may also be used to determine the refractive index of a gas [51].

2.3.2 Feedback system and its advantages

Laserbeams are are spatially and temporally coherent form of light. These properties make laserbeams the prime choice of light in interferometry. One of the most commonly used lasers is the He-Ne laser. By drilling a hole at the back of the . He-Ne laser cavity, and collecting the light from this hole by using an optical fiber one can eliminates the reference arm of the interferometer. The light will be collected by a photodetector from the optical fiber. This type of interferometer is often called Laser feedback interferometer [88]. Laser feedback interferometry (LFI) is a modified interferometer with only single-axis optical arrangement that requires minimal optical components. Because of the frequency selectivity of the laser, LFI is less sensitive to incoherently reflected light than other forms of interferometry. By elimination of additional optical elements, this system is much easier to align and more robust compared to the Michelson interferometer.

We simplify the physics of this interferometer by assuming the we can model the effect of coherent feedback in a He-Ne gas laser as a three-mirror Fabry-Perot etalon [51], where each mirror can be represented by reflectivity, $\check{R}$. As was demonstrated by Ovryn & Andrews [85] the steady-state change in the intensity of the laser that is subjected to feedback, $I(m, b, \bar{\phi})$, can be written as:

$$I(m, b, \bar{\phi}) = I_0 \left(1 + m\cos(\bar{\phi}) \sum_{j=0}^{\infty} (-b)^j \cos(j\bar{\phi})\right) \tag{2.1}$$

Equation 2.1 represents the change in intensity caused by a phase difference $\bar{\phi}$ between the incident and the reflected light with fringe visibility m, I_0 is the average intensity of the interference, b is the coupling parameter, and j is number of reflections. . Because the laser hits the sample and is reflected back into the laser cavity, the phase $\bar{\phi}$ is related to the change in the optical path length (OPL), δ as $\bar{\phi} = 4\pi\delta/\lambda$, where λ is given by the line integral of the index of refraction along the optical path. When LFI is used in a regime where the effect of multiple reflections is small ($j = 0$), equation 2.1 has the same form as a two-beam interferometer.

The interference of two electric fields E_1 and E_2 with same polarization:

$$E_1 = a_1 e^{-i\bar{\phi}_1} \tag{2.2}$$

$$E_2 = a_2 e^{-i\bar{\phi}_2} \tag{2.3}$$

generate interference intensity, I, which can be calculated, if $\bar{\phi} = \bar{\phi}_2 - \bar{\phi}_1$, as:

$$I = |E_1 + E_2|^2 = I_0 \left(1 + m\cos(\bar{\phi})\right) \tag{2.4}$$

and

$$m = 2\frac{a_1 a_2}{a_1^2 + a_2^2} \tag{2.5}$$

where m is the fringe visibility of the interference. If E_1 is the incident beam and E_2 is the reflected beam, since all of the light will not couple back into the laser cavity ($a_2 < a_1$), the visibility in LFI will not reach unity ($m < 1$).

2.3.3 Phase-shifting interferometry

To achieve higher accuracy we use an electro-optical phase modulator situated in the beam path between the front mirror of the laser cavity and the object. This modulation can be used to introduce discrete known changes in OPL that can be combined to solve for the phase and fringe visibility from a least-square fitting to an over-determined set of measurements.

To determine the phase $\bar{\phi}$ and fringe visibility m from equation 2.4, an experimentally controlled additive phase shift ψ can be introduced:

$$I_i = I_0\left(1 + m\cos(\bar{\phi} + \psi_i)\right) \tag{2.6}$$

Using an overdetermined set of measurements, it is possible to solve for the three unknowns in equation 2.6. One algorithm [50] which reduces the random error in the discrete phase step ψ, uses five discrete phase shifts: $\psi = -\pi, -\pi/2, 0, \pi/2, \pi$. Once the phase step has been introduced, the intensity is measured at the corresponding phase shift. The five resulting intensities are:

$$\begin{aligned}
I_1 &= I_0\left(1 - m\cos\bar{\phi}\right) && (2.7)\\
I_2 &= I_0\left(1 + m\sin\bar{\phi}\right) && (2.8)\\
I_3 &= I_0\left(1 + m\cos\bar{\phi}\right) && (2.9)\\
I_4 &= I_0\left(1 - m\sin\bar{\phi}\right) && (2.10)\\
I_5 &= I_0\left(1 - m\cos\bar{\phi}\right) && (2.11)
\end{aligned}$$

Then the five phase-shifted measurements can be combined and the phase and fringe visibility can be determined from:

$$\tan(\bar{\phi}) = \frac{2(I_2 - I_4)}{2I_3 - (I_1 + I_5)} \tag{2.12}$$

$$m = \frac{3\sqrt{\left(2\left(I_2 - I_4\right)\right)^2 + \left(2I_3 - I_5 - I_1\right)^2}}{2\left(I_1 + I_2 + 2I_3 + I_4 + I_5\right)} \tag{2.13}$$

The variation in the OPL, δ, can be determined from equation 2.12 by using the following relation:

$$\delta = \frac{\lambda\bar{\phi}}{4\pi} \tag{2.14}$$

2.3.4 Specifications

We have combined an electro-optically phase-shifting laser feedback interferometer (psLFI) together with a reflecting light microscope. The resulting interference micro-

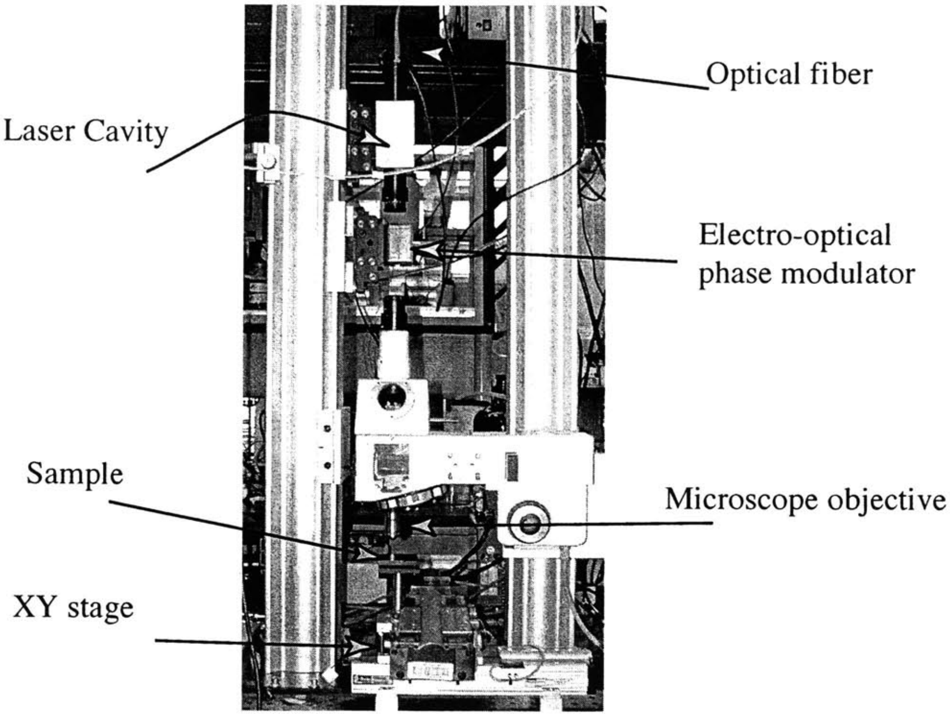

Figure 2-5: The psLFI system.

scope was used to measure the variation of the optical path length and fringe visibility (which is proportional to the sample reflectivity). Light from a low power helium-neon laser was passed through a linear polarizer and electro-optic phase modulator (New Focus, 4002) and focused with a 20×/0.4 NA objective lens (Zeiss, Epiplan). After reflection from the surface of interest, the light re-enters the laser cavity. The time-dependent change in the laser intensity was measured with a detector (New Focus, 1801) that monitored the light transmitted through the rear mirror of the laser.

The five-step phase-shifting process requires equal shifts. Therefore by determining the modulation depth for the electro-optical modulator, the process is automated with the LabView program. The used the same program to collect the output voltage from the photodetector and to calculate the phase and the fringe visibility. The program then stores the change in the optical path length and the fringe visibility as a function of time in a tab delimited text file.

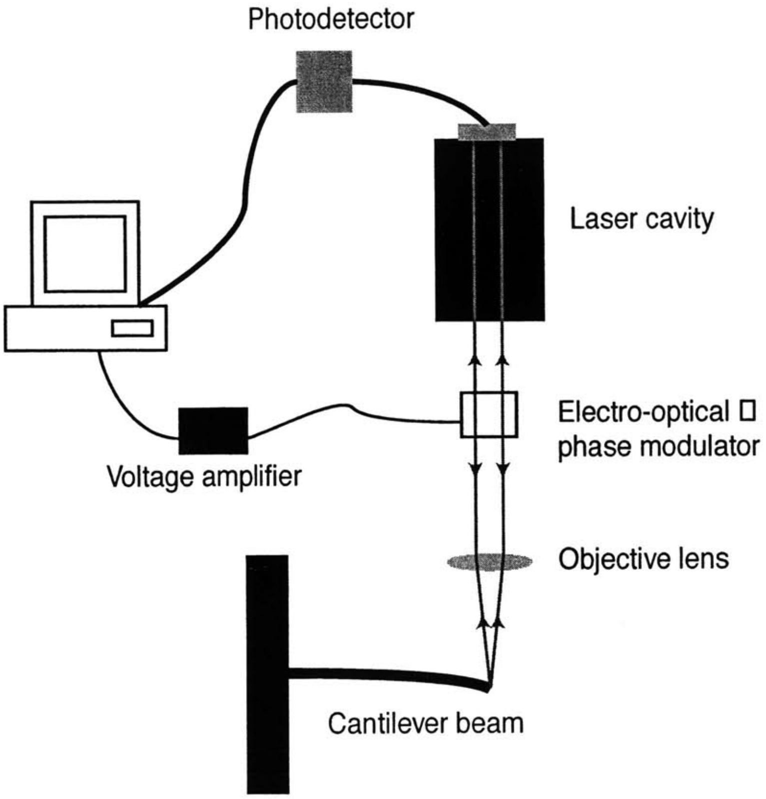

Figure 2-6: The setup for the calibration of psLFI using a cantilever bimorph.

2.3.5 Calibration

In order to calibrate the psLFI system, a measurement of of the cantilever bending of a piezoelectric bimorph was produced. The bending of the bimorph is directly proportional to the applied voltage and is a quadratic function of its length [86]. Figure 2-6 presents a schematic diagram of the apparatus used for this measurement. The bimorph was mounted on a clamp so that it formed a cantilever 10.16 mm in length with 0.38 mm thickness. Then we applied a sinusoidal voltage that produced oscillations at the tip of the cantilever of the form:

$$\delta = A \sin 2\pi f t \tag{2.15}$$

where the amplitude, A, is set to be 72 nm and the frequency, f, is 80 mHz. In figure 2-7(a), the measurement at the tip of cantilever is shown. In figure 2-7(b) the measurement of displacement of the tip is shown when the length of the cantilever increased to change the amplitude of oscillation to 850 nm for a sinusoidal wave (●) and a sawtooth wave (□)with the same amplitude and frequency.

Additional experiments have been performed to calibrate other aspects of the psLFI system [85, 87, 44]. For example, a spatial calibration of the psLFI microscope was done [87] also using a piezoelectric bimorph (figure 2-8). The data is acquired using psLFI by utilizing a XY stage to scan along the bimorph cantilever. It can be observed that the instrument accurately captures the theoretically-predicted parabolic deflections of the cantilever.

The important issue of using psLFI on transparent materials with curved surface was investigated in detail by Fischer & Ovryn [44]. When psLFI is focused on a dry reflective surface, most of the incident rays will reflect back and are collected by the objective lens. However, the curved surface and difference in index of refraction between air and the liquid influence the path of the rays. Fischer & Ovryn [44] showed that there is always a single reflected ray, which they called the *magic ray*, that follows the same path as the incident ray (figure 2-9).

A phase correction needed to justify this effect on the psLFI measurements is given in equation 2.16.

$$\bar{\phi} = \frac{4\pi}{\lambda}\left(nh(x_c) - b\right) \tag{2.16}$$

$$b = \sqrt{h(x_c)^2 + (x_f - x_c)^2} \tag{2.17}$$

x_f is the scan position and x_c is the virtual location. The geometrical parameters in these equations are shown in figure 2-10.

Calibration tests indicate that the lateral spatial resolution (diffraction limited) of this system is 0.96 μm when an objective lens with 0.4 NA is used and that the optical path length may be measured with an rms error of 10 nm, with a response time of approximately 2 ms. Numerical aperture is defined as the ratio of the radius of the objective lens to the lens focal length NA $= R/f$. Since we are also interested in measuring curved surfaces (surface of spreading drops, chapter 3-6,7), the issue of numerical aperture is very important. By increasing the numerical aperture, the lateral resolution, *Res*, of the measurement improves, $Res \sim \lambda/2\mathrm{NA}$. However, by

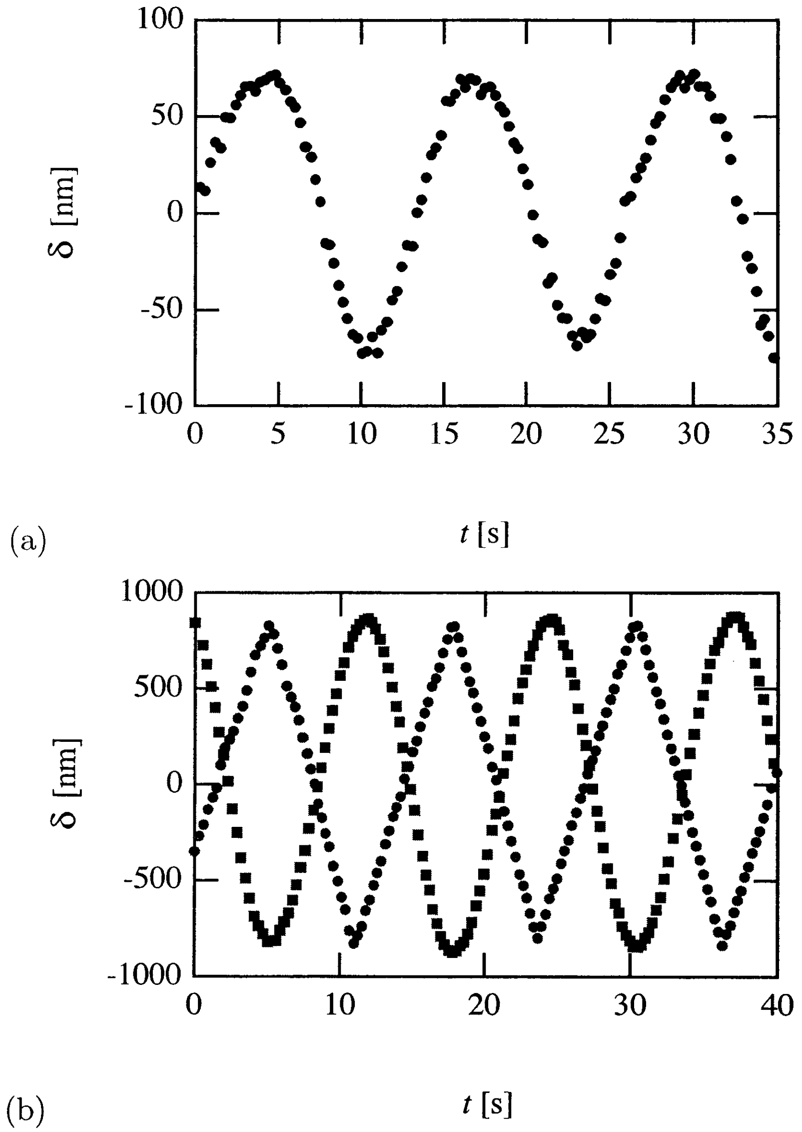

Figure 2-7: The results for psLFI measurement of the tip of cantilever bimorph when it oscillates as (a) a sinusoidal oscillation with amplitude of 72 nm with frequency of $f = 80\text{mHz}$, and (b) a sinusoidal oscillation (□) and a sawtooth oscillation (•). Both waves have amplitude of 850 nm and frequency of $f = 80\text{mHz}$.

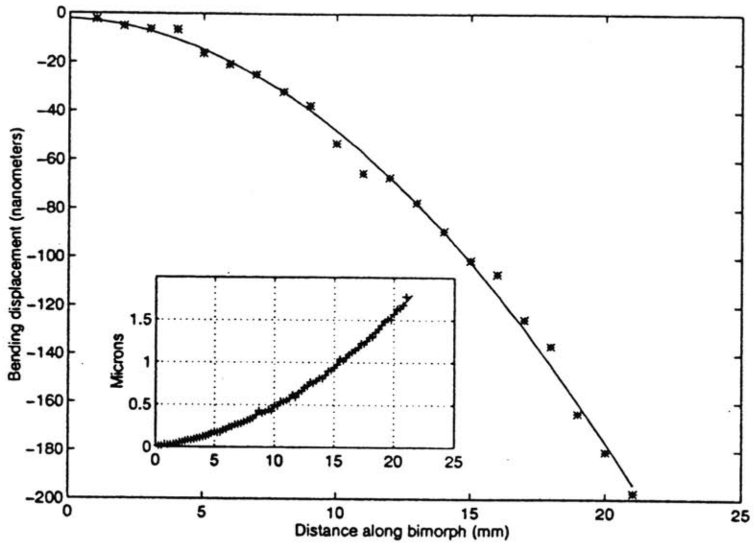

Figure 2-8: Bending curve for the piezoelectric bimorph after two separate voltages applied, 4.0 V and -500 mV. Profile is measured by psLFI (from [87])

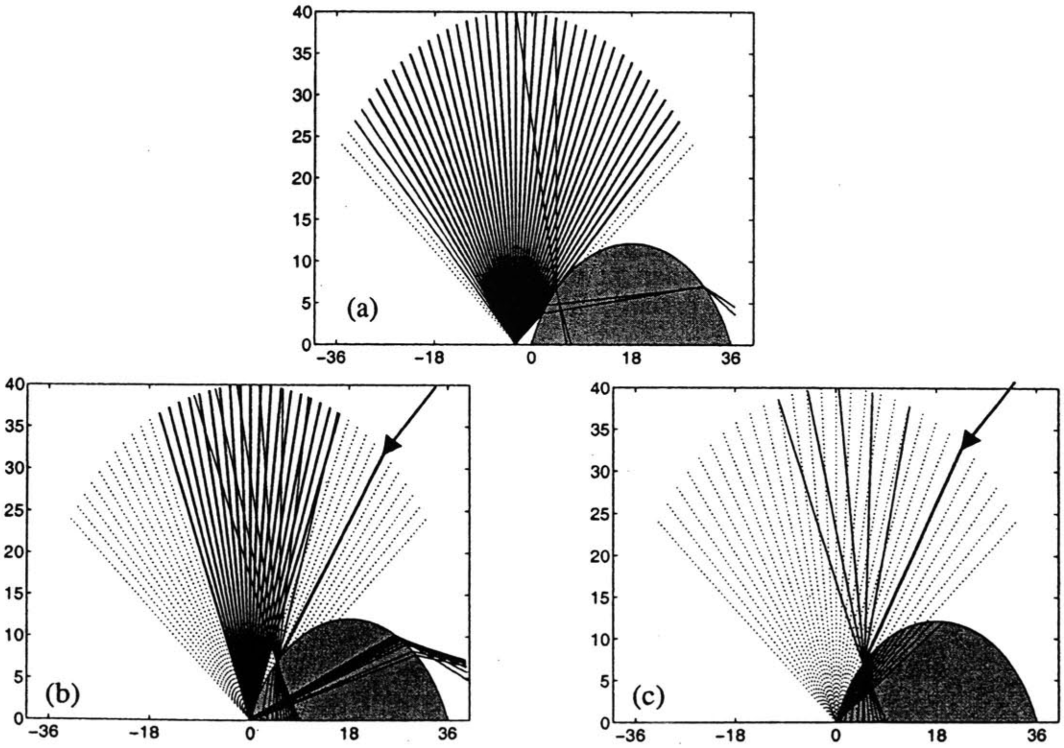

Figure 2-9: A high NA beam is scanned from outside (a and b) to inside of a drop (c). The ray shown by the arrow represent the magic ray (from [44]).

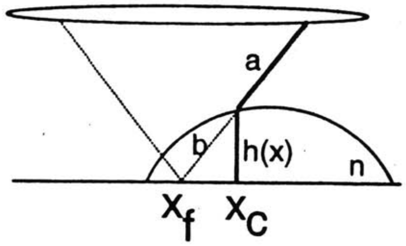

Figure 2-10: Important geometrical parameters for magic ray correction. The scan position is at x_f (from [44]).

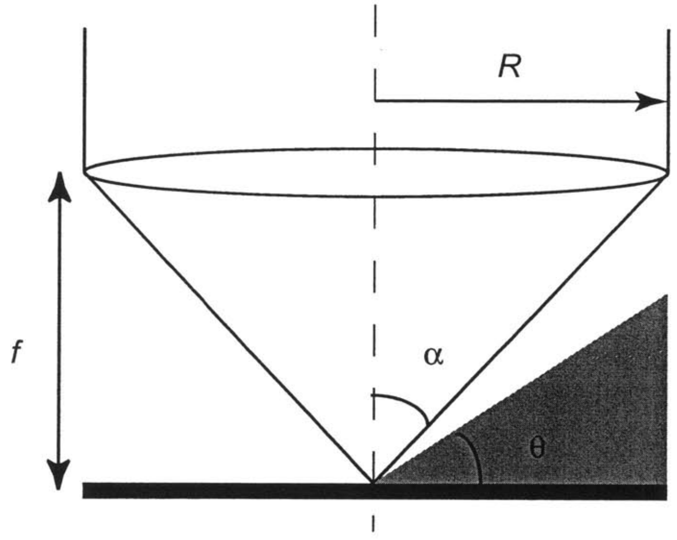

Figure 2-11: Limitation of the measurement of the surface slope for a lens with $\mathrm{NA} = R/f$ in psLFI.

increasing the numerical aperture, the ability of measuring at the liquid free surfaces with slope θ larger than $\alpha = \arcsin(\mathrm{NA}/n)$ (figure 2-11). By increasing the numerical aperture, *alpha* increases, but to have a correct measurement of slope, $\alpha + \theta \leq \pi$. Therefore, for NA can not be larger than certain number. This is a trade off between the lateral resolution and the slope of the profile. In the following chapters, we will always be careful in our selection for objective lens. We make sure that the numerical aperture is big enough to lead to a better lateral resolution that lateral length scales but at the same time able to measure the slope of drop accurately.

In table 2.2, we compare the two optical measurement systems that have been

Table 2.2: Comparison between psLFI and the confocal surface metrology systems.

Features	**psLFI**	**Confocal surface metrology LT-8110**
Response time	~ 1 ms	2.2 ms
Lateral resolution	0.8 μm	7 μm
Vertical resolution	10 nm	500 nm
Range of measurement	up to 500 μm	± 1 mm
Working distance	6.25 mm	25mm
Light source	He-Ne laser	Semiconductor laser
Wave length, λ	633 nm	670 nm
Power output	0.5 mW	0.02 mW
Data output	OPL and fringe visibility	Displacement

discussed in this chapter. As indicated, the psLFI system has much better lateral and vertical resolutions compared to the LT-8110 system. If very high resolution is not desired, LT-8110 provides the users with a greater flexibility because of large range of measurement and working distance. Furthermore, LT-8110 is very compact unit compared to the psLFI microscope.

Having developed and calibrated the above mentioned systems, we now proceed to use them to investigate steady and dynamic spreading of liquid film on dry surfaces in the following chapters.

Chapter 3

Steady spreading of viscous fluid drops

3.1 Introduction

The spreading of liquid drops on solid surfaces has been subject of numerous research papers through out the last century. Several aspects of this problem have been of interest of engineers and physicists. Some common examples include the spreading of liquid droplets on solids such as in the spraying of paint and agricultural chemicals, the penetration of ink in paper, the liquid absorbency or propellency of fabrics, and the displacement of one fluid by another over a solid in enhanced oil recovery. Generally, one can separate this field to two general categories:

- Macroscopic features of spreading. Variation of radius and thickness of the spreading liquid drops as a function of time is very important. In paint industry, the final thickness and area of painted as well as the time of process are very critical. Liquid viscosity, μ, surface tension, σ, volume of the drop, Ω, are all important parameters that can affect the spreading process. As it will be discussed, the spreading regimes of the liquid drop is greatly depends on these properties.
- Microscopic features of spreading such as characteristics of the precursor layer

and its effect on the spreading. The surface energy, Hamaker constant, polarity of the fluid, molecule size and formation, and surface charges are some examples of the parameters that affect the microscopic region of the drop. The physics of microscopic features are very important for the understanding of fundamental of spreading process.

Historically, most of the early work has focused on the macroscopic features of spreading dynamics. This was due to the lack of experimental instruments that were able to detect and quantify the microscopic dynamics of spreading. As noted in chapter 2, it was not until the 1960s that suitable optical methods become available for these types of experiment. However, this did not stop scientists from looking for answers to questions of spreading in the microscopic regions. A good example is work of Hardy [49] who used the humid air environment and investigated the microscopic "invisible" film of acetic acid. He observed interactions between macroscopic drops of acetic acid placed with a distance from each other on glass. The humidity of surrounding air effected the shape of these drops. He concluded the interactions are due to an invisible film of acetic acid spreading from the macroscopic drops.

In this chapter, the theories of several different regimes of spreading are presented. It will be shown that depending on values of certain dimensionless parameters, the liquid drop will exhibit different spreading behavior which often take the form of a power-law relation for the radius of the drop as a function of time, $R(t) = At^n$. The relation for the dynamic contact angle, θ_a, as a function of time and other physical parameters will also be derived, and the well-known Hoffman-Voinov-Tanner law will be presented. Following the analysis, the experimental results are presented to confirm or refute the theoretical predictions.

3.2 Theoretical approach

When a viscous drop of wetting liquid is placed on a solid surface (figure 3-1), the evolution of the droplet shape depends on its physical properties and its initial volume. The Ohnesorge number, $Oh = \mu/\sqrt{\rho R \sigma}$, scales the forces that resist the spreading.

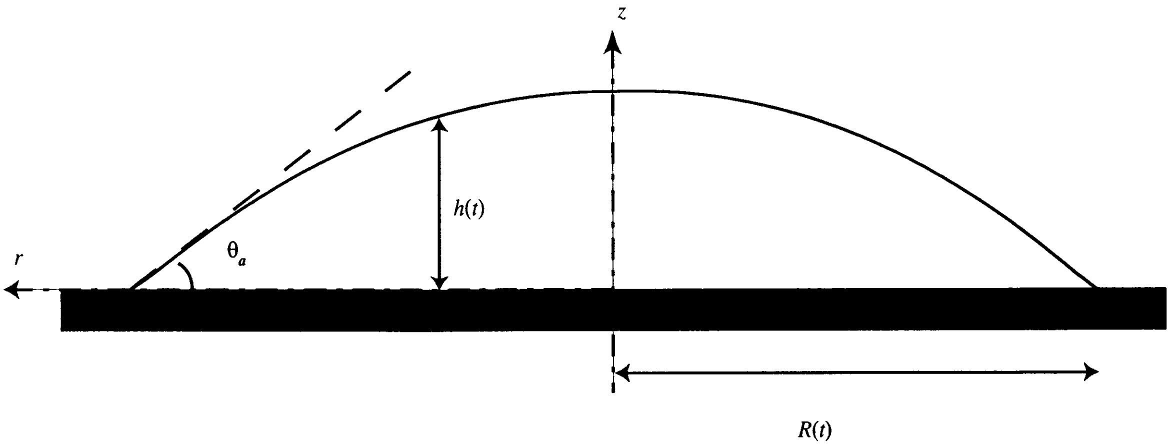

Figure 3-1: The schematic geometry of the spreading drop.

For $Oh \gg 1$ the spreading is resisted primarily by viscous stresses in the fluid, whereas at low $Oh \ll 1$ the spreading is retarded principally by fluid inertial effects. The dominant driving force of the spreading depends on the relative size of the drop compared to the capillary length $\ell_{cap} = \sqrt{\sigma/\rho g}$. In figure 3-2 we show three regimes for evolution for spreading viscous droplets corresponding to $Oh \gg 1$. If the characteristic length scale for a drop of volume Ω is taken as $(\Omega/\pi)^{1/3}$ then an appropriate measure of the dimensionless drop size is $\phi = (\Omega/\pi)^{1/3}/\ell_{cap}$. For small viscous drops ($\phi < 1$; $Oh \gg 1$), the spreading is driven by capillary force imbalance at the contact line, and resisted by viscosity. However for larger viscous drops ($\phi > 1$; $Oh \gg 1$), spreading is initially driven by the gravitational body force instead of capillary forces. For the conditions considered in the present study, the impact velocity during the drop deposition process has negligible effects. The three regimes shown in figure 3-2 for a viscous drop ($Oh \gg 1$) depend on the relative magnitudes of the height, $h(t)$, and the radius, $R(t)$, compared to the capillary length, $\ell_{cap} = \sqrt{\sigma/\rho g}$. Small drops with $h < R < \ell_{cap}$ assume the shape of a spherical cap. In this regime, capillarity acts as the driving force and viscous flow throughout the spherical cap provides the resistance. Scaling arguments yield a power-law for variation of the drop radius as a function of time of the form $R(t) \sim t^{1/10}$ [110] (for further details see section 3.3.2). For larger initial volumes ($\phi > 1$) with $\ell_{cap} < h < R$ the drop initially spreads as a

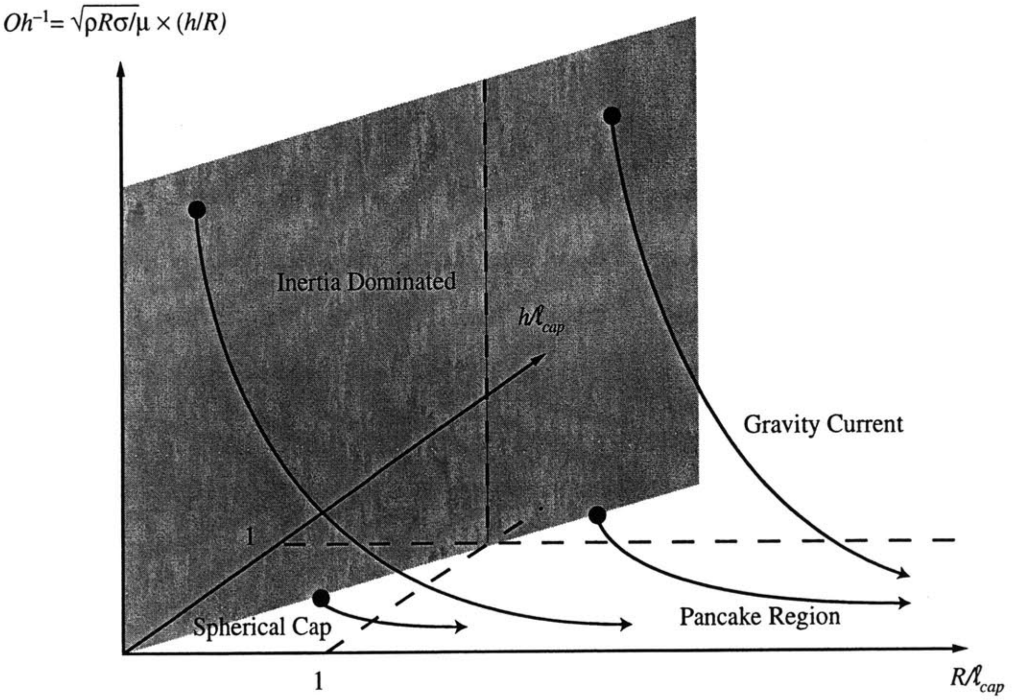

Figure 3-2: Three characteristic regimes of spreading drops of a drop The dynamics in each regime depends on the relative magnitudes of the height, $h(t)$, the radius, $R(t)$, the capillary length, ℓ_{cap}, and the Ohnesorge number, Oh.

gravity current. Evolution of the drop radius as a function of time can be found by balancing the gravitational body force with viscous stresses and yields $R(t) \sim t^{1/8}$ (see [65]; also section 3.3.1). After a long time, the thickness of the spreading drop becomes very small and both of the regimes described above evolve towards a pancake regime with $h < \ell_{cap} < R$. In this regime, capillarity and viscous stresses are important in an annular region close to contact line (of lateral extent ℓ_{cap} from the contact line). Gravitational forces once again become important in the rest of the drop but only serve to act as a hydrostatic force, leading to a pancake-like central region of constant thickness. In this regime the power-law spreading is of the form $R(t) \sim t^{1/7}$ [39].

An important note must we had regarding the conventional definition of the Ohnesorge number as used in this work. The common definition for the Ohnesorge number is $Oh = \mu/\sqrt{\rho R \sigma}$ where μ, σ, ρ and R are the viscosity, surface tension, density and the length scale of the system, respectively. The Ohnesorge number is the ratio of the viscous force to the inertial force in the presence of the capillary force. If one substitutes the velocity in the Reynolds number, $Re = \rho UR/\mu$, with capillary velocity scale, σ/μ, it is found that $Oh^2 = 1/Re$. However the Reynolds number that naturally arises in lubrication analyses (with $h/R \ll 1$) is defined as $Re = (\rho UR/\mu)(h/R)^2$ where h is the maximum drop thickness and R is the drop radius. This leads to a modified definition for the Ohnesorge number as:

$$Oh = Re^{-1/2} = \frac{\mu}{\sqrt{\rho\sigma R}}\frac{R}{h} \tag{3.1}$$

Since both radius and thickness of drop are function of time, it is not clear a priori if the Ohnesorge number decreases or increases during the spreading process. It is however known that the drop volume, Ω, is conserved during the spreading therefore the radius of the spreading is related to the drop thickness via $h \sim \Omega/R^2$. By substituting this relation into the equation 3.1, one can find the relation between the Ohnesorge number and the radius as:

$$Oh(t) \sim \frac{\mu}{\sqrt{\rho\sigma}} \frac{R(t)^{5/2}}{\Omega} \tag{3.2}$$

As the drop spreads (larger radius), the Ohnesorge number increases and the effect of viscous forces progressively dominate over inertial effects. The modified definition of the Ohnesorge number (equation 3.1) can rationalize the behavior of all of spreading regimes that will end up the the viscous dominated regimes after initial stages of the spreading (figure 3-2).

There is also another approach to these types of problems that is called scaling analysis. The idea is to balance the dominant forces acting in the system, one can find relations between characteristic parameters of the system. This method provides a powerful tool for systems which involve two dominant competing forces. For well-defined region of Oh and ϕ, the drop spreading problem is a case in which there are usually two active forces acting on the drop. These forces are usually called the driving force that provides the energy for the system and the resisting force which serves to dissipate the energy. For example for $Oh \gg 1$ and $\phi < 1$, the driving force for spreading is the capillarity and the viscous force resists spreading. The mathematics used in this scaling approach is less complicated than required for directly solving the governing equations, which are usually non-linear PDEs. However, the final relation usually lacks a numerical front factor of order unity. This method has been used in a wide range of subjects [5]and was first used in the spreading problems by Fay [41] and [61]. A few interesting works have been done (e.g. [33]) to explore the use of this powerful tool in this area of research.

In the next section, both of this methods are used to derive the relations for radius, $R(t)$, thickness, $h(t)$, and dynamics contact angle, θ_a, as a function of time.

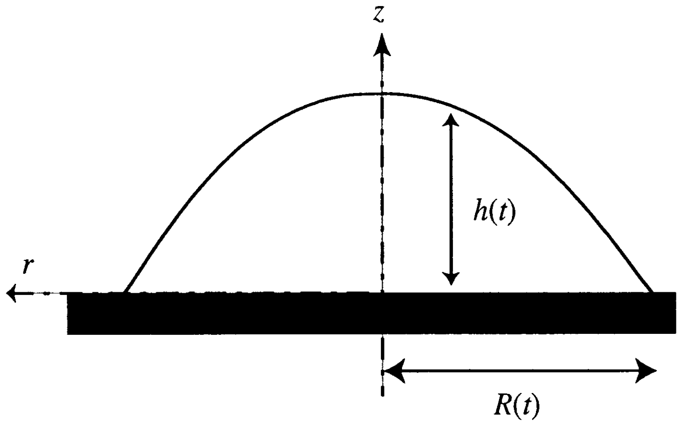

Figure 3-3: The schematic geometry of the spreading drop in gravity current region.

3.3 Regimes of macroscopic spreading

3.3.1 Gravity Current

As mentioned in the previous section, if $\phi > 1$, then one can neglect interfacial effects. Therefore the driving force of spreading is the gravitational body force and the resisting force arises from viscosity. A schematic figure of this problem is shown in figure 3-3. By assuming that the flow is axisymmetric and using standard lubrication analysis, the continuity and Navier-Stokes equations have the form of:

$$\frac{\partial v}{\partial z} + \frac{1}{r}\frac{\partial}{\partial r}(ru) = 0 \tag{3.3}$$

$$\frac{\partial p}{\partial r} = \mu \frac{\partial^2 u}{\partial z^2} \tag{3.4}$$

By neglecting the effect of surface tension, we can write the pressure relation when only gravity effects it:

$$p = p_0 + \rho g(h - z) \tag{3.5}$$

therefore:

$$\rho g \frac{\partial h}{\partial r} = \mu \frac{\partial^2 u}{\partial z^2} \tag{3.6}$$

By integrating the continuity equation from $z = 0$ to $z = h(r, t)$:

$$v(h) - v(0) + \frac{1}{r}\frac{\partial}{\partial r}\int_0^h u dz = 0 \tag{3.7}$$

Since $v(0) = 0$ and $v(h) = \partial h/\partial t$ then:

$$\frac{\partial h}{\partial r} + \frac{1}{r}\frac{\partial}{\partial r}\int_0^h u dz = 0. \tag{3.8}$$

Also we assume the drop volume, Ω is fixed as:

$$\Omega = 2\pi \int_0^{R(t)} r h dr. \tag{3.9}$$

By integrating 3.6 twice with respect to z and imposing the boundary conditions:

$$z = 0 \rightarrow u = 0, \tag{3.10}$$

$$z = h \rightarrow -\mu\frac{\partial u}{\partial z} = 0, \tag{3.11}$$

the axial velocity, u, can be found to be:

$$u = -\frac{\rho g}{2\mu}\frac{\partial h}{\partial r} z(2h - z). \tag{3.12}$$

By substituting in equation 3.8, we obtain the following differential equation:

$$\frac{\partial h}{\partial t} - \frac{\rho g}{3\mu}\frac{1}{r}\frac{\partial}{\partial r}(r h^3 \frac{\partial h}{\partial r}) = 0. \tag{3.13}$$

This nonlinear PDE can be solved analytically by similarity transformation. First we define:

$$\xi = \left(\frac{\rho g \Omega^3}{3\mu}\right)^{-1/8} r t^{-1/8}. \tag{3.14}$$

Also, a new dependent variable, ζ, is defined such that the drop thickness is expressed as:

$$h(r,t) = \xi_R^{2/3}\left(\frac{3\Omega\mu}{\rho g}\right)^{1/4} t^{-1/4}\zeta, \tag{3.15}$$

Here ξ_R is the value of ξ at $r = R$. By combining equations 3.14 and 3.15 in equation 3.13, the following differential equation relates the similarity variables:

$$\frac{d}{d\varsigma}\left(\varsigma\zeta^3\frac{d\zeta}{d\varsigma}\right)+\frac{1}{8}\varsigma^2\frac{d\zeta}{d\varsigma}+\frac{1}{4}\varsigma\zeta=0, \tag{3.16}$$

where $\varsigma = \xi/\xi_R$. From equation 3.9, ξ_R is calculated to be:

$$\xi_R = \left(2\pi\int_0^1 \varsigma\zeta d\varsigma\right)^{-3/8}. \tag{3.17}$$

The solution to equation 3.16 is [91]:

$$\zeta = \left(\frac{3}{16}\right)^{1/3}\left(1-\varsigma^2\right)^{1/3}, \tag{3.18}$$

$$\xi_R = \left(\frac{2^{10}}{3^4\pi^3}\right)^{1/8} = 0.894. \tag{3.19}$$

or

$$h(r,t) = 0.531\left(\frac{3\mu\Omega}{\rho g t}\right)^{1/4}\left(1-(r/R)^2\right)^{1/3}, \tag{3.20}$$

$$R(t) = 0.894\left(\frac{\rho g\Omega^3}{3\mu}\right)^{1/8} t^{1/8} \tag{3.21}$$

It can be seen that the radius of drop has a power-law relation of the form $R(t) \sim t^{1/8}$ with time.

3.3.2 The Hoffman-Voinov-Tanner law

When $\phi < 1$, the gravitational effects is negligible in the spreading drops. If $Oh \gg 1$, then the driving force of the spreading is the capillarity force and the resisting force is the viscous force. Let's assume the geometry which is shown in figure 3-4. A quasi-steady hydrodynamic analysis of the drop spreading on a horizontal substrate leads to an explicit model for the dynamic contact angle and power-law that relates the radius of the drop as a function of time. Let's begin with the lubrication equation:

$$\frac{\partial p}{\partial r} = \mu\frac{\partial^2 u}{\partial z^2} \tag{3.22}$$

This equation is integrated twice with respect to z and with no slip boundary conditions at the wall and no shear at the free surface, the mean velocity in r direction is:

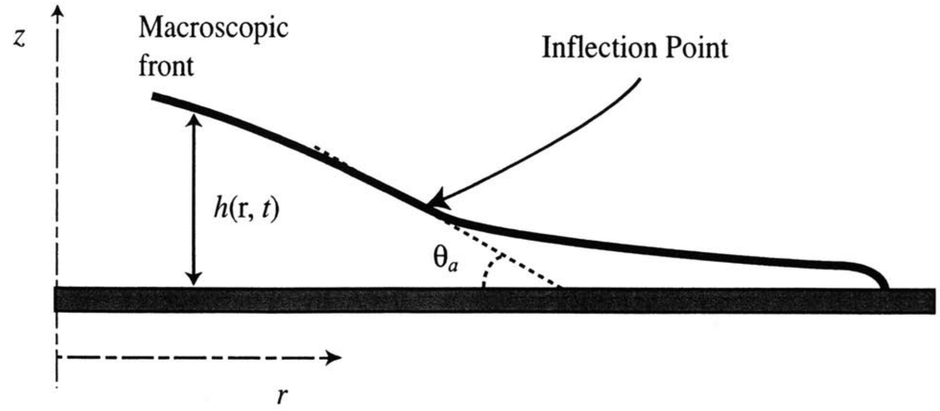

Figure 3-4: Drop shape near the inflection point close to the moving contact line.

$$\bar{u} = -\frac{h^2}{3\mu}\frac{dp}{dr} \tag{3.23}$$

For pressure gradient, we can use the Laplace-Young relation ($p = -\sigma d^2h/dr^2$ assuming slope of the free surface of drop is very small) which gives the following:

$$\frac{dp}{dr} = -\sigma\frac{d^3h}{dr^3} \tag{3.24}$$

replacing 3.24 in equation 3.23, the governing equation for the free surface of the spreading drop is found to be:

$$3Ca = h^2\frac{d^3h}{dr^3} \tag{3.25}$$

where the capillary number, Ca, is defined based on the average velocity, $\bar{u}$.

Let's define the following dimensionless parameters:

$$r^* = -\frac{r}{r_0} \tag{3.26}$$

$$h^* = \frac{h}{h_0} \tag{3.27}$$

$$h_0 = r_0(3Ca)^{1/3} \tag{3.28}$$

The dimensionless form of equation 3.25 is then:

$$h^{*2}\frac{d^3h^*}{dr^{*3}} = -1 \tag{3.29}$$

This equation has the property that there is a range of values of the parameter h_0 such that the curve h^* has an inflection point as shown in figure 3-4. To identify the apparent contact angle, θ_a, which is the slope of the drop at the inflection point [79], one can write:

$$\theta_a \equiv -\left(\frac{dh}{dr}\right)_i = \frac{h_0}{r_0}\left(\frac{dh^*}{dr^*}\right)_i = (3Ca)^{1/3}\left(\frac{dh^*}{dr^*}\right)_i \qquad (3.30)$$

The term $(dh^*/dr^*)_i$ is usually assumed to be a constant however in the following section, it will be shown that this term is actually a logarithmic function of the capillary number [30]. Most of the previous experiments were done by assuming this term is constant and the relation between the dynamic contact angle and capillary are presented as:

$$\theta_a = k_1 Ca^{1/3} \qquad (3.31)$$

The equation 3.31 is usually called "Tanner's law" or "Hoffman-Voinov-Tanner law" [69]. The constant k_1 is not a universal constant [15] and it varies for each experiment but its value is usually close to 3 when θ_a is in radian. A summary of a few of the experimental and analytical works regarding this power law is presented in table 3.1.

Going back to the spreading power-law, since gravitational force is negligible, the shape of the spreading drop is that of a spherical cap of a radius R and height of h. For $R \gg h$:

$$\Omega = \frac{\pi h R^2}{2} = \frac{\pi R^3 \theta_a}{4}. \qquad (3.32)$$

Using this relation in the equation 3.31:

$$\Omega = \frac{\pi k_1 R^3}{4}\left(\frac{\mu}{\sigma}\frac{dR}{dt}\right)^{1/3}. \qquad (3.33)$$

This equation can be integrated to give:

$$R(t) = \left(\frac{4\Omega}{\pi k_1}\right)^{3/10}\left(\frac{10\sigma t}{\mu}\right)^{1/10} + R_0 \qquad (3.34)$$

For a very large radius and $k_1 = 3$:

$$R(t) = 0.97 \left(\frac{\sigma \Omega^3 t}{\mu} \right)^{1/10} \tag{3.35}$$

Or simply $R(t) \sim t^{1/10}$.

3.3.3 Scaling analysis

In this section, a scaling analysis is applied to the above mentioned regimes of spreading. An important constraint of this system is the volume of the drop is always conserved which means there is no evaporation or chemical reaction present during the spreading. The volume of drop, Ω, can be calculated as $\Omega = \pi R^2 h/2$ where $R(t)$ is the drop radius and $h(t)$ is the drop thickness at its center. For all of the following cases, it is assumed that the fluid fully wets the surface (spreading parameter $S > 0$ as it defined by equation 1.2).As it was mentioned before $\ell_{cap} = \sqrt{\sigma/\rho g}$ is the capillary length.

Capillary-Viscosity :

For very small drops, the characteristic length of the drop, $(\Omega/\pi)^{1/3}$, is smaller than capillary length ($\phi < 1$). The drop always assumes the shape of a spherical cap. Since the effect of gravity is negligible, the driving force of spreading is the capillary force and viscous forces is resisting the spreading.

From the equation of motion, one can balance these forces (forces per unit volume) as:

$$\mu \frac{\dot{R}}{h^2} \sim \frac{1}{R} \frac{\sigma h}{R^2} \tag{3.36}$$

The left hand side of this relation is the viscous dissipation term from Navier-Stokes equation and the right hand side is the dp/dr term as shown previously in equation 3.24. From the Laplace-Young relation the pressure term can be written as the capillarity term. The curvature of the surface is $-h/R^2$ due to the fact that the drop has a shape of a spherical cap. By substituting dR/dt for $\dot{R}$ and $\Omega/(2\pi R^2)$ for h, we find the following relation:

$$\mu \frac{dR}{dt} \frac{1}{\left(\Omega/(2\pi R^2)\right)^2} \sim \frac{\sigma h}{R^3} \frac{\Omega}{2\pi R^2} \tag{3.37}$$

By rearranging and integration, the relation for $R(t)$ as a function of time is found to be:

$$R(t) \simeq \left(\frac{80\Omega^3}{\pi^3}\right)^{1/10} \left(\frac{\sigma}{\mu}\right)^{1/10} t^{1/10} = 1.1 \left(\frac{\sigma\Omega^3 t}{\mu}\right)^{1/10} \tag{3.38}$$

Thus by using this simple scaling analysis we were able to generate a similar relation to equation 3.35. The ratio of the scaling result to the direct solution is $R_{Scaling}/R_{Direct} = 1.13$.

Gravity current :

If the drop size is large compared to the capillary length, $\phi > 1$, then the effect of capillary forces are negligible ($Bo = \rho g h^2/\sigma \gg 1$). Then the driving force of spreading is the gravitational force and the resisting force is the viscous force. Following the governing equation, one can balance the forces as:

$$\mu \frac{\dot{R}}{h^2} \sim \frac{1}{R} \rho g h \tag{3.39}$$

Once again by substituting for $\dot{R} = dR/dt$ and $h = \Omega/(2\pi R^2)$ and integrating, the following relation for the radius of the large drops as a function of time is found:

$$R(t) \simeq 1.095 \left(\frac{\rho g \Omega^3}{\mu}\right)^{1/8} t^{1/8} \tag{3.40}$$

which is reproduction of the equation 3.21. Once again the ratio of scaling to direct solution is $R_{Scaling}/R_{Direct} = 1.41$.

We can assume that the dynamic contact angle can scale as $\theta_a \sim h/R$. Using the conservation of mass and equation 3.40, the power-law relation for the dynamic contact angle is found to be $\theta_a \sim Ca^{3/7}$.

Pancake region :

When a spreading drop in either of previously mentioned regions spreads for a long time, the thickness of it becomes very small and it evolves to a 'pancake regime' with $h < \ell_{cap} < R$. In this regime, capillarity and viscous stresses are important in an annular region close to the contact line (of a lateral extent $\Delta r \sim \ell_{cap}$ from the contact line). Gravitational forces become important in the rest of the drop but only serve to act as a hydrostatic force, leading to a 'pancake-like' central region of constant thickness. However, near the edge region the surface tension effect provides energy for spreading and viscous forces dissipate this energy. Unlike the spherical cap region, the curvature at the edge region is now h/ℓ_{cap}^2 and the gradient of the pressure is only taken over the edge region:

$$\mu \frac{\dot{R}}{h^2} \sim \frac{1}{\ell_{cap}} \left(\sigma \frac{h}{\ell_{cap}^2} \right) \tag{3.41}$$

Following the previous procedures, the relation between $R(t)$ and time is found to be:

$$R(t) \simeq 1.09 \left(\frac{\sigma \Omega^3}{\mu \ell_{cap}^3} \right)^{1/7} t^{1/7} \tag{3.42}$$

which is similar to the power law presented by [39] which is derived by directly solving the governing equations.

The power-law for the dynamic contact angle is found to be $\theta_a \sim h/\ell_{cap} \sim Ca^{1/3}$ which is similar to HVT law (section 3.3.2).

Inertia-Capillary :

At very early stage of spreading for drops with low viscosity($Oh \ll 1$), there exists a regime in which the driving force of spreading is capillarity but since viscous effects are negligible (small Ohnesorge number), the inertial force is the only resisting force. Since the shape of the spreading drop is approximately hemispherical, the curvature of the free surface is $-2/R$. By balancing the capillary force and inertia forces:

$$\frac{\rho \dot{R}^2}{R} \sim \frac{1}{R}\frac{2\sigma}{R} \tag{3.43}$$

By integration, one can get the following relation:

$$R(t) \simeq 1.65 \left(\frac{\rho}{\sigma}\right)^{1/3} t^{2/3} \tag{3.44}$$

The scaling method is a very powerful tool that not only enable us to find the solution faster and easier, but helps elucidate the understanding of the physics of the problem. Many nonlinear and complicated problems in physics can be solved or are solved by scaling analysis. A book by [5] in this subject is highly recommended.

3.3.4 Microscopic model and the matching region

In this section, an important issue regarding the "Hoffman-Voinov-Tanner" law is addressed. In the last 50 years, there have been numerous experiments regarding the spreading regimes of a viscous drop on surfaces. Before the 1970s (before the HVT law was established), power law form of spreading for the dynamic contact angle, θ_a, and the velocity of spreading was known. Analytical work for spreading of a liquid drop on a previously wetted surface [47] and experiments on spreading of polymer melts on solid surface [101] were shown such a relationship. However Hoffman, Voinov, and Tanner were the first to realize the more general relation between θ_a and the dimensionless capillary number. Since this time, most of the spreading results are presented in form of $\theta_a \sim Ca^{1/3}$ or $\theta_a \sim Ca^n$ where the value of n is experimentally determined and is close to 1/3. These experiments are carried out by using well characterized Newtonian fluids on different substrates or inside a capillary tubes. A detailed discussion is given by Kistler [69]. We have summarized most of the published works (experimental and analytical) in table 3.1. In the derivation of the HVT law, the fluid and the surface properties do not effect the governing equation (surface tension and viscosity effects are considered only in setting the magnitude of the capillary number). However, as it seen in table 3.1 the front factor and the power-law exponent of the relation are not consistent. The first thing that comes to mind is that the geometry of the experiments are different. A few sets are obtained from inside of a capillary tube, or parallel plates. In many cases, the drop was allowed to spread under the gravitational or capillary driving forces, and there are also some cases in which the fluid was forced to wet the surface by plunging a plate or a rod into the fluid.

There is also an important issue regarding the measurement of contact angle. As mentioned before in chapter 2, during the last forty years the methods that have been used did not all possess same lateral and vertical resolutions. To measure the contact angle, it was customary to measure the slope of the free surface near the contact line. This type of measurements was very inconsistent since the measurements are resolution dependent. Due to the existence of the inflection point (point of maximum slope at which the dynamic contact angle has to be measured) close to the moving contact line (figure 3-4), the closer they got to the contact line, the measured angle was closed to the real contact angle. The dependency of the contact angle measurement on the system resolution could have caused the inconsistency in the reported data in the earlier works. However this could not be the only reason since in the late 1970s and early 1980s, most of these measurements were done by high resolution systems.

Due to these issues, the contact angle measurement and the shape of the free surface have been of special interest of physicists. Garoff and co-workers [36, 77, 22] have extensively investigated the free surface of the spreading film on a solid surface at the vicinity of the moving contact line. Their experiments consisted of immersing a glass tube tilted at an angle to the horizontal at a constant speed into a bath of silicone oil. the slope of air-fluid interface was measured at distances from the contact line. They were able to confirm the analytical prediction of such profiles given by Ngan & Dussan V. [81]. Also found in their experiments was the HVT law is valid for capillary numbers up to 0.1 and for $Ca > 0.1$ the model fails to describe the experimental data. They concluded that the breakdown is due to the low-order of the geometry -free part of the perturbation solution of their analysis.

Works done by Chen & Wada [19, 20, 21] were concentrated on the shape of the free surface of the drop and the dynamic contact angle. By observing interference fringes relating them to the film thickness, they were able to measure the thickness of a spreading drop of silicone oil on glass. To measure the dynamic contact angle, numerical differentiation of the measured thickness was used. The experimental results had a good agreement with the HVT law, however the issue of the location of dynamic contact angle were not resolved. By relying on the visible interference fringes, there were not able to detect an inflection point at the free surface of drop because interference fringes disappeared at a thickness less than thickness of the film at the inflection point.

Let's look back to the theoretical arguments on the moving contact line. It was mentioned in chapter 1 that there exists a paradox in the moving contact line. If the liquid is considered Newtonian and the "no-slip" boundary condition is applied at the solid surface, the velocity field at the contact line become multivalued. A non-integrable stress is produced at the contact line, which leads to an infinite force at that location. However, this can not be a real singularity because we experience the spreading process in the everyday life. For example, if an infinite force existed at the moving contact line, then it was impossible fill up a glass with water.

This singularity is particularly very serious since it does not permit the specification of a boundary-value problem.

This problem can be removed and the force made finite by making some ad hoc assumptions [35, 69]. The simplest way of eliminating the singularity is to assume slip occurs at the immediate vicinity of the contact line. This means the velocity at the moving contact line u_s is non-zero and assumed to be $u_s = \ell_{slip} du/dy$ where ℓ_{slip} is the slip length. In the region far from the contact line however, no-slip condition still holds. The region close to contact line, in which slip boundary condition is applied, is usually called the *inner region.* The region in which no-slip boundary condition is applied is called the *outer region.* An *intermediate region* is required to properly match the inner and outer regions [25, 58, 116]. To date, Cox [25, 24]

Table 3.1: Experimental and analytical results published of the last 40 years on the power-law relationship between the apparent contact angle and spreading velocity (or capillary number) of spreading viscous drops.

$\theta_a = k_1 Ca^n$	k_1	n	Ca	Liquid/Substrate	Notes
Rose & Heins (1962)	3.4	1/3	Up to 6×10^{-3}	Oleic acid	Capillary tube
Friz (1965)	3.4	1/3	————————	————————	Theoretical, prewetted surface
Schwartz & Tejada (1972)	3.4	1/3	Up to 1	different liquids/solids	Capillary tube
Hoffman (1975)	4.54	0.35	4×10^{-5}-36	Si oil on Glass	Capillary tube
Tanner (1979)	3.20	1/3	5×10^{-6}-6.5×10^{-4}	Si oil on Glass	Different values of k_1 are calculated from paper
	3.00	1/3			
	3.40	1/3			
	3.10	1/3			
	3.70	1/3			
	3.24	1/3			
Ngan & Dussan (1982)	3.41	0.31	3.8×10^{-3}–2×10^{-2}	Si oil on glass	Between flat plates, 0.01 cm gap
	4.44	0.36	5×10^{-3}–1.8×10^{-2}		Between flat plates, 0.07 cm gap
	3.90	0.35	6×10^{-3}–2×10^{-2}		Between flat plates, 0.12 cm gap
Ausserré et al (1986)	3.12	0.333	1×10^{-6}–1×10^{-2}	PDMS on Si	Different values of k_1 is calculated from their results
	3.37	0.333			
	3.11	0.333			
	4.87	0.333			
	2.66	0.333			
Chen (1988)	3.9	0.35	1×10^{-5}–1×10^{-3}	PDMS on Si	
Chen & Wada (1992)	7.1	0.39			
	3.33	0.333			
	3.85	0.333			
Ehrhard (1993)	3.19	0.36	$\sim 1 \times 10^{-4}$	Si oil & parafin/glass	Capillary tube
Marsh et al (1993)	5.17	0.35	Up to 1×10^{-2}	PDMS on Pyrex	Force wetting, plunging pipe
Starov et al (1994)	4.1	0.333	————	————	Theoretical
Schonhorn et al (1966)	24.6	0.63	1×10^{-3}–1×10^{-2}	Ethylene-vinyl acetate on aluminum at $170^{\circ C}$	Polymer melt,0.02 g drop
	22.0	0.56			Polymer melt,0.0055 g drop

performed the most comprehensive analysis of this problem with the three region model. For perfectly wetting liquids with small dynamic contact angles Cox's results can be simplified to:

$$\theta_a = \left(9Ca \ln(\frac{1}{\epsilon_s})\right)^{1/3} \tag{3.45}$$

where ϵ_s is the ratio of the slip length to the characteristic length scale of the flow (ℓ_{cap}). This ratio is always less than unity as $\ell_{slip} < \ell_{cap}$. The typical values of ϵ_s that equation 3.45 becomes the HVT law is 10^{-4} [69]. As it can be seen in the equation 3.45, there is a logarithmic correction in this relation which depends on the flow characteristics and the slip length. Equation 3.45 may be able to answer the question of inconsistency among the experimental results but there are still doubt about the assumption made in this analysis. The slip length in this problem has been subject of debate among the researchers. A comprehensive discussion on the modified HVT law using the slip length is given by Kistler [69] and Eggers & Stone[37].

Another approach to resolving this problem is presented by de Gennes [30]. By including microscopic effects close to the contact line, de Gennes was able to derive a modification to the HVT's law. The analyses assume that long range fluid/solid interactions (van der Waal's interactions) furnish the sole driving force for the precursor film, and that the film remains sufficiently thick so that the molecular structure and topology of the interfaces is unimportant and continuum theory remains applicable. In this case, the net aggregate of all fluid/solid interactions as a function of thickness can be lumped into the disjoining pressure, Π, that was first introduced by Derjaguin [32]. By inclusion of van der Waals forces to the hydrodynamic model [52], the governing equation for the thickness of the drop is found to be:

$$3Ca = h^2 \frac{d}{dx}\left(\frac{d^2h}{dx^2} + \frac{A}{6\pi\sigma h^3}\right) \tag{3.46}$$

where h is the thickness of the film, x is the horizontal coordinate (same as r in equation 3.25), Ca is the capillary number based of the spreading velocity of the contact line, σ is the surface tension of the liquid, and A is the Hamaker constant for the long range interaction between solid and gas through a thin liquid film. HVT law can be derived from this nonlinear lubrication equation by neglecting van der Waals forces so that a balance of capillary pressure and viscous stress in the vicinity of the advancing contact line gives $h^2 d^3h/dx^3 = 3Ca$. This equation has the property that $h(x)$ has an inflection point (denoted h_i) near the intersection with the precursor film. The existence of this inflection point is a requirement for drops with small apparent contact angles and provides a connection between the inner macroscopic region near the tongue and the outer macroscopic region as it was shown in section 3.3.2.

More on the precursor layer and analysis in this regard will be discussed in the chapter 4. In the mean time, the equation 3.46 is used to derive a modified relation to the HVT law. Let's pick appropriate length scales to non-dimensionalize the equation 3.46. If $X = x/x_0$ and $H = h/h_0$ where

$$x_0 = 3^{-1/6}\ell_{mic}Ca^{-2/3} \tag{3.47}$$

$$h_0 = 3^{1/6}\ell_{mic}Ca^{-1/3} \tag{3.48}$$

and the microscopic length scale of the drop, ℓ_{mic}, is defined as [30]:

$$\ell_{mic} \equiv \sqrt{\frac{A}{6\pi\sigma}} \tag{3.49}$$

The dimensionless form of the equation 3.46 using these length scales is:

$$H^{-2}\frac{dH}{dX} - H^2\frac{d^3H}{dX^3} = 1 \tag{3.50}$$

At large distance from the contact line, the van der Waals forces are negligible compared to the capillary forces. There is a particular solution to this equation that has zero curvature for large H [52]. This part of the profile, which is usually called the *wedge region* has the asymptotic form of

$$H \to X\left(3\ln(\frac{X}{X_0})\right)^{1/3} \tag{3.51}$$

The constant cut off length, X_0, is determined by matching equation 3.51 with the appropriate solution for the precursor layer. Hervet & de Gennes used asymptotic techniques and found a solution that matches the macroscopic solution at the wedge

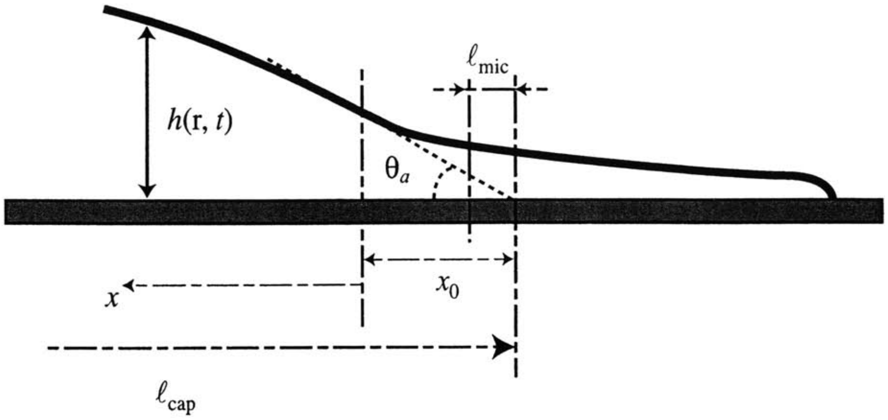

Figure 3-5: Different length scales at the vicinity of the moving contact line.

region (zero curvature region). The value of the constant, X_0, is calculated to be equal to 2.5. The most important part of this analysis is the dynamic contact angle, θ_a, defined as the slope of the free surface at the inflection point which is found to be:

$$\theta_a \equiv \left(\frac{dh}{dx}\right)_i \simeq (3fCa)^{1/3} \tag{3.52}$$

where

$$f \equiv 3\ln(0.4X) = 3\ln\left(\frac{0.4x}{x_0}\right) \tag{3.53}$$

By substituting x_0 from equation 3.47, the modified HVT law becomes:

$$\theta_a = \left(9Ca\ln\left(\frac{0.4x}{\ell_{mic}}Ca^{2/3}\right)\right)^{1/3} \tag{3.54}$$

In equation 3.54, x is the macroscopic matching distance from the the contact line where the inner microscopic profile matches the the outer macroscopic profile. From this point on, we call this length the macroscopic length, ℓ_{mac}. All of the important length scales in this analysis is shown in figure 3-5. The form of equation 3.54 is very similar to equation 3.45 as they both have a logarithmic term related to microscopic and macroscopic length scales. If $\epsilon_s \sim Ca^{-2/3}$ then these relations are approximately the same.

As indicated in equation 3.54, the front factor in the modified HVT law is no longer a constant and has logarithmic dependency to the capillary number ($Ca^{2/3}$). Another important note is that the location of the measured contact angle is important since the position itself (ℓ_{mac}) appears in this relation. This effect is even more important when two experimental systems with different global geometry are compared with each other. For example the existence of inflection point for the experiment of flow in the capillary tube is doubtful due to the fact that free surface profile of drop is different than a spontaneously spreading drop on a horizontal surface. Thus ℓ_{mac} is somehow arbitrary. Also this might explain the size effect which is reported in earlier wetting experiments [81].

There have been other efforts to modify the HVT law and consideration of other effects that may effect the spreading phenomena. An interesting work is the model presented by Pismen et al. [93]. This work is also based on asymptotic analysis however they were not able to confirm the numerical constant reported by Hervet & de Gennes. Instead they found this numerical constant to be dependent of geometry and other factors. They also included the effect of gravity to their analysis on the front factor in the HVT's law. The important dimensionless parameter was found to be $G = (\ell_{mic}/\ell_{cap})^2$ which is the ratio of microscopic length scale to the capillary length. We will return to this paper later in the discussion of our experimental results.

Recently, Eggers & Stone [37] have used de Gennes approach to this problem and found a similar result. They found out the numerical constant in the logarithmic term was not calculated accurately in the original work of de Gennes and they found this relation to be:

$$\theta_a = \left(9Ca \ln\left(\frac{1.44\ell_{mac}}{\ell_{mic}}Ca^{2/3}\right)\right)^{1/3} \tag{3.55}$$

They believe this difference is simply due to the large values of X necessary for integration until the true asymptotic limit is reached given by equation 3.51. There is also similar calculation by this group using the slip model in the equation that leads to the dependency of the logarithmic term to the $Ca^{1/3}$ unlike van der Waals effect ($Ca^{2/3}$). Therefore the slip length argument can not be equivalent to the van der Waals effect. No experimental evidence was reported to support the dependency to the slip length by Eggers & Stone [37].

To summarize, there have been several relations used to present the relation between the dynamic contact angle, θ_a, and capillary number, Ca for spreading of a perfectly wetting Newtonian viscous fluid over a smooth substrate. To make it easier to compare our results with the theory we rewrite these relations as following:

$$\theta_a = k_1 Ca^{1/3} \tag{3.56}$$

$$\theta_a = k_2 Ca^n \tag{3.57}$$

$$\theta_a = k_3 \left(Ca \ln \left(k_4 Ca^{2/3}\right)\right)^{1/3} \tag{3.58}$$

In equation 3.58, $k_3 = 9^{1/3}$ and $k_4 = 1.44\ell_{mac}/\ell_{mic}$ according to the most recent article by Eggers & Stone [37].

3.4 Experimental results

3.4.1 Fluids

The test fluids used in this study are constant-viscosity silicone oils with relatively low molecular (No reptation effect; cf. chapter 7) weights which are produced by Gelest Inc. There are several advantages in using these silicone oils: first, they all wet the substrates that are used in our experiments; secondly, the viscosities of these liquids are well characterized. This enables us to explore several regimes of spreading on viscous liquids on the surface. The general thermophysical properties of these liquids are given in appendix A. Rheological measurements show that test fluids have a constant viscosity for deformation rates less than 300 s^{-1}.

3.4.2 Spreading regimes

The first step in our experiments was test the capabilities of the confocal measurement system applied to the spreading drops. A viscous drop of silicone oil (DMS-T21, $Oh = 0.98$, $\phi = 0.86$) was placed on a silicon surface and by using the XY translation stage, the free surface profile of the spreading drop was scanned repeatedly as it spread. The scanning speed of the stage is 1 mm/s and is fast enough that the profile can be assumed to be quasi-steady over each scan. The results are shown in figure 3-6(a) for $t = 0, 55, 214, 255$ s after dispensing the drop. On the abscissa we show the measured distance from the center of drop, r, in millimeters and on the ordinate axis we plot the local thickness of the drop, h, in micrometers. By normalizing the height profiles by the maximum thickness at each instant, $h^* = h(r,t)/h_{max}(t)$, and the radius by the maximum radius, $R^* = r/R(t)$, all of the results of figure 6.27a collapse to form a single self-similar profile as shown in figure 3-6(b). Given this self-similarity in the spatial profile of the spreading fluid droplet, it is sufficient to monitor the temporal dynamics of the process by using the confocal system to measure the evolution in the height at a single fixed spatial position, and we employ this approach in the majority of the results we present below.

The different power-law regimes of spreading for viscous drops have been outlined and we have also validated these experimentally. Many of the previous experiments were done by observing the radius of the drop as it spreads on the substrate by using imaging systems such as CCD cameras. Our measurement system enables us to measure the local thickness of the drop and derive the associated power-law from this data. The power-law coefficients for the radial extent and local thickness are constrained by the self-similarity of the shape and conservation of mass so that at all times. There are analogous power-law relations for the inertial-capillary spreading of less-viscous drops ($Oh \ll 1$). For fluid droplets of low viscosity, the resistance to spreading from viscous stresses is negligible and inertial resistance balances the driving force of capillarity. Viscous drops ($Oh \gg 1$) spread much more slowly compared to relatively inviscid drops as expected because the large viscous forces in the thin film retard the spreading. At long times, the volume of the drop (ϕ) is not a factor since all spreading drops will eventually move to pancake regime regardless of initial size (cf. figure 3-2). Table 3.2(a) shows the approximate form of the similarity solution for spreading at low and high Ohnesorge numbers in the pancake regime. The analytical relation for h as a function of time is derived from the scaling relations

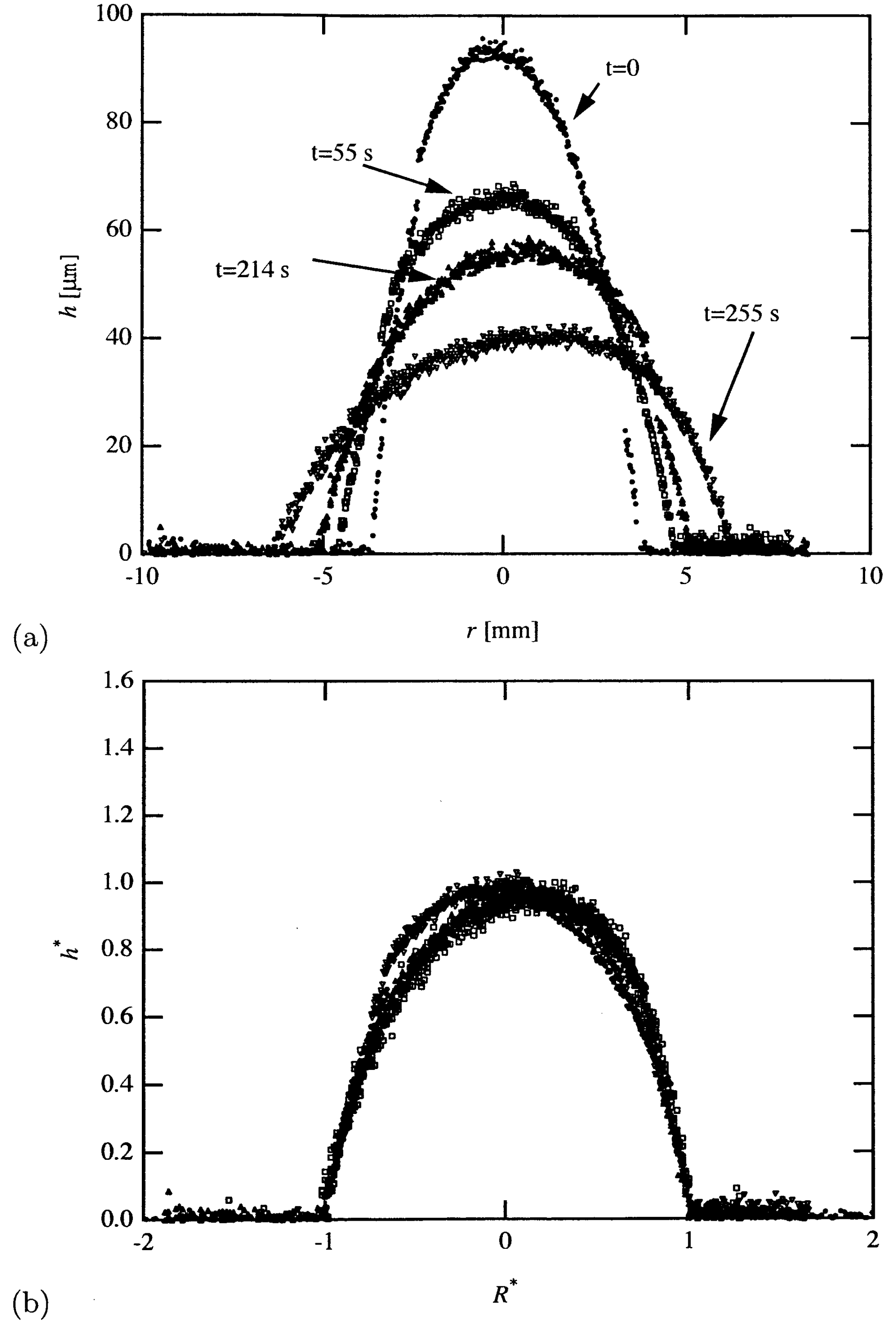

Figure 3-6: (a) Evolution of the free surface, h(r,t), of a spreading droplet of silicone oil ($Oh = 0.98$, $\phi = 0.86$) on a silicon substrate. Measurement is done by scanning the free surface at a scanning speed of $U = 1mm/s$. (b) Normalized height, $h^* = h(r,t)/h_{max}(t)$, vs. normalized lateral position, $R^* = r/R(t)$, for the same data set.

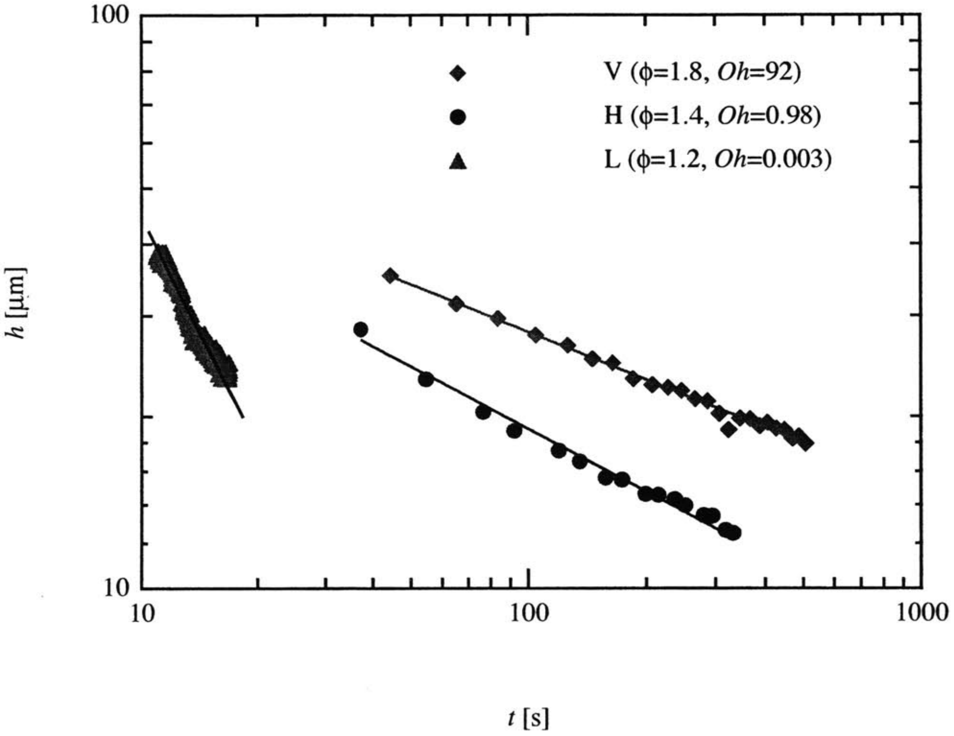

Figure 3-7: Spreading experiments of drops of silicone oils on silicone wafer substrate. Data include (◇) V ($Oh = 92, \phi = 1.8$); (□) H ($Oh = 0.98, \phi = 1.4$); (△) L ($Oh = 0.003, \phi = 1.2$). The solid lines are the best power-law regression to each data set.

Table 3.2: (a) Theoretical power-laws for viscous-capillary and inertia-capillary spreading of droplet on smooth solid surface. (b) Comparison between the analytical spreading results and the experimental spreading results in the pancake regime.

(a)

Driving force	Resisting force	Oh	Scaling form
Capillary	Viscous	$Oh \gg 1$	$h/\ell_{cap} \cong \left((\Omega/\pi)^{1/3}/\ell_{cap}\right)^{9/7}\left(t/\left(\mu\ell_{cap}/\sigma\right)\right)^{-2/7}$
Capillary	Inertia	$Oh \ll 1$	$h/\ell_{cap} \cong \left((\Omega/\pi)^{1/3}/\ell_{cap}\right)^{3}\left(t/\sqrt{\rho\ell_{cap}^{3}/\sigma}\right)^{-4/3}$

(b)

Liquid	Oh	Analytical result	Experimental result
L	0.003	$A = 2.32$, $B = -1.33$	$A = 2.97$, $B = -1.28$
H	0.98	NA	$A = 2.00$, $B = -0.36$
V	92	$A = 0.71$, $B = -0.28$	$A = 0.56$, $B = -0.28$

Power-law has the form of $h/\ell_{cap} \simeq At^{*B}$. Data include (◇) V ($Oh = 92$,$\phi = 1.8$); (□) H ($Oh = 0.98$,$\phi = 1.4$); (△) L ($Oh = 0.003$,$\phi = 1.2$).

for radius and by assuming the volume of drop remains constant during the spreading ($\Omega \simeq \pi h(t)R(t)^2/2$). In figure 3-7 we show experimental spreading results for three different silicone oils with small, medium, and large Ohnesorge numbers. The fluids used in this experiments are silicone oils with low (L), high (H), and very high (V) viscosities. The rheological properties of these fluids are reported in appendix A. The vertical axis of the plot shows the local thickness of the film $h(t)$, which is measured by a confocal surface metrology system (chapter 2), , and the horizontal axis of this plot is elapsed time. For silicone oil droplets spreading at very large Ohnesorge number (V, $Oh = 92$, $\phi = 1.8$), the analytical power-law result in table 3.2 is of the form $h/\ell_{cap} = A(t/(\mu\ell_{cap}/\sigma))^{-2/7}$. For the silicone oil with lowest Ohnesorge number (L, $Oh = 0.003$, $\phi = 1.2$), the analytical form of the power-law in the pancake regime is $h/\ell_{cap} = A(t/\sqrt{\rho R^3/\sigma})^{-4/3}$ as shown in table refpowerlaws(a). These power-law relations are derived from the radius power-laws, previously driven in section 3.3, and using the conservation of mass to find the relation for thickness ($h = \Omega/2\pi R^2$). Linear regression of a power law to the experimental results shows that these forms of spreading equations accurately describe the experimental observations. The power-law coefficients and the front factors obtained from experiments and from theory are shown in table 3.2(b). For fluids with intermediate Ohnesorge numbers close to one (e.g. H, $Oh = 0.98$, $\phi = 1.4$), there is no analytical power-law form available for the evolution of a spreading drop since viscous, capillary and inertial effects are all equally important. However, the power-law coefficient may be expected to lie between the two extreme cases described above. The values obtained from the experiment confirm that the power law coefficient for viscous-inertial spreading of a drop lies between the limiting values of inertia-capillary and viscous-capillary spreading.

3.4.3 Experimental results of dynamic contact angle

In this section, the characterization of the dynamic contact angle, θ_a, in the spreading process is presented. We have used the psLFI system (chapter 2) to measure the free surface profile of the moving drop close to the contact line. We have used the same experimental geometry as earlier investigations [4, 21] and consider well-characterized silicone oils spreading on polished silicon wafers. First, we deposit a drop of silicone oil of a known volume on a cleaned silicon wafer using a syringe pump (Harvard Apparatus, pump 11). When the advancing contact line of the spontaneously wetting drop moves below the focal point of the objective lens its instantaneous rate of spreading, $\dot{R}$, is measured using a CCD camera and the profile, $h(t)$, is measured interferometrically. Knowing the local speed of the wetting line, the profile of the drop, $h(t)$, is converted to $h(x)$ via a simple Gallilean transformation. The spreading velocity of the drop is a time-varying function that depends on the drop size and the dominant driving and resisting forces. The drops used in the present experiments have a volume $V = 10\mu$L ($\phi = 0.92$) and initially assume the shape of a spherical cap, which spreads such that $R \sim t^{1/10}$ (section 3.3), but ultimately evolve to a pancake regime which follows the same power-law relation shown table 3.2. All of our measurements are performed when the drops are in the final pancake regime. A number of different silicone fluids have been used in our experiments in order to generate results for a wide range of capillary numbers. These materials are supplied by Gelest Inc. and have constant shear viscosities spanning the range $7 \times 10^{-3} < \mu < 10.0$ Pa.s. The surface tension, σ, of these silicone liquids vary weakly with increasing molecular weight but are in the range of 19×10^{3} - 21×10^{3} N/m. Further details of the rheological properties are provided in appendix A.

A representative drop profile ($\phi = 0.9$; $Oh = 6.22$) is presented in figure 3-8, where the abscissa represents the lateral displacement (x) of the front and the left ordinate shows the measured value of the decrease in optical path length (or local thickness of the drop, $h(x)$) in micrometers. The fluid front passes through the measuring volume and the macroscopic profile of the drop can be accurately imaged. Rather than assuming a model-dependent drop profile, the local slope was determined by a direct numerical differentiation of the profile $h(x)$ using a fifth order Gram polynomial [120] that minimizes amplification of experimental noise. The resulting values of dh/dx are shown on the right vertical axis. As shown in figure 3-8, at $Ca = 7 \times 10^{-4}$, the slope dh/dx has a maximum value at a distance of $13\mu m$ from the moving contact line, corresponding to an inflection point of the drop profile. By definition [79, 93], this point separates the inner region of microscopic physics from the outer or macroscopic domain which was discussed in section 3.3.2. The macroscopic dynamic contact angle is conventionally defined [79] as $max[\arctan dh/dx]$ and we can thus determine unambiguously a precise value for θ_a. As the spreading proceeds, the capillary number falls and the maximum slope or apparent contact angle decreases [4] as $\theta_a \sim t^{-0.3}$.

In figure 3-9(a), we show the variation in the measured dynamic contact angle θ_a (in radians) as a function of the capillary number for $2 \times 10^{-6} < Ca < 3.2 \times 10^{-4}$. We were able to get a range of Ca in one experiment by several measurement of the dynamic contact angle during the spreading at different times. It was shown (section 3.3) that $R \sim t^{1/7}$ for the pancake region. Therefore the spread of spreading has a power-law of $\dot{R} \sim t^{-6/7}$. This indicates that the velocity of spreading and therefore capillary number decreases in time and each spreading drop provided us

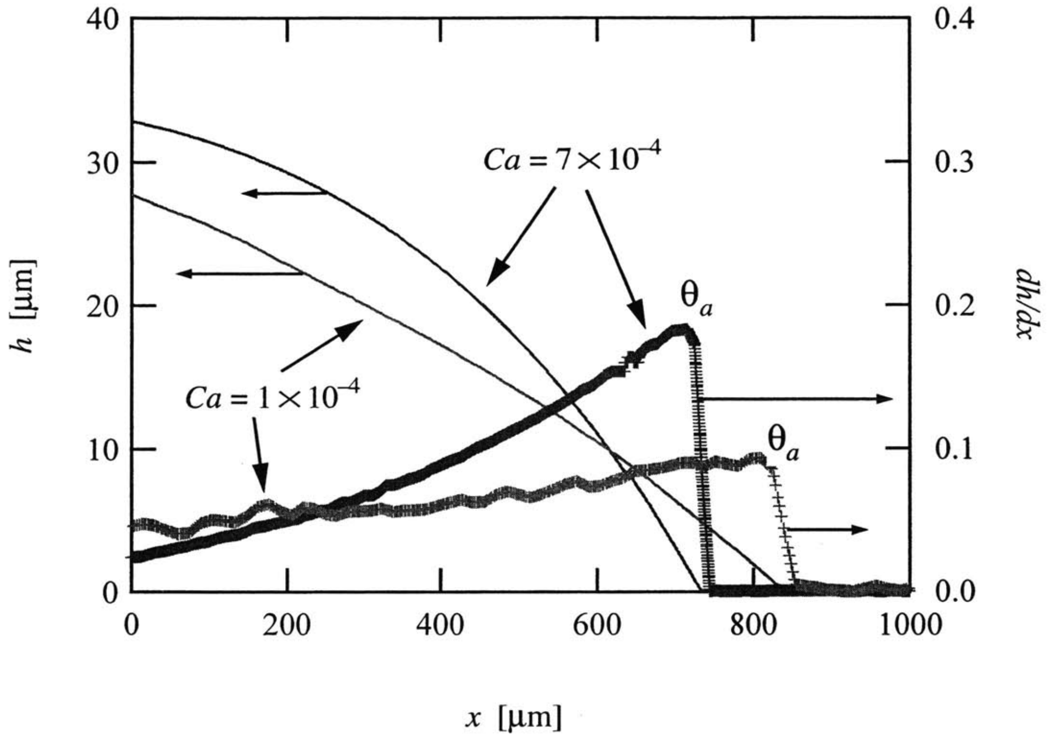

Figure 3-8: Free surface profile, $h(x)$, and the spatial derivative, dh/dx for different values of capillary number ($Ca = 1 \times 10^{-4}$ and $Ca = 7 \times 10^{-4}$) for a spreading viscous drop ($\phi = 0.9$; $Oh = 6.22$). The maximum value of the slope corresponds to the macroscopic dynamic contact angle, θ_a.

with a range of capillary numbers. Numerous functional forms for the variation in θ_a with Ca have been proposed in the literature and can be compared impartially with this data (section 3.3.2). Direct regression to the Hoffman-Voinov-Tanner law (HVT; $\theta_a = k_1 Ca^{1/3}$) gives $k_1 = 1.92 \pm 0.04$ with a confidence level of $R^2 = 0.968$ and is shown by the broken line. Careful examination shows that in fact there is a systematic deviation from this line. A better fit to the data set is given by a somewhat stronger power-law, $\theta_a = k_2 Ca^n$ with $k_2 = 3.4 \pm 0.4$ and $n = 0.39 \pm 0.01$ (at a confidence level of $R^2 = 0.986$). Previous experiments have also noted a power law exponent exceeding $n = 1/3$ [110, 21] as shown in table 3.1. However, as noted first by de Gennes [30], there is in fact a weak logarithmic dependency of the numerical coefficient k_1 on the speed of the spreading drop. A more detailed treatment [37] gives an equation of the functional form of equation 3.58 with $k_4 = \ell_{mac}/\ell_{mic}$. Here ℓ_{mac} is a characteristic matching length where the inner microscopic profile matches the outer macroscopic profile of the drop. Regression to this form is shown by the solid line in figure 3-9a and yields $k_3 = 1.2 \pm 0.7$ and $k_4 = 32450 \pm 23276$ with a confidence level of $R^2 = 0.987$. This dependence is clearer when data is plotted in semi-log scale for θ_a^3/Ca as a function of Ca as shown in figure 3-9(b). The slope of the solid line, which is the regression to the data, is approximately 1/3 which is another evidence to the effect of capillary number on the logarithmic correction.

It therefore appears that this logarithmic dependence is the correct functional form to be used as a correction to HVT's law which becomes increasingly important at small Ca. A recent computation [37] suggests that $k_4 = 1.44\ell_{mac}/\ell_{mic}$ as the matching length can be calculated by substituting values of ℓ_{mic} (chapter 4) and k_4 in this relation as shown in equation 3.55. We find $\ell_{mac} \simeq 14\mu$m which, according to our measurements, is the average distance from the inflection point to the intersection of the macroscopic region and the precursor layer (chapter 4) for the range of capillary numbers in our experiments. This length scale is large with respect to the microscopic region (ℓ_{mic}) but still small with respect to outer scales such as the capillary length ($\ell_{cap} = 1.4$ mm) or the Landau-Levich-Deryagiun length $\ell_{LLD} \simeq \ell_{cap} Ca^{1/3}$ which is important in forced wetting problems [37].

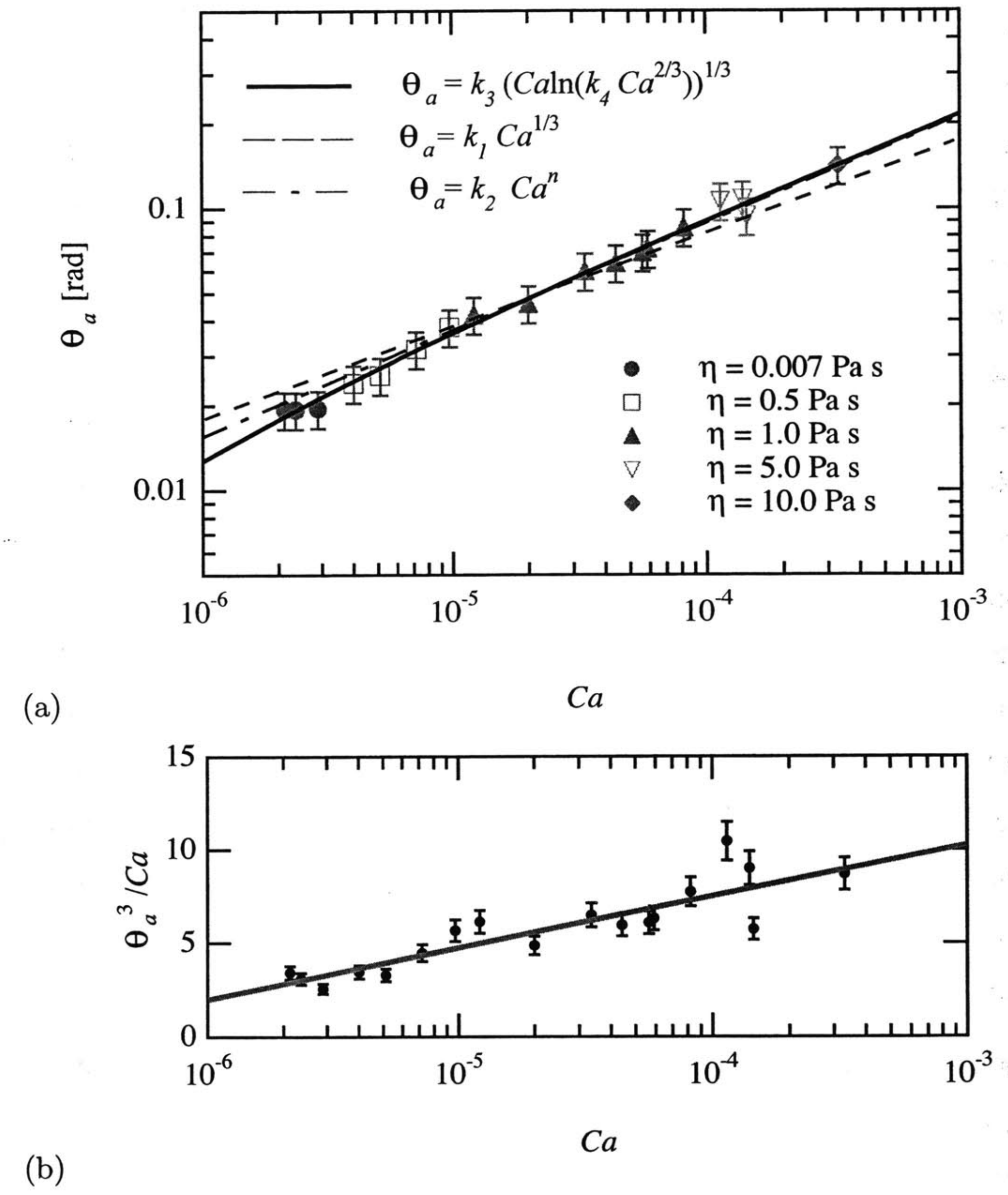

Figure 3-9: (a)Dynamic contact angle, θ_a, as a function of capillary number. Dashed line (— — —) is the regression to the experimental data following HVTs law, $\theta_a = k_1 Ca^{1/3}$. Dashed dot line is a regression to the experimental data of form, $\theta_a = k_2 Ca^n$. The solid line is a regression to the experimental data using the de Gennes model, $\theta_a = k_3 \left(Ca \ln\left(k_4 Ca^{2/3}\right)\right)^{1/3}$. (b) deGennes model fit to the same set of data (solid line) when the reduced angle θ_a^3/Ca is plotted as a function of $\log Ca$. The slope of the solid line is 1/3.

In original asymptotic theories [30, 37] the front factor in the spreading law is determined from the wedge flow in the intermediate matching region to be $k_3 = 9^{1/3} = 2.08$. Our experiments yield a smaller value that is consistent with earlier experiments in the same system [4]. This so-called size effect [69, 81] arises from two distinct physical phenomena; (i) the additional curvature resulting from the geometry of the spherical caps formed by the very small fluid droplets and (ii) the coupling between the inner and outer scales. The latter effect was demonstrated by recent simulations [93] which show that the front factor varies systematically with the van der Waals number $G = (\ell_{mic}/\ell_{cap})^2$. For the present silicone/silicon system $G = (6.1 \times 10^{-10}/1.4 \times 10^{-3})^2 \simeq 1.8 \times 10^{-13}$. We have performed additional experiments using two-dimensional silicon strips [78]. In these experiments, a viscous drop spreads only along the strip instead of radial spreading. These experiments yield a somewhat larger front factor, $k_3' = 1.7 \pm 0.35$. These results are shown in figure 3-10. The regression to this data leads to $k_4' = 15455 \pm 1460$ with a confidence level of $R^2 = 0.977$.

3.5 Discussion

In this chapter, we have investigated the steady spreading of perfectly wetting viscous liquid drops on solid substrates. We have reviewed the important parameters in this phenomena and how they can affect the system. The drop volume, surface tension, viscosity, and density of the liquid all have profound effects on the spreading process. Depending on the importance of these parameters or some combination of them, different dynamical regimes of spreading are present in the process. The drop size and its value compared to the capillary length of the drop, ϕ, can dictate whether the gravitational forces are of importance or not. Also inertia, viscous and the capillarity forces may act as resisting force or driving force.

Three dynamical spreading regimes have been introduced in this chapter. The gravity current, spherical cap, and the pancake regions develop depending on the drop size and the relevant driving and resisting forces in the process. When the drop characteristic size, ϕ, is larger than unity and Ohnesorge number is large ($Oh \gg 1$),

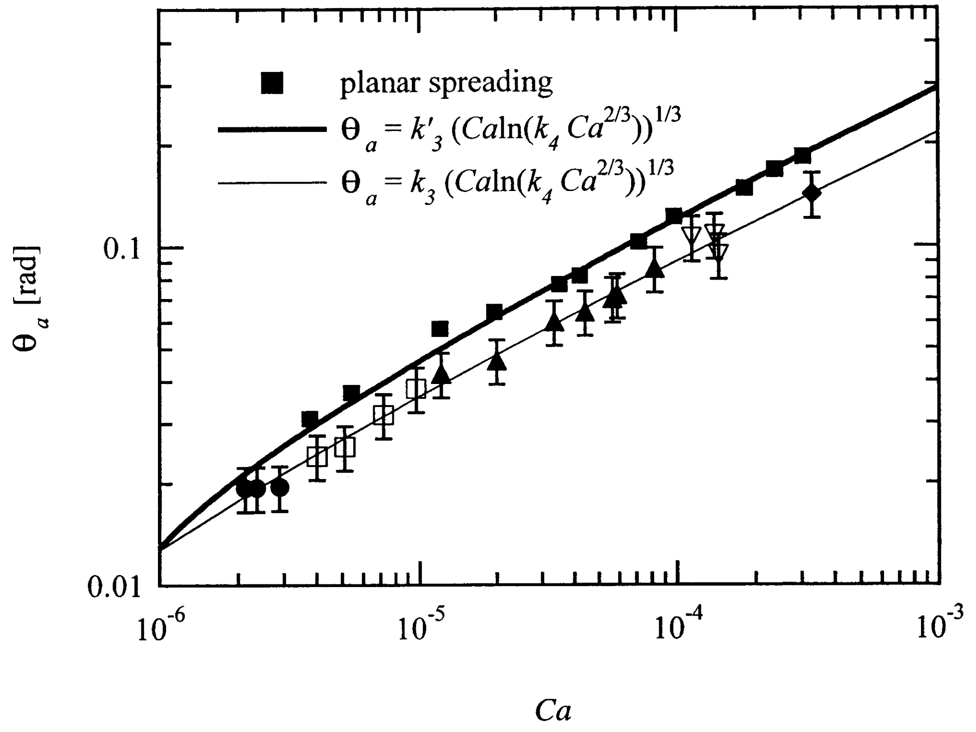

Figure 3-10: Dynamic contact angle, θ_a, as a function of capillary number for spreading of drop ($\phi = 0.9$, $Oh \gg 1$) on silicon strip (2-dimensional spreading) is shown with symbol (□). The thick solid line is a regression to the de Gennes model. The result of the axisymmetric spreading (from figure 3-9) are also plotted for comparison.

then gravitational force is important in the spreading and acts as the driving force in spreading. While viscous force resists the spreading, the capillary force can be neglected. The spreading rate, $\dot{R}$, and the power-law function of radius of drop, $R(t)$ as a function of time can be found either by directly solving the Navier-Stokes equation or by using the scaling analysis. The analysis leads to $R(t) \sim t^{1/8}$ relation which are confirmed by previous works as well (figure 3-2).

If $\phi \ll 1$ and $Oh \gg 1$, the drop size is small compared to the capillary length. This means the gravitational force are not important in this process. The droplet shape is set by the Laplace equation which for small drops leads to a spherical cap shape. The capillary force acts as the driving force and the viscous force is the resisting for in the spreading process. The analytical solution (as well as the scaling analysis) leads to the well known power-law for this regime as $R(t) \sim t^{1/10}$.

When $Oh \ll 1$, the viscous forces can be neglected and instead it is the inertia that resists the spreading. This usually happens in the very early stages of spreading when a drop is deposited on the the solid surface. The power-law relation for this regime is found to be $R(t) \sim t^{2/3}$.

Almost all of the above mentioned regimes will ultimately evolve to a 'pancake' regime. In this regime, the radius of the spreading drop is much larger than the capillary length and the spreading drop has the shape of a pancake (constant thickness almost everywhere except near the rim). The thickness reduces to reach the contact line near the rim over a distance of order ℓ_{cap}. The driving force is capillarity and viscous force is the resistance. Gravity only acts as a hydrostatic force in the central pancake region. From the scaling analysis, the power-law of the spreading is of the form of $R(t) \sim t^{1/7}$.

It is noteworthy that because of the conservation of mass in the spreading drop ($\Omega \sim hR^2$), similar power-laws can be found for $h(t)$ by substituting $R(t)^2 \sim \Omega/h$ in the above mentioned power-laws. The dynamic contact angle can be scales as $\theta_a \sim h(t)/R(t)$ for first order approximation.

The relationship between the dynamic contact angle and capillary number is called the Hoffman-Voinov-Tanner law (HVT). This power-law relation $\theta_a \sim Ca^{1/3}$ is valid when the gravitational effect are negligible, $h, R \ll \ell_c ap$, which means in pancake or spherical cap regions in figure 3-2.

We have also applied a non-invasive phase-shifting laser feedback interference microscope to investigate the evolution of moving contact lines in dry spreading of perfectly wetting van der Waals fluids. The system has sufficient resolution and dynamic range to resolve details of both the physics of the inner (microscopic) interfacial region and its interconnection to the outer (macroscopic) fluid response. The coupling between these regimes that is revealed by the experimental measurements is in good agreement with theoretical predictions and numerical simulation. The variation in apparent contact angle with Ca is roughly consistent with the Hoffman-Voinov-Tanner relationship; however careful examination shows the clear existence of a logarithmic dependence on the spreading velocity or capillary number as predicted previously by de Gennes [30]. We shown that the measured contact angles for spreading of fluids on strips have better agreement (especially the front factor, k_3') with the HVT's law which can be due to the so-called "size effect".

It is obvious from these results that there exists a very important relation between the microscopic and macroscopic part of the spreading drop. The existence of the inflection point as a linking point between the microscopic and macroscopic regions, and the logarithmic modification to the HVT law which is due to the microscopic effects, motivate us to characterize the microscopic region of the moving contact line. In the next chapter, the characteristic of this region specially the *precursor film* will be presented.

Chapter 4

Characteristics of the precursor film for spreading Newtonian fluids

4.1 Introduction

In chapter 3, the macroscopic features of spreading viscous drops have been thoroughly investigated. We have pointed out the important parameters in the wetting process and how they affect the spreading dynamics. The relationships for different spreading regimes and the Hoffman-Voinov-Tanner law were derived from the balances between different forces acting in this problem. However, the singularity at the moving contact line can not be removed unless microscopic parameters at the region very close to the contact line effects the spreading dynamics. At the end of the chapter 3, the logarithmic correction to the HVT law was presented and our experiments and theoretical results [30, 37] have shown that the microscopic length scales are involved in this correction. A common way of removing the singularity at the moving contact line is the assumption of spreading of the drop on a pre-wetted surface [69]. This is possible if a microscopic film spreads spontaneous in front of the moving contact line. The film thickness at the contact line is not zero and the singularity is removed. The velocity slip at moving contact line was mentioned in chapter 3 (equation 3.45), however we would like to investigate the existence of a microscopic feature at the moving contact line which is commonly called the *precursor film.*

For systems in which the fluid spreads spontaneously to give a zero equilibrium contact angle ($S > 0$; equation 1.2), the precursor film (or precursor layer) is a microscopic film which moves ahead of the contact line and pre-wets the solid surface. Existence of this layer prevent the singularity at the contact line since the thickness of the film does not go to zero at the contact line. Thus, the velocity is not multivalued and the resulting viscous force at the moving contact line is bounded. Precursor films form when the thickness of drop becomes small enough that the intermolecular forces of attraction between the solid and liquid are strong enough to to generate a positive spreading coefficient, S, (equation 1.2) and disjoining pressure. These forces provide the driving force for spreading. The released energy is dissipated by the viscous forces in the thin film [30]. A pressure gradient is generated between the bulk of the liquid and the fluid close to the contact line by the disjoining pressure. This pressure gradient draws the liquid out of the bulk and pulls it into the precursor film. An important feature of existence of a precursor film in wetting processes is that flow within the film is approximately one-dimensional ($h \ll R$) and can be described by a lubrication analysis. The spreading of the bulk liquid is effectively decoupled from the motion of the wetting line, and is independent of the spreading coefficient, S, for perfectly wetting fluids. This has been well-documented both experimentally and theoretically [30, 69].

Hardy's experimental work [49] provided the first observation of a very thin film in front of a spreading wetting line on solid surfaces. Numerous studies have subsequently confirmed the existence of precursor films using ellipsometry, interference patterns, and polarized reflection microscopy. From this point of time, there have been a few experimental, numerical, and analytical studies on the precursor films. Bascom et al. [6] used the interference patterns on spreading of fluids on the metal surfaces and reported a thin layer of liquid in front of the moving contact line. Ellipsometry is another vastly used measurement system in the precursor film experiments. In experimental work performed by Heslot et al. [55, 54, 53], Valignat et al. [115], Léger et al. [73], and Beaglehole [7], ellipsometry have been used to quantify this film. However the dynamic range of this system only allowed them to measure the

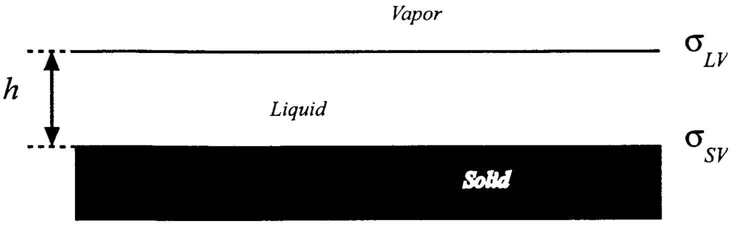

Figure 4-1: A liquid film on a solid surface.

thicknesses up to 500Åwhich prevented them to match their measurements in the nanoscale to the macroscopic part of the drop. The polarized reflection microscopy was used by Léger et al. [73] to detect a precursor films in front of the moving contact line. All of these systems lacked the spatial resolution required to measure the length of the precursor film in the earlier stages of spreading. Therefore, almost all of these experiment were performed after a long time after the deposition of the drop. In the next section, we will review the theoretical analyses that predict two different regimes for the precursor films (an 'early time' and 'late time'). Most of these experiments only investigated the film which appears at the later stages of spreading. X-ray reflectivity is another method that was used by Daillant et al. [26] to probe the precursor films but this method also lacks the dynamic range desired for this problem. Finally, numerical simulations [118, 117, 12] have modeled the spreading of long chain polymers to characterize the precursor films.

In this chapter, we review the available analytical results and prediction of the two regimes of precursor films. Our measurement of the precursor films using the psLFI system will be presented and these experimental results will be compared with analytical predictions.

4.2 Theoretical predictions

When the thickness of a liquid film approaches the molecular dimensions, 'long range' molecular forces must be considered in the analysis of the liquid films. Here, this issue will be explained as it is first described by Joanny & de Gennes [68].

In figure 4-1, an schematic of a liquid film on a solid surface is shown. The free energy per unit area between the vapor and the solid through the liquid film, F, is in form of:

$$F = \sigma_{SL} + \sigma_{LV} \tag{4.1}$$

where σ_{SL} and σ_{LV} are the solid-liquid and liquid vapor surface tensions, respectively. As it seen from the equation 4.1, the free energy, F, does not depend on the thickness of the liquid film. This assumption is valid as long as the boundaries between liquid-solid and liquid-vapor can be considered as interfaces. However, in reality these boundaries are interphases in which the liquid molecules exhibit variations in density and orientation as they move around. If the thickness of the film, h, is small enough, these molecular interactions overlap in the sense that the molecules at liquid-solid interphase can interact with the those at the liquid-vapor interphase. Thus, we can rewrite equation 4.1 to include the thickness dependent of the force which leads to the following equation:

$$F = \sigma_{SL} + \sigma_{LV} + \Phi(h) \tag{4.2}$$

The form of the function $\Phi(h)$ depends on the fluid properties such as polarity of the molecules. The most common form of this function for the non-retarded London van der Waals interaction fluids can be written as [79]:

$$\Phi(h) = \frac{A}{12\pi h^2} \tag{4.3}$$

The constant A, is called the Hamaker constant and it depends on the properties of the three phases of material. This model can be used for a non-volatile and non-polar oils on metal surfaces [79]. For more complex materials such as water, where the possibility of double layer interaction exists, a much more complicated relation must be used [56].

A "disjoining pressure" arises from the interfaces of the ultrathin films since the above mentioned interactions can generate pressure contributions within the liquid film. The disjoining pressure $\Pi(h)$ can be calculated as:

$$\Pi(h) = -\frac{d\Phi}{dh} \tag{4.4}$$

so the disjoining pressure is the free energy of a film with thickness h, relative to the bulk liquid on the surface where $\Pi \to 0$ (for larger thickness h). Combining equations 4.3 and 4.4 results in the relation between the disjoining pressure and the thickness of the film:

$$\Pi(h) = \frac{A}{6\pi h^3} \tag{4.5}$$

When the film thickness h decreases, equation 4.5 predicts an increase in the disjoining pressure. This means the free energy increases and for very thin films in the atomic scale, this is energetically disfavored. Therefore, it is expected that the van der Waals forces could support a finite film thickness. This would not be valid for the analysis with the continuum assumption.

Let's try to find this minimum thickness for the ultrathin liquid film on a solid surface. The free surface energy difference per covered area between the dry surface and the wetted surface is

$$S = \sigma_{SV} - (\sigma_{SL} + \sigma_{LV}) \tag{4.6}$$

where σ_{SV} is the solid-vapor surface tension. The free surface energy is positive when the wet surface is energetically favored because of a lower energy compared to the dry surface. A liquid drop would spread spontaneously on a dry surface if $S > 0$ as discussed in chapter 1. The static equilibrium contact angle will be equal to zero. For a drop spreading on a surface, the free energy can be written as:

$$E = (F - \sigma_{SV})\mathbf{A} = (\Phi(h) - S)\mathbf{A} = (\Phi(h) - S)\frac{\mathbf{V}}{h} \tag{4.7}$$

where $\mathbf{A}$ is the wetted area which is approximately equal to the volume of the drop, $\mathbf{V}$, divided by its thickness, h.

The minimum thickness of a liquid layer can be calculated by minimizing the free energy of the liquid film. At the minimum thickness, the free energy is given by $dE/dh = 0$. From equation 4.7, the following relation for the spreading parameter can be written:

$$S = \Phi(h) - h\Pi(h) = \frac{3}{2}\frac{A}{6\pi h^2} \tag{4.8}$$

By substituting for A from the equation 3.49, the minimum thickness allowed is found to be:

$$h_{min} = \ell_{mic}\sqrt{\frac{3\sigma}{2S}} \tag{4.9}$$

where ℓ_{mic} is the microscopic length scale of the liquid drop from equation 3.49 and σ is same as σ_{LV}.

Now that the minimum thickness allowed by the molecular forces is estimated, one can look closer to the precursor film. By knowing the minimum thickness, the thickness of the location that the precursor film is truncated is found. It is also known that the precursor film must match with the macroscopic profile of the drop close to the inflection point as it was pointed out in chapter 3. The precursor films are assumed to have two main regions [68]. The section of the film that starts from the macroscopic part of the drop (inflection point) and moves with a constant velocity with respect to the stationary coordinate (or solid surface) is called the *adiabatic* precursor film. However, there is another part of the film which spreads as a diffusive front and is called the *diffusive* film. In the next two sections, these regimes will be discussed.

4.2.1 Adiabatic precursor film

The effect of molecular forces was included to the calculation for the free surface profile of the spreading viscous drop (equation 3.46) by Hervet & de Gennes [52] to calculate the profile of the drop in the vicinity of the contact line. Due to the flatness of the precursor film, the first term in the right hand side of equation 3.46 which represents the curvature of the free surface can be neglected. The profile of the precursor film is governed by:

$$Ca = \frac{\ell_{mic}^2}{h^2}\frac{dh}{dx} \tag{4.10}$$

Integration of equation 4.10 would give us the film profile as:

$$h(x) = -\frac{\ell_{mic}^2}{Ca}\frac{1}{x} \tag{4.11}$$

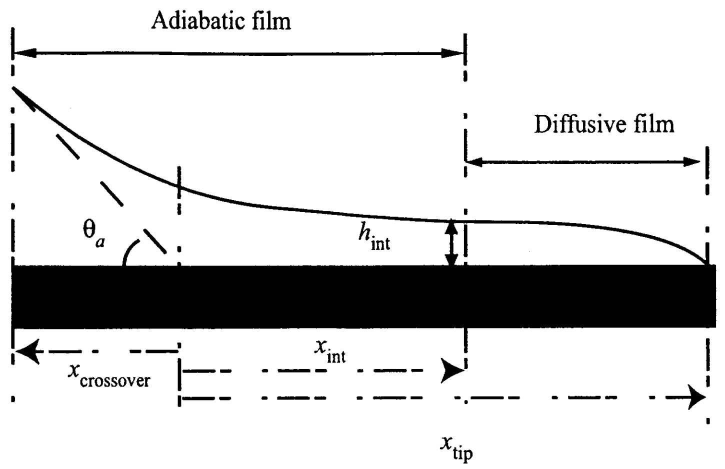

Figure 4-2: A schematic of a mixed precursor. The adiabatic film is moving with the same velocity as the average velocity of the macroscopic front but the diffusive films moves with different speed from the front.

The length of the precursor film, L_P, is the the distance from the crossover between the macroscopic and microscopic profiles (approximately the inflection point of the profile) to the tip of the film where it is truncated by the molecular force. The thickness of the film at these points are $h_{crossover}$ and h_{min}, respectively. It is important to note that $h_{crossover} \gg h_{min}$.

By using equation 4.11, we can calculate L_P as:

$$L_p = x_{tip} - x_{crossover} = \frac{\ell^2_{mic}}{Ca}\left(\frac{1}{h_{min}} - \frac{1}{h_{crossover}}\right) \cong \frac{\ell^2_{mic}}{Ca}\frac{1}{h_{min}} \tag{4.12}$$

Substituting the value of h_{min} from equation 4.9 in equation 4.12, the length of the precursor film is:

$$L_p = \frac{\ell_{mic}}{Ca}\sqrt{\frac{2S}{3\sigma}} = \sqrt{\frac{2SA}{18\pi\sigma^2}\frac{1}{Ca}} \tag{4.13}$$

L_p is the length of the adiabatic precursor film only if there is no diffusive film present.

4.2.2 Diffusive precursor film

At longer times [68], the length of the precursor film becomes longer since the length is inverse proportional to the capillary number (or velocity of the spreading). At larger distances from the inflection point (crossover point),there exists a diffusive regime in which the velocity of the moving contact line becomes negligible. The part of the film close to the macroscopic drop (adiabatic part) ($x/x_{int} < 1$) would be governed by the relations derived in the previous section. However, the spreading of the precursor film farther from the length of the adiabatic precursor is governed by a non-linear diffusion relation. It was shown by Joanny & de Gennes [68] that

$$\frac{\partial h}{\partial t} = \frac{\partial}{\partial x}\left(\frac{A}{6\pi\mu h}\frac{\partial h}{\partial x}\right) \tag{4.14}$$

It was also indicated that the thickness of a diffusive film has a functionality of $h(x) \sim 1/x^2$ whereas for the adiabatic film it is $h(x) \sim 1/x$ (see equation 4.11).

The thickness of the crossover point, h_{int}, between these regions was found to be:

$$h_{int} = \frac{\sigma \ell_{mic}^2}{\dot{R}^2 \mu}\frac{1}{t} \tag{4.15}$$

where $\dot{R}$ is the average velocity of the spreading drop and t is time.

It is important to note that the value of h_{int} has to be between the minimum thickness h_{min} and the macroscopic thickness of the drop at the inflection point. If $h_{int} < h_{min}$ then the whole film is adiabatic and it is only governed by the adiabatic relations.

It is very important for this analysis for both adiabatic and diffusive precursor films, that fluid wets the surface completely. Another condition suggested by de Gennes [30] is the dynamic contact angle has to be very small:

$$\theta_a \ll \frac{2S}{\sigma} \tag{4.16}$$

To summarize, at the early stages of spreading of a perfectly wetting fluid with small dynamic contact angle, an adiabatic precursor film exists that spreads in front of the wetting line. The length of this film is inversely proportional to capillary number. However at the later stages of spreading, a diffusive film is generated at the end of the adiabatic film with smaller thickness. The length of this film is found to be $L_d = \ell_{mic}\sqrt{(2\sigma/\mu h)t}$ [68].

4.3 Experimental results and discussions

Most of the experiments previously performed to quantify precursor films have not been able to simultaneously confirm the existence of the macroscopic and microscopic descriptions of the spreading process and quantitatively interconnect the two processes. We have measured the length of precursor films using a novel interference microscope (psLFI) with both high temporal and spatial dynamic range (chapter 2). We have used the same experimental geometry as explained in chapter 3 and consider well-characterized silicone oils spreading on polished silicon wafers. First, we deposit a drop of silicone oil of a known volume on a cleaned silicon wafer using a syringe pump (Harvard Apparatus, pump 11). When the advancing contact line of the spontaneously wetting drop moves below the focal point of the objective lens its instantaneous rate of spreading, $\dot{R}$, is measured using a CCD camera and the profile, $h(t)$, is measured interferometrically. Knowing the local speed of the wetting line, the profile of the drop, $h(t)$, is converted to $h(x)$ via a simple Gallilean transformation ($x = \dot{R}t$).

The spreading velocity $\dot{R}(t)$ of the drop is a time-varying function that depends on the drop size and the dominant driving and resisting forces. The drops used in the present experiments have a volume $V = 10\mu\text{L}$ and initially assume the shape of a spherical cap (which spreads such that $R \sim t^{1/10}$) but ultimately evolve to a pancake regime ($R \sim t^{1/7}$). All of our measurements are performed when the drops are in the final pancake regime as noted in section 3.3.

To quantify the precursor lengths for a wide range of capillary numbers, a number of different silicone fluids have been used in our experiments . These materials are supplied by Gelest Inc. and they are same as those that were used in experiments in chapter 3. The rheological properties are tabulated in appendix A.

A representative drop profile is presented in figure 4-3. Here the abscissa represents the lateral displacement (x) of the front and the left ordinate shows the measured value of the decrease in optical path length (or local thickness of the drop, $h(x)$) in μm. To convert the measured phase to drop height, we used $n = 1.44$ for the

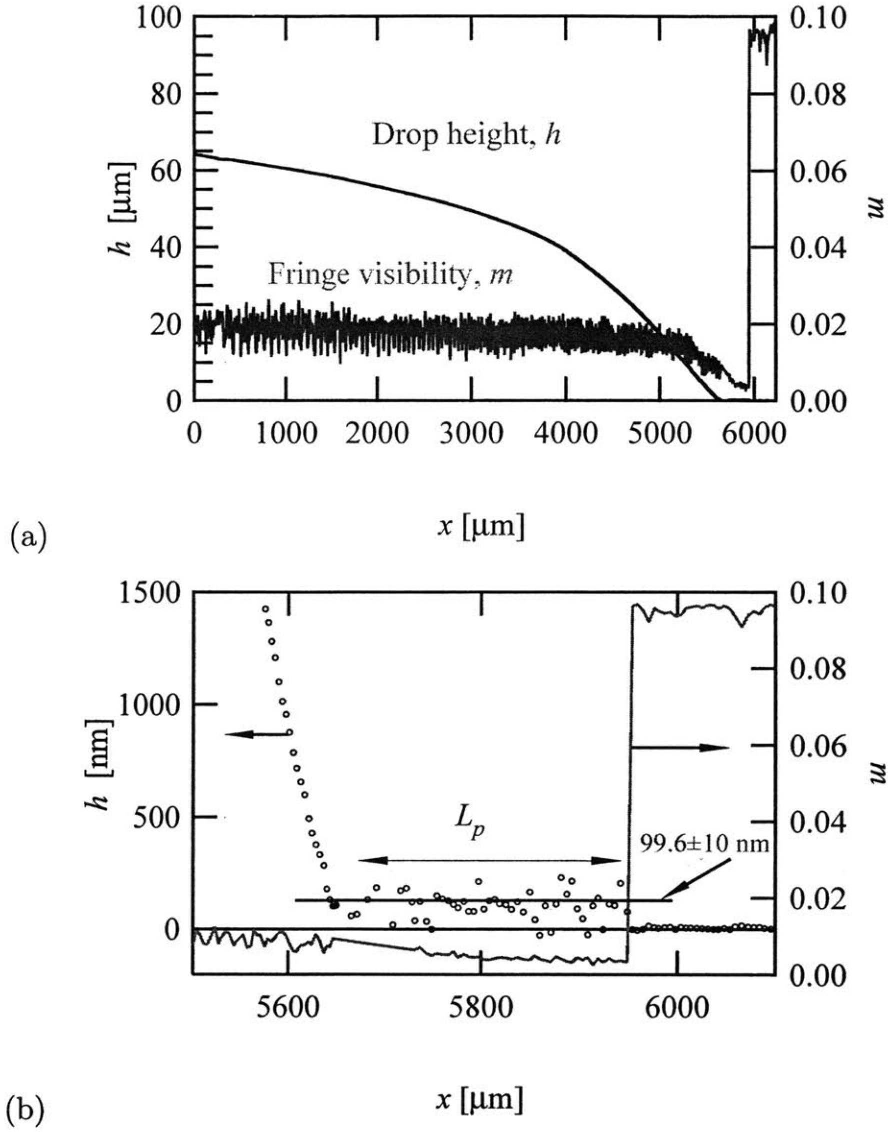

Figure 4-3: (a)Evolution in the profile of a silicone oil drop spreading on a smooth dry silicon substrate at $Ca = 2 \times 10^6$. Symbols (○) show the local thickness of the drop (in μm) and solid line is the visibility of the interference fringes, m. (b)An enlarged view of the precursor film detected in front of the moving contact line.

index of refraction of the liquid. The solid line represents the interferometric fringe visibility, m, and is represented on the right ordinate axis. The fringe visibility, m, remains constant until the edge of the precursor film reaches the focal point of the laser interferometer. At this instant, the fringe visibility decreases rapidly, well in advance of the macroscopic front reaching the measurement point. Figure 4-3(b) shows that a thin liquid precursor film or tongue of fluctuating but approximately constant thickness $H_P = 99 \pm 10$ nm preceding the macroscopic contact line is the cause of the drop in the fringe visibility. As noted before, $H_P \sim 1/x$ from equation 4.11. This decrease in fringe visibility is the interferometric equivalent of the impeded condensation of humid air that can be observed using a breath test[49]. Later in the spreading process, the macroscopic front passes through the measuring volume and the macroscopic profile of the drop can be accurately imaged.

We have determined the length of the adiabatic precursor film, L_P, for the spontaneously spreading liquid drops for a wide range of capillary numbers. It is important to note that the diffusive precursor films which usually develop at longer times (when $h_{int} > h_{min}$) are not part of this analysis. We define L_P as the distance from the point that the fringe visibility, m, suddenly decreases from the constant value corresponding to the bare silicon wafer surface to the point that the macroscopic profile is measured (figure 4-3(b)). In figure 4-4(a), we show the length of the precursor film L_P, as a function of capillary number, Ca. The length of the precursor film decreases monotonically as the spreading rate of the drop or fluid viscosity increases. Regression to a power-law relationship yields a best fit, $L_P = 7.2 \times 10^{-10} Ca^{-0.98 \pm 0.16}$ with L_P in meters. This result is in excellent agreement with the form of the theoretical prediction ([30, 68]) in equation 4.13. Furthermore, the front factor is in good agreement with the calculated value of $\sqrt{SA/6\pi\sigma^2} = 6.1 \times 10^{-10}$m which is shown by the dashed line in figure 4-4(a) ($S = 20 \times 10^{-3}$ Pa s; $\sigma = 20 \times 10^{-3}$ Pa s; $A = 1.4 \times 10^{-19}$ [56, 2]). In figure 4-4(b), we show the average thickness of the adiabatic precursor film, H_P in nm, as a function of capillary number. As can be seen from figure 4-3, significant local fluctuations in this local measurement of the precursor film can be measured using the psLFI technique; however there is no evidence of a dependency of the average thickness H_P on capillary number and a constant average thickness of 98 ± 20nm is measured.

These results are significant since most of the experiments done before to quantify the precursor films focused exclusively on the diffusive part of the film. Among all of these results only one [7] has documented a relation between L_P and the spreading velocity however the results do not span a wide range of capillary number and it is difficult to separately asses the effects of viscosity and surface tension.

Another important note is that the precursor films measured in our experiments are adiabatic precursor films. The calculated thickness between adiabatic and diffusive films (h_{int}) from equation 4.15 is always smaller that minimum possible thickness of drop (h_{min}) from equation 4.9 in our experiments. Therefore according to Joanny & de Gennes [68], the measured precursor films are adiabatic precursors.

To summarize, we have applied a non-invasive phase-shifting laser feedback interference microscope to investigate the evolution of the precursor films ahead of moving contact lines in dry spreading of perfectly wetting van der Waals fluids. The system has sufficient resolution and dynamic range to resolve details of both the physics of the inner (microscopic) interfacial region and its interconnection to the outer (macroscopic) fluid response. The theoretical predictions of different regimes of precursor films (adiabatic and diffusive) have been reviewed. We have shown that the length of the adiabatic precursor film, L_P, that forms in advance of the drop during the early stages of spreading is inversely proportional to the capillary number as anticipated theoretically [68, 30]. The front factor of this function is in good agreement with the theoretical prediction calculated by using the independently determined fluid properties. Even though we were not able to characterize the thickness of this layer (H_P) as a function of dynamic parameters of spreading, the average film thickness was shown to be approximately 100 nm for most of the measured precursor films over the range of capillary number ($10^{-6} < Ca < 10^{-3}$).

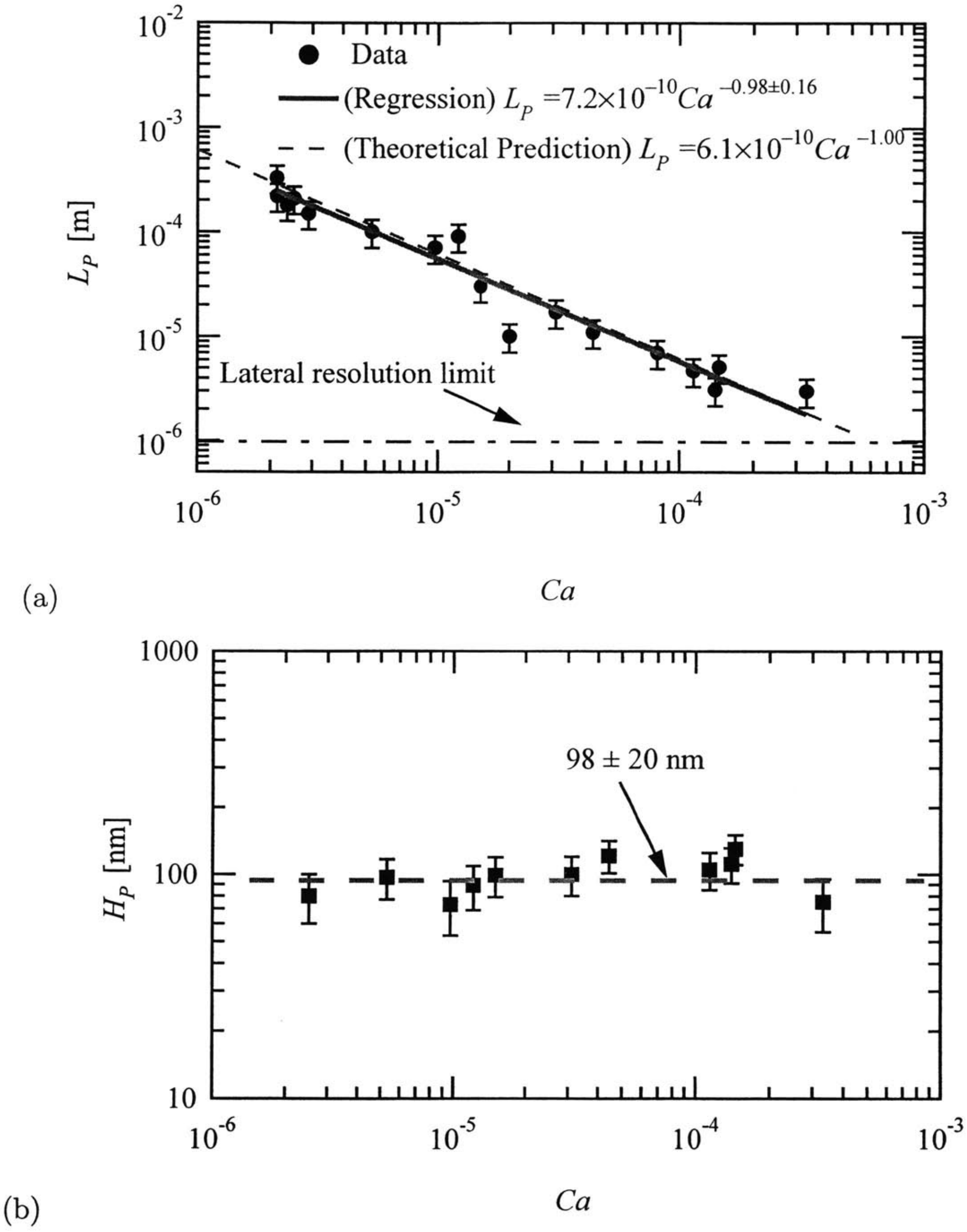

Figure 4-4: (a) Length of the precursor film, L_P, (in meters) as a function of capillary number. Solid line is the regression to the experimental results (●), $L_P = 7.2 \times 10^{-10} Ca^{-0.98\pm0.16}$, and dashed line is the theoretical prediction for an adiabatic precursor layer, $L_P = 6.1 \times 10^{-10} Ca^{-1}$. The dash-dot line is the diffraction limited lateral resolution of our system. (b) The average thickness of the precursor film, H_P, as a function of capillary number, Ca.

Chapter 5

Liquid drops spreading on inclined plates

5.1 Introduction

In the previous chapters, the analysis and the experimental results for the spreading of the viscous drops on *horizontal* surfaces have been presented. In all of these experiments, the effect of gravitational body forces were negligible ($Bo \equiv \rho g h^2/\sigma \ll 1$) unless explicitly mentioned (gravity currents). The dynamic contact angle measurements (HVT law) and microscopic characteristics of the spreading drop were all performed when gravitational effects were negligible, except in providing a hydrostatic pressure in the center of the large drop.

Another class of spreading drop problems which has been of interest to scientists through the last 50 years, is the spreading of a drop (or liquid film) on an inclined plate. This problem has been considered in the literature via several different approaches. The subject of most of the published works on the gravity driven drainage of films are on the fingering instabilities at the moving contact line (e.g. [64, 104, 9]). The mechanism for these instabilities involves a region of fluid far from the front line where the surface tension is not important [64] and a region close to the contact line where the surface tension dominates. Huppert [64] characterized this flow and concluded that the effect of surface tension is of a secondary nature.

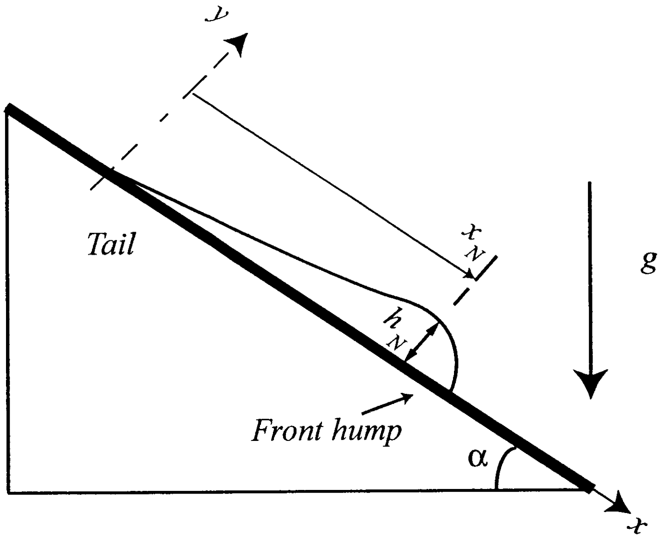

Figure 5-1: The schematic of a viscous drop spreading on an inclined plate. h_N is the maximum thickness of the drop and x_N is the location of the moving contact line. α is the slope of the inclined surface.

In recent years, theories were developed for spreading of a drop on inclined plate to derive a base solution for the instabilities. Huppert, as a pioneer in this type of experiments and analysis, showed that most of the energy will dissipate at the tail of the spreading drop (figure 5-1) by the viscous force. He assumed that for this reason one can neglect the effect of the surface tension in the spreading process. In his analysis, he totally neglected the effect of the front hump (from the location of the maximum thickness, h_N, to the tip of the drop). We will discuss this further in section 5.2. Later, Troian et al. [111] improved Huppert's analysis by adding the first order effects of surface tension into lubrication analysis of the base state flow. They went on to develop a stability analysis of the two-dimensional lubrication equations for very small contact angles.

The analysis of the spreading of liquid films on an inclined plate without the above mentioned instabilities are done partly by Goodwin & Homsy [48]. A boundary integral technique was used to obtain the numerical solution to the problem in which a contact angle boundary condition as a fixed value was imposed as shown in figure 5-2. Numerical simulation of this type of flow was also performed by Reznik & Yarin

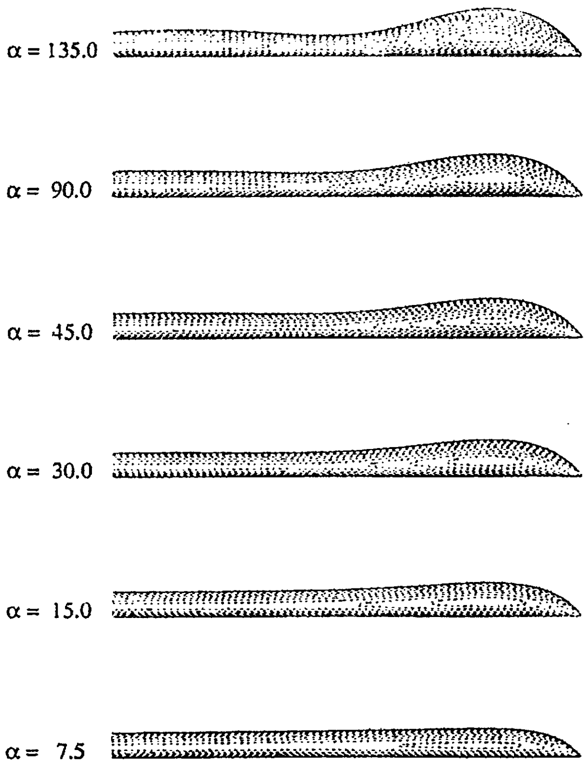

Figure 5-2: Streamfunction contours over a range of inclination angles α with the capillary number and contact angle held fixed at $Ca = 0.10$ and $\theta = 45°$ from [48].

[97]. In most of these numerical simulations, the dynamic contact angle and capillary number were inputs of the simulations. Thus, it is very difficult to compare these results with the experimental data since the observed contact angle depends on the capillary number in the spreading process (figure 3-9). One of the main conclusions by Goodwin & Homsy [48] and Hocking [57] is that for larger capillary numbers at which the dynamic contact angle becomes large, the lubrication analysis breaks down and other approaches, such as the Stokes flow problem, are needed to analyze this problem [48].

In this chapter, we investigate the steady flow of a viscous drop on an inclined plane before the onset of these instabilities. We made sure that no instability existed during our experiments (due to the small size of drop). Our high resolution optical system (psLFI microscope) was used to investigate the macroscopic and microscopic features of this regime of spreading.

5.2 Theoretical analysis

Detailed analysis of a spreading viscous drop on an inclined plate can be found in previous studies (e.g. [64, 48, 9]; also [90] on powerlaw fluids). In this section, a similar scaling analysis is used to derive a relation for the characteristics of the drop as a function of time.

First, we used lubrication analysis to derive the governing equation of spreading of a viscous drop on an inclined plate as :

$$3\mu U = -h^2 \frac{dP}{dx} + \rho g \sin(\alpha) h^2 \tag{5.1}$$

where α is the angle of inclination of the plate, P is the pressure, U is the average velocity of the leading front, and h is the thickness of drop. From the pressure balance at the free surface, pressure can be calculated as $P = -\sigma(d^2h/dx^2)$. Equation 5.1 can be written as:

$$3\mu U = -\sigma h^2 \frac{d^3h}{dx^3} - \rho g \sin(\alpha) h^2 \tag{5.2}$$

We can rewrite equation 5.2 in dimensionless form using $h^* = h/h_N$ and $x^* = x/x_0$, where h_N is the thickness of the front and x_0 is a lateral length scale, as:

$$3Ca = -\frac{h_N^3}{x_0^3} h^{*2} \frac{d^3 h^*}{dx^{*3}} - Bo\, h^{*2} \tag{5.3}$$

where $Bo = \rho g \sin(\alpha) h_N^2/\sigma$ and $Ca = \mu U/\sigma$ are Bond number and capillary number, respectively.

Let's choose $x_0 = h_N/(3Ca)^{1/3}$ similar to what we chose for lateral length scale in section 3.3.2. Equation 5.3 can be written as:

$$-1 = h^{*2} \frac{d^3 h^*}{dx^{*3}} + \frac{Bo}{3Ca} h^{*2} \tag{5.4}$$

If $Bo \ll Ca$ (e.g. $\alpha \approx 0$), then equation 5.4 would have the form of equation 3.29 and drop spreads similar to spreading on a horizontal plate. The dynamic contact angle of the advancing drop front, θ_a, is scaled with the thickness of the drop and the distance of the maximum thickness from the front, x_0, as $\theta_a \sim h_N/x_0$. Using the scaling for x_0, the dynamic contact angle as a function of capillary number is found to be $\theta_a \sim Ca^{1/3}$. This scaling is similar to the HVT law for the spreading liquid drops on inclined plane when $Bo < Ca$.

If $Bo \gg Ca$, the left hand side of equation 5.2 is negligible and after simplification and integration in respect to x, it can be written as:

$$\frac{h_N^2}{x_0^2} \frac{1}{Bo} \frac{d^2 h^*}{dx^{*2}} + 1 = 0 \tag{5.5}$$

If we choose $x_0 = h_N/Bo^{1/2}$, equation 5.5 is found to be:

$$\frac{d^2 h^*}{dx^{*2}} + 1 = 0 \tag{5.6}$$

The dynamic contact angle of the advancing drop front, θ_a, when $Bo \gg Ca$ is found to be:

$$\theta_a \sim \frac{h_N}{x_0} \sim Bo^{1/2} \tag{5.7}$$

An interesting feature of drop spreading on an inclined plate, when both the gravitational body forces and viscous force are important and capillarity effect is negligible in equation 5.2, is the following:

$$Bo \equiv \frac{\rho g \sin \alpha h_N^2}{\sigma} = Ca \tag{5.8}$$

As seen in equation 5.8, in this type of spreading the Bond number and capillary number are equivalent. This is a very unique feature that is not obvious at the beginning of analysis.

In the next section, the experimental results that were performed to confirm these scaling analysis will be presented.

5.3 Experimental results

We have used the same experimental setup as one used for spreading on a horizontal surface, as explained in detail in chapters 4 and 5. Since the laser beam in the psLFI microscope has to be perpendicular to the substrate, psLFI system and the substrate were mounted on a rigid breadboard. Then the breadboard was tilted to the desired inclination angle, α, and held firmly by a jack (figure 5-3).

The fluids used in these experiments are silicone fluids (Gelest Inc.) same as those used in the previous chapters. The fluid properties are presented in appendix A. The experiment procedure is also similar to the previous cases. A drop of silicon oil is deposited on a clean silicon wafer using a syringe pump (Harvard Apparatus, pump 11). While the drop moves down the inclined plate, its free surface profile is measured by the psLFI system as a function of time. The velocity of this drop is measured from the side by a CCD camera to convert the observation time to the spatial coordinate, $x = U(t - t_0)$). The dynamic contact angle is calculated by numerical differentiation of the free surface profile (same as chapter 3). We carefully observed the fringe visibility, m, to be able to detect a possible precursor film in front of the moving contact line as we did in chapter 4.

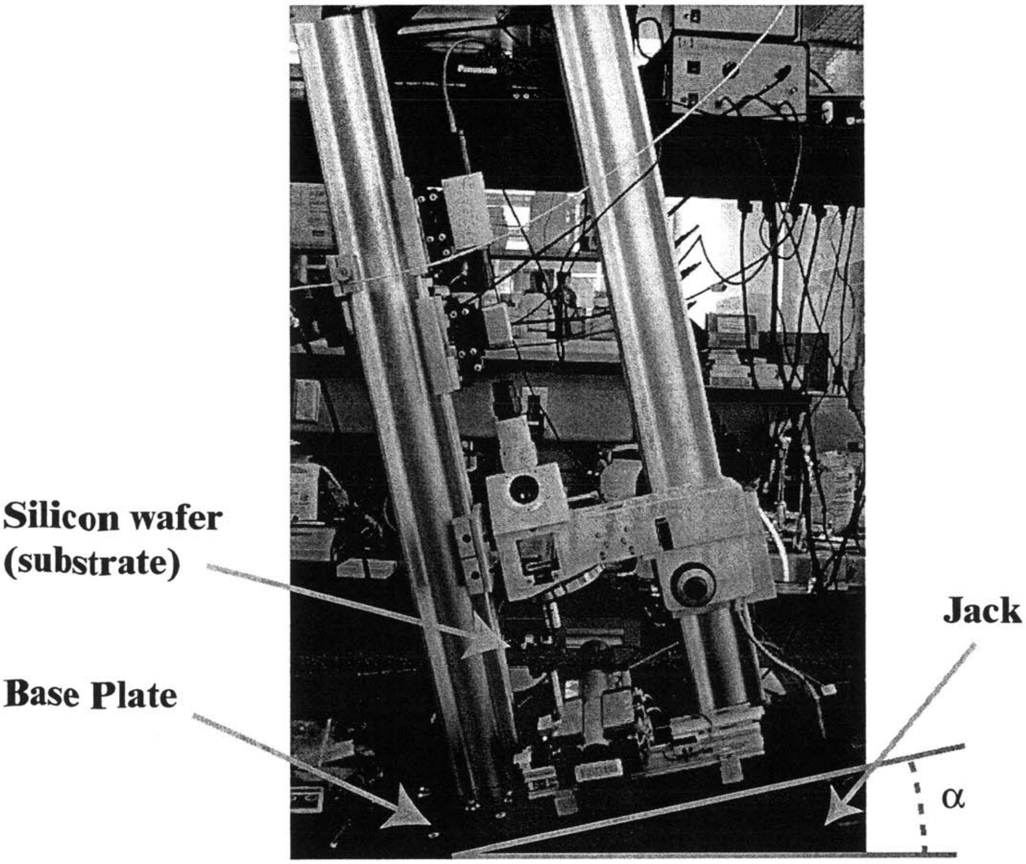

Figure 5-3: Tilted psLFI system for measurement of spreading drop on inclined plate.

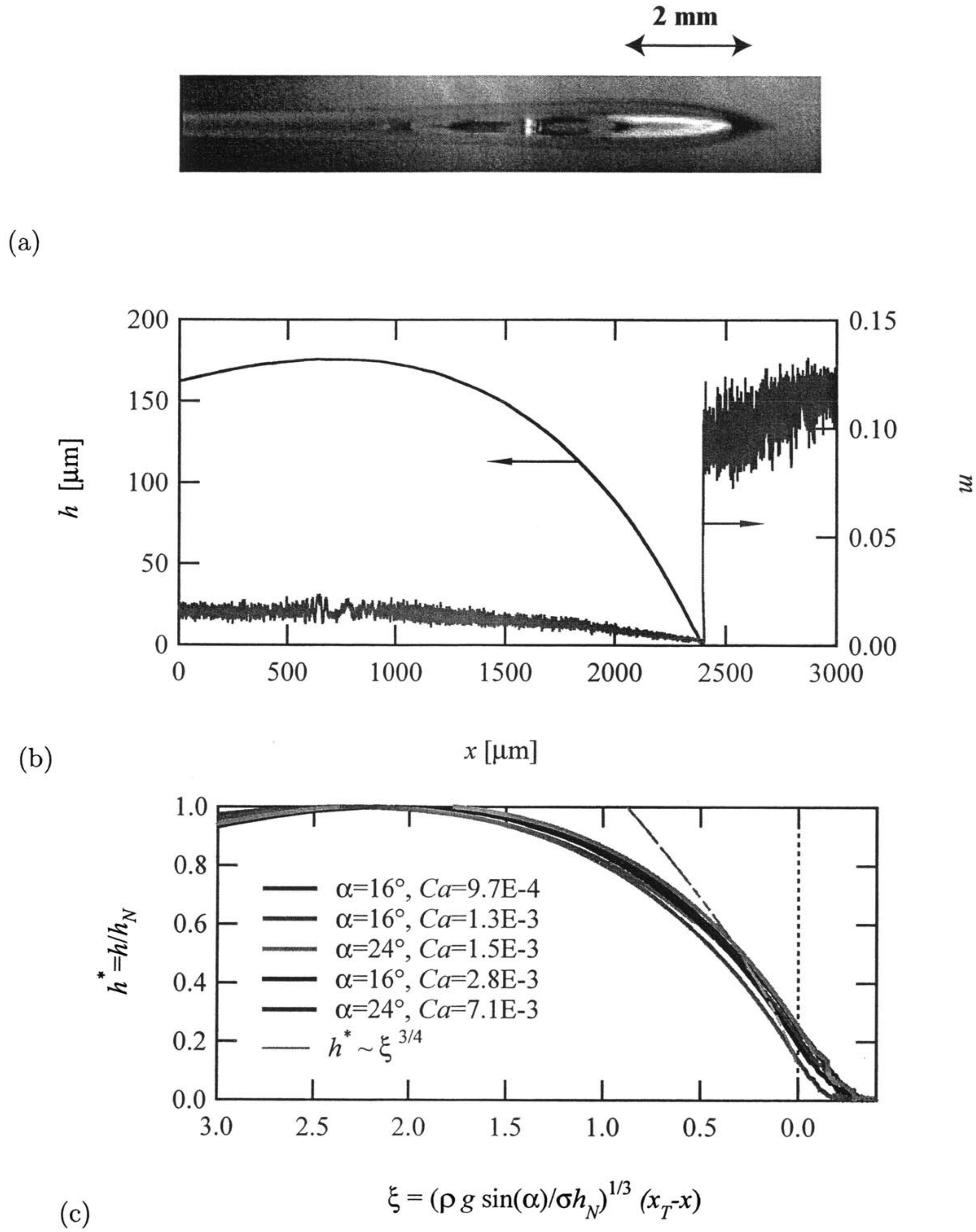
(a)

(b)

(c)

Figure 5-4: (a) A photograph and (b) profile of spreading drop on an inclined plate, $Ca = 7.1 \times 10^{-3}$, $\alpha = 24°$. (c) The profiles of the spreading viscous drops in dimensionless forms using equation 5.10. The dashed line is the similarity solution fitted to the experimental data. The reference for ξ is chosen at the inflection point of the profiles. x_T is the location of the inflection point.

5.3.1 Profiles of drops moving down the inclined plate

Figure 5-4 shows the profiles of drops spreading on a silicon wafer when it is tilted with an inclination angle, α. Figure 5-4(a) shows a picture of a drop spreading on an inclined plate which free surface profile was measured using psLFI microscope and shown in 5-4(b) ($Ca = 7.1 \times 10^{-3}$, $\alpha = 24°$). The left vertical axis of this plot is the measured thickness, h, of the moving drop in μm and the right vertical axis is the fringe visibility, m, from the psLFi system. The horizontal axis of the plot is the lateral displacement, x in μm. The maximum thickness of the drop is h_N.

To make the profiles dimensionless , the following scaling forms are used:

$$h^* = \frac{h}{h_N} \tag{5.9}$$

$$\xi = \left(\frac{\rho g \sin(\alpha)}{\sigma h_N}\right)^{1/3} (x_T - x) = Bo^{1/3}\,\frac{x_T - x}{h_N} \tag{5.10}$$

where x_T is the location of the inflection point and ξ is the distance from the moving contact line into the drop. The resulting dimensionless profiles, for several drops with different Ca and inclination angle α, are shown with solid lines in figure 5-4(c). As seen in this figure, the profiles close to the contact line are self-similar as predicted by Huppert [64]. The scaling for the self-similar profile close to the contact line is:

$$h^* + h_i^* \approx \left(\frac{64}{15}\right)^{1/4} \xi^{3/4} \tag{5.11}$$

The self -similar profile is shown on the figure 5-4(c) with a dashed line. The vertical axis of this plot is the dimensionless thickness h^* and the horizontal axis is the dimensionless lateral displacement ξ. The dimensionless thickness of the drop at inflection point is h_i^*. The reference for ξ is taken at the inflection point to unify the starting point for all of the profiles.

As shown in this figure, the similarity solution is not valid for $\xi = 0$ since it predicts $\theta_a = \pi/2$ for all the drops regardless of the capillary number. We will show the results for the dynamic contact angle in the next section which varies with capillary number.

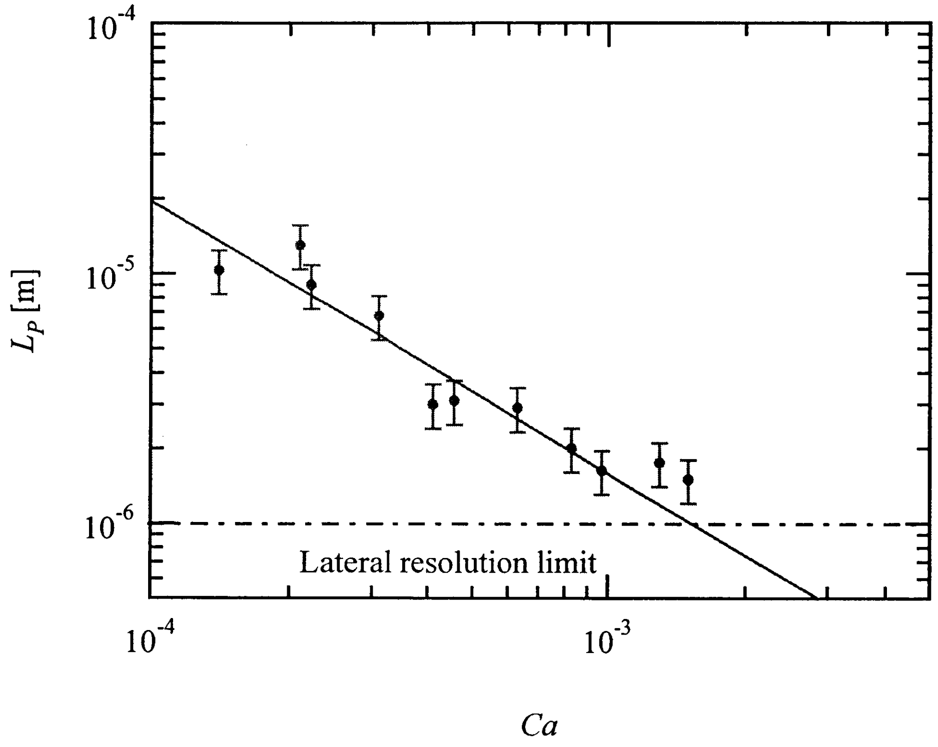

Figure 5-5: Length of the precursor film L_P as a function of capillary number Ca for the spreading drops on inclined plate. The power-law regression gives $L_P = 8.4 \times 10^{-10} Ca^{-1.09 \pm 0.01}$

5.3.2 Characteristics of the moving contact line

For drops with $Ca < 2 \times 10^{-3}$, a thin liquid film (precursor film) was detected which moves in front of the contact line. The analysis of these film has been addressed in chapter 4. As shown in chapter 4, the length of the 'adiabatic' precursor film, L_P is inversely proportional to the capillary number (equation 4.13). The measured length of the precursor film as a function of capillary number is presented in figure 5-5. The vertical axis of the graph is the length of the precursor film L_P and the horizontal axis is the capillary number. Similar to our observation in chapter 4, a power-law regression to the experimental data gives $L_P = 8.4 \times 10^{-10} Ca^{-1.01 \pm 0.01}$ with L_P in meters. This result is in good agreement with the results of the chapter 4 and the theoretical prediction. However, the front factor of the regression is lower than the front factor for horizontal spreading. We were not able to detect any precursor films for capillary numbers higher than 1.5×10^{-3} since the length of the precursor films become on the order of the lateral resolution of psLFI.

Represented drop profiles for two different capillary numbers and inclination angles, α, are shown in figure 5-6. The dynamic contact angle of the drop with higher capillary number, shown in figure 5-6(a) ($Ca = 2 \times 10^{-2}$ spreading on an inclined plate, $\alpha = 24°$), is larger than dynamic contact angle of drop with a lower capillary number, figure 5-6(b) ($Ca = 3.8 \times 10^{-4}$ which spread on an inclined plate, $\alpha = 7°$).

In figure 5-7 the measured dynamic contact angle θ_a (chapter 3) is plotted as a function of capillary number. For smaller values of Ca, the dynamic contact angle follows the well known HVT law (cf. chapter 3). The power law regression to this data set gives $\theta_a = k_1 Ca^n$ where $k_1 = 3.3 \pm 0.06$ and $n = 0.38 \pm 0.02$ with a confidence level of $R^2 = 0.966$. However for $Ca > 10^{-2}$, the dynamic contact angle θ_a increases more rapidly compared to those for smaller capillary numbers. A power-law regression to this part of data gives $\theta_a = k_1 Ca^n$ where $k_1 = 5.03 \pm 0.4$ and $n = 0.45 \pm 0.02$ with a confidence level of $R^2 = 0.950$. We are not aware of any prior experimental work that has reported this behavior for the dynamic contact angle for spreading viscous drops on an inclined plate. In previous section, we argued that if $Bo > Ca$ then

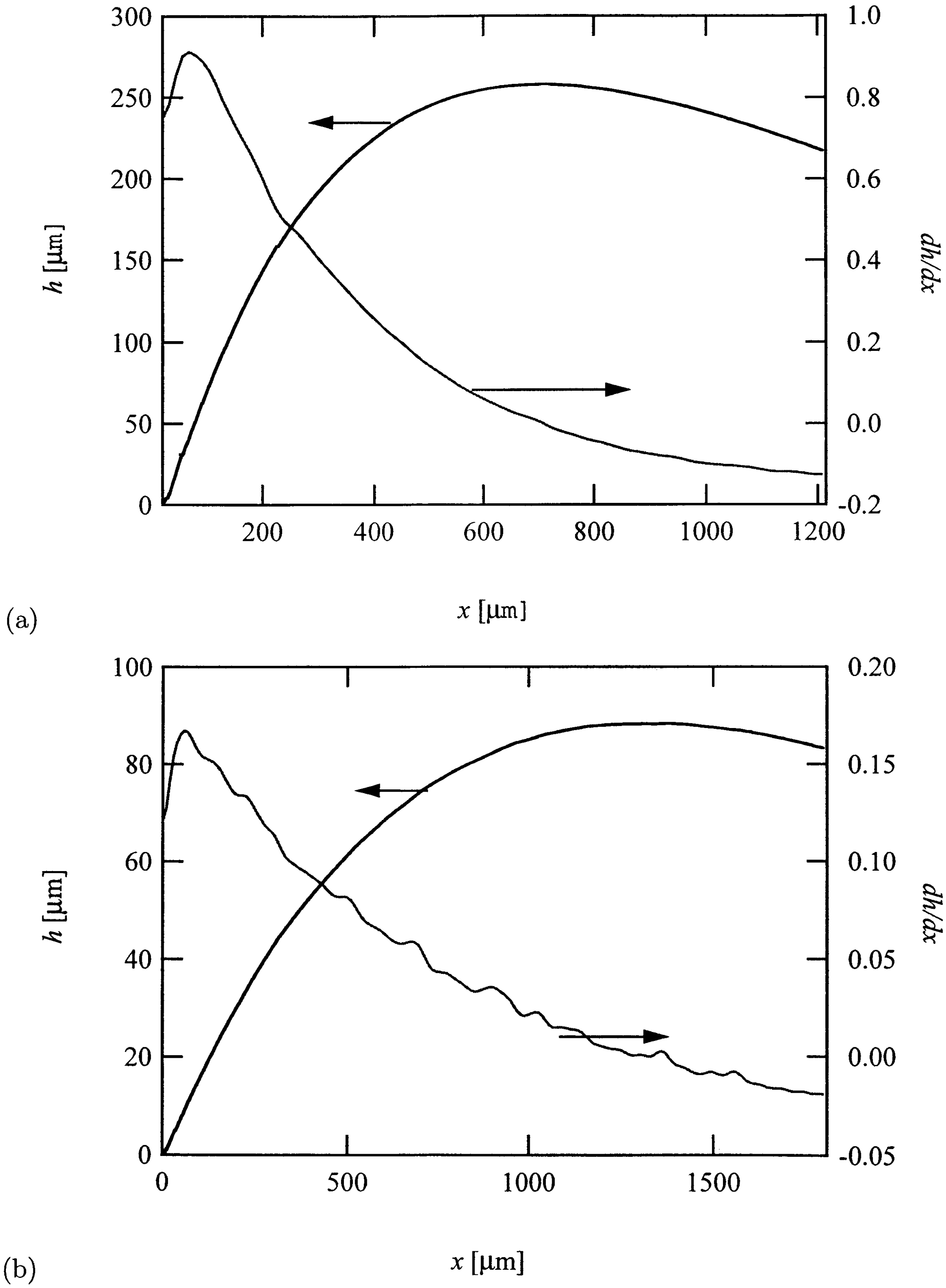

Figure 5-6: Drop profile, $h(x)$, and spatial derivative, dh/dx, for two different values of capillary number: (a) $Ca = 2 \times 10^{-2}$, $\alpha = 24°$; (b) $Ca = 3.8 \times 10^{-4}$, $\alpha = 7°$.

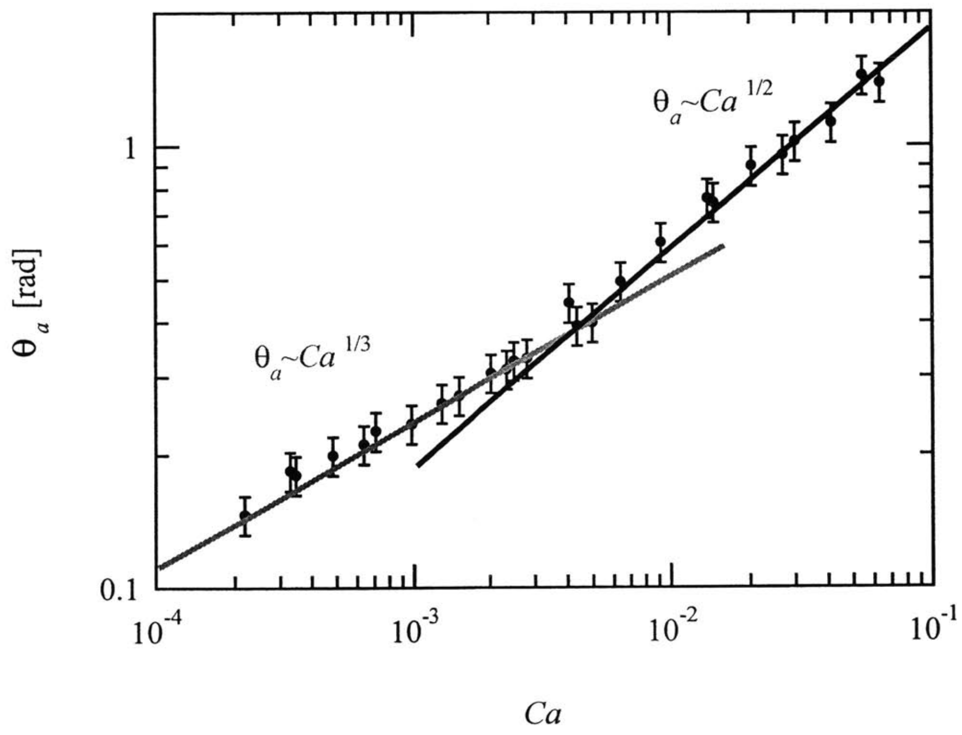

Figure 5-7: The dynamic contact angle of spreading drop of an inclined plate as a function of capillary number.

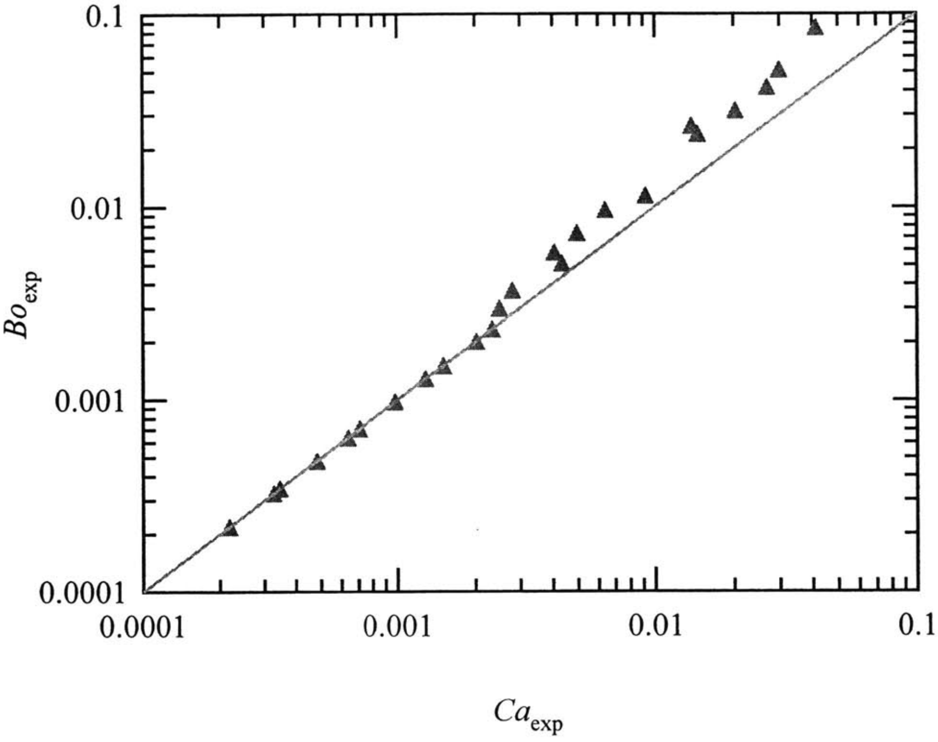

Figure 5-8: Experimentally measured Bond number $Bo_{exp} = \rho g \sin \alpha h_N^2/\sigma$ as a function of measured capillary number $Ca_{exp} = \mu \dot{x}/\sigma$. The solid line is $Bo_{exp} \sim Ca_{exp}$.

the dynamic contact angle would scale as equation 5.7. This can be the reason for the change in exponent of the power-law in figure 5-7. To further investigate this matter, we plotted $Bo_{exp} = \rho g \sin \alpha h_N^2/\sigma$ as a function of measured capillary number $Ca_{exp} = \mu \dot{x}/\sigma$ in figure 5-8. In figure 5-7, Ca is measured capillary number, Ca_{exp}. Since Bond number and capillary number are equivalent earlier in this process as shown in lubrication analysis, the value of Bond number increases as capillary number increases with a power-law exponent of unity. The lubrication analysis is only valid for small angles and $B0 \ll 1$. Therefore for higher Bond numbers, a deviation from the HVT law can happen. It shown in figure 5-8 that for capillary numbers higher than 0.01, the values of the measured Bond numbers, Bo_{exp}, become larger than the corresponding capillarity numbers, Ca_{exp}. This deviation supports our argument for the change in power-law exponent from the HVT law.

5.4 Discussion

In this work, we have studied the slow spreading of perfectly wetting viscous drops on a silicon wafer with an angle of inclination, α, with the horizontal surface. The fingering instabilities that may happen in this process at long times have been widely investigated [64, 104, 9]. In this study, we are interested in the relationship between the advancing contact angle and rate of spreading of moving contact line in the absence of the instability.

Analytically, we have shown that capillary number,$Ca = \mu U/\sigma$ and Bond number $Bo = \rho g h_N^2 \sin(\alpha)/\sigma$ are equivalent for lower values of Ca when lubrication analysis is valid. The gravitational force is the main resource for the spreading in this process and the drop spreading velocity can be found by balancing the viscous force with the gravitational force.

The free surface of the drops with the range of viscosities (0.5 Pa s $< \mu <$ 10 Pa s) have been measured on plates with angle of inclination of $\alpha = 7°, 16°, 24°$. By using the proper scaling, we have shown that the all of the drop profiles close to the contact line fall on a master curve $h^* \sim \xi^{3/4}$. However, this can not accurately predict the contact angle since it gives a contact angle of $\pi/2$ at the wall and does not predict an inflection point. The existence of the inflection point is important because it is the location of the dynamic contact angle [79] and it is a crossover point to a microscopic region as we explained in detail in chapters 3 and 4. We have detected and quantified the precursor films present in front of the moving contact line and showed that they follow a similar power-law which was predicted by Joanny & de Gennes [68] and discussed in chapter 4.

Finally, the measured dynamic contact angle is presented as a function of capillary number. For smaller capillary number, the power-law fit to the experimental data has a good agreement with the HVT law. For $Ca > 0.01$ however, the dynamic contact angle systematically deviates from the HVT law and the new power-law has the form of $\theta \sim Ca^{1/2}$. We argue that when the dynamic contact angle is small, lubrication estimation is valid, thus the viscous force and gravitational body force are involved in spreading precess and this leads to the HVT law. However we have shown that for the high Bond numbers ($Bo > Ca$), the gravitational body force balances the capillarity and this lead to $\theta_a \sim Bo^{1/2}$.

Chapter 6

Evaporatively-driven Marangoni instabilities on spreading liquid films

6.1 Introduction

In the previous chapters, the macroscopic and microscopic features of the 'isothermal' spreading of viscous drops have been presented. The volume of the drop is assumed to stay constant during the spreading process. The temperature of the environment and the spreading fluid were constant. The silicon wafer is used in this process have a very high thermal diffusivity $9.34 \times 10^{-5} m^2/s$. Thus, we can assume that the temperature of the substrate is always constant and is equal to the environment temperature. The silicone liquid used in the steady spreading experiments are all have very high saturation temperature. This means the evaporation rate for these fluids are negligible.

It is also know that if the spreading is non-isothermal, new features may appear during the spreading process. One of most common features of non-isothermal films are a class of instabilities that are usually called *Marangoni* instabilities. Marangoni instability arises from the thermal or concentration variations (for mixtures) in the liquid film that result a gradient in the surface tension due to its dependence to temperature and concentration of the dissolved solutes.

The parameters involved in this type of instability is characterized by the Marangoni number, $\bar{Ma}$, which is defined as:

$$\bar{Ma} = -\frac{\partial \sigma}{\partial x}\frac{R^2}{\alpha \mu} = -\frac{\partial \sigma}{\partial T}\frac{\partial T}{\partial x}\frac{R^2}{\alpha \mu} \tag{6.1}$$

This definition is in terms of drop radius R, thermal diffusivity α, viscosity μ, and surface tension gradient $\partial \sigma / \partial x$. The critical Marangoni number value for a system showing Marangoni instability is usually $50 - 100$ [2].

Instability of liquid films is a branch of interfacial science that has attracted many scientists because of its mathematically and physically aspects since early 20th century. The phenomenon of cellular convection in a liquid with a free surface heated from below was first discovered by Bénard [8]. A fundamental theoretical paper is that of Lord Rayleigh [95], who considered instability due to the buoyancy resulting from expansion of a heated liquid. Later, Jefferys [66, 67] and Low [75]extended and refined Lord Rayleighs analysis. The agreement with experiments involving marginal stability has been generally good. In all these treatments the cause of instability was buoyancy. Pearson [92] argued that buoyancy was not the driving force and offered a new explanation for the instability. He showed that if the upper surface was free then Bénard type cells could be produced by tactions arising from the variation with temperature of surface tension. He argued that in many of Bénards experiments the cells observed must have been due to surface tension effect rather than buoyancy. Nield [82] combined these two theories and showed that the two effects reinforced one another and are tightly coupled. Scriven & Sternling [102, 103] extended Pearsons analysis to include a deformable interface and demonstrated that this added degree of freedom renders the system convectively unstable at all Marangoni numbers. Detailed reviews of this type of instabilities can be found in [27, 100]

During our experiments on spreading drops it was noticed that if a drop of volatile wetting liquid was deposited on a surface and allowed to spread, then, after a few seconds, periodic fluctuations at the free surface of the liquid film (figure 6-1) were

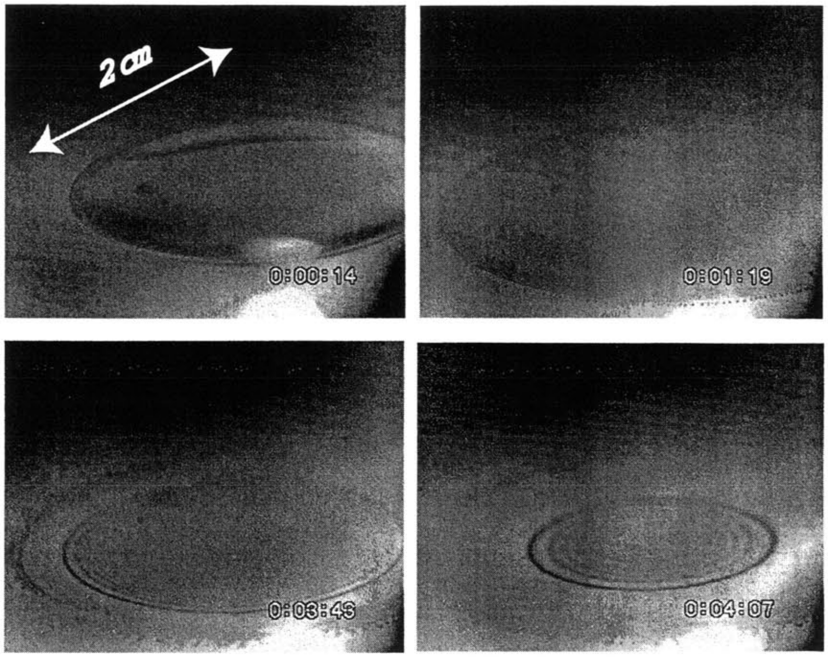

Figure 6-1: Snap shots of a volatile liquid drop during spreading on a conductive substrate.

detected by the confocal measuring system. A series of experiments described in this chapter show that these instabilities arise as a result of the volatility of the liquid and the non-uniform evaporation rate across the drop. Also a detailed linear stability analysis is presented using the lubrication analysis developed by Ehrhard & Davis [39] and Oron et al. [84]. The linear stability results is compared with the experimental result at the end of this chapter.

6.2 Experimental results

The latent heat of spreading and the latent heat of evaporation can both be important in such problems. However, our calculation shows the latent heat of spreading is negligible compared to the latent heat of evaporation. For example, using material properties (appendix A), the latent heat of spreading, $\Delta H = -\sigma + T\partial\sigma/\partial T$, can be calculated as $40mJ/m^2$. This means to change the temperature in drop of silicone oil by $1K$, the area of spreading has to be $2m^2$ [56]. A detailed thermal analysis [84] shows that the important dimensionless parameter in this type of evaporatively-driven instabilities is the dimensionless interfacial thermal resistance, $\mathcal{R}$. This dimensionless parameter $\mathcal{R}$ quantifies the relative magnitude of the evaporative resistance to heat transfer at the interface compared to the conductive resistance of the liquid film itself. It is analogous to the inverse of the Biot number encountered in convection-diffusion heat transfer problems, $Bi = h_{conv}/(k_s/h_0)$, in which h_{conv} is the heat transfer coefficient for convection into a liquid and k_s/h_0 is the heat transfer coefficient for thermal diffusion through the solid boundary. A linear stability analysis will be presented later in this chapter shows that for a critical $\mathcal{R}$ disturbances on the spreading film are amplified and for $\mathcal{R}$ smaller than this critical value, the liquid microdroplets spread without showing this type of evaporative instability. The limit $\mathcal{R} = 0$ is special and corresponds to the case of a perfectly thermally-insulating film or a non-volatile spreading fluid with zero mass flux from the surface. There are several thermophysical parameters of both the spreading fluid and the underlying substrate that affect the observed instability phenomenon. In the following sections, we explore each of these factors.

6.2.1 Effect of Liquid Viscosity

In 6-2 we show the evolution in the height of the spreading droplets close to onset of instability for (a) L ; $Oh = 0.003$, $\phi = 1.39$, (b) M; $Oh = 0.02$, $\phi = 1.35$, and (c) H; $Oh = 0.23$, $\phi = 1.33$. In each figure the ordinate axis is the local thickness of the drop in micrometers and the abscissa represents elapsed time in seconds. The solid lines show the power-law relation expected for the spreading in the absence of Marangoni instability.

For the liquid with the lowest viscosity (figure 6-2(a)) the instability starts at a film thickness of about 30μm. The insets to the figure show details of the periodic fluctuations in the free surface height of the drop. It can be seen that as the drop spreads and the film thickness decreases the relative amplitude of the oscillations increases and the frequency decreases. In figure 6-2(b) we show the onset of instability in the oil of intermediate viscosity (M). It can be seen that the instability threshold is achieved at a lower critical thickness than observed in the previous case. Also the amplitude of oscillations is smaller than observed in the low Oh case. The inset to figure 6-2(b) shows the same data plotted on double logarithmic axes. Initially, the film thickness has a power-law form as expected. As the disturbance grows there is a small but systematic deviation from the simple power-law spreading. In figure 6-2(c) we show the onset of instability in the more viscous fluid (H). The same trend can be seen here as the instability starts at a yet lower film thickness and the amplitude of the oscillations are smaller than those observed at lower Oh. Finally, in figure 6-2(d) we show the spreading profile observed in the most viscous fluid (V). No instability can be observed within the resolution of the measuring system down to the minimum detectable height of approximately 0.5μm.

6.2.2 Directionality of the Traveling Waves

The disturbances shown in figures 6-2(a)-(c) correspond to surface perturbations propagating past the fixed measuring point of the laser confocal microscope. To investigate the speed and direction of the surface waves generated by this evaporative Marangoni instability, the surface profile of a spreading droplet of low viscosity silicone oil (L) is measured by scanning the laser probe across the drop at a constant speed of $U = 320mm/s$. First the film surface is scanned from the contact line toward the center of the drop and then in the reverse direction from its center toward the contact line. The scanning results are shown in figure 6-3. The solid line shows the wave profile when the scanning direction is from the leading edge towards the center and the dashed line represents the wave pattern when the scanning direction is from the center to the contact line. It can be seen in this figure that the waves have a higher apparent frequency when the scanning direction is from the center outwards towards the contact line. This Doppler shifting in the disturbance frequency indicates that the surface waves resulting from the evaporatively-driven Marangoni instability propagate radially-inwards from the contact line to the center of the drop.

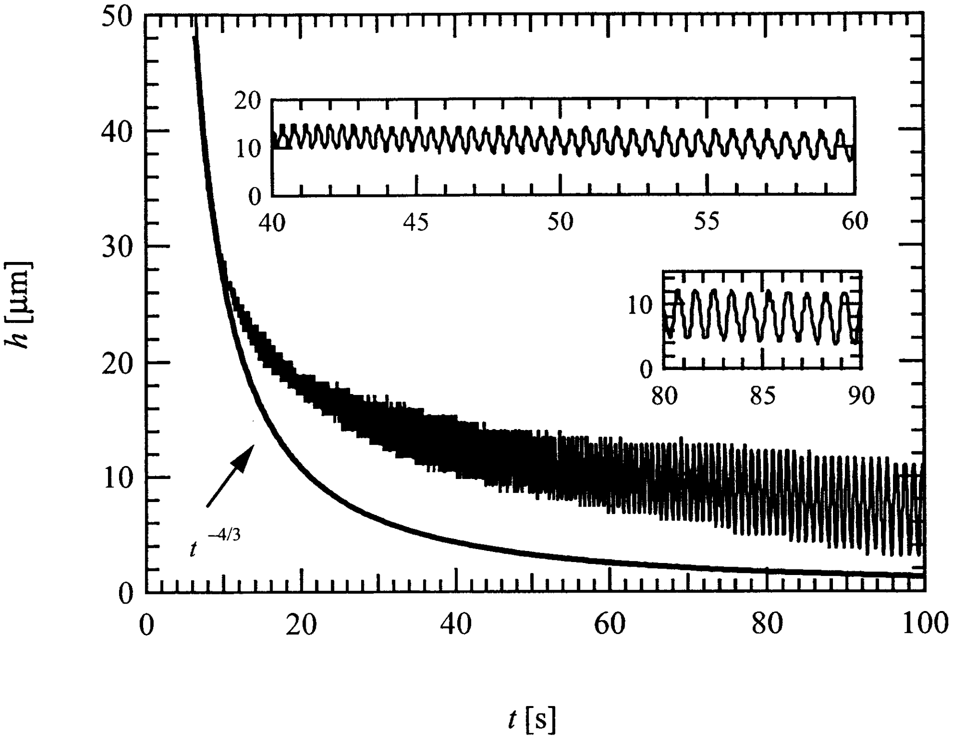
50
40
30
20
10
0
h [µm]
0
20
40
60
80
100
t [s]
$t^{-4/3}$
20
10
0
40
45
50
55
60
10
0
80
85
90

(a)

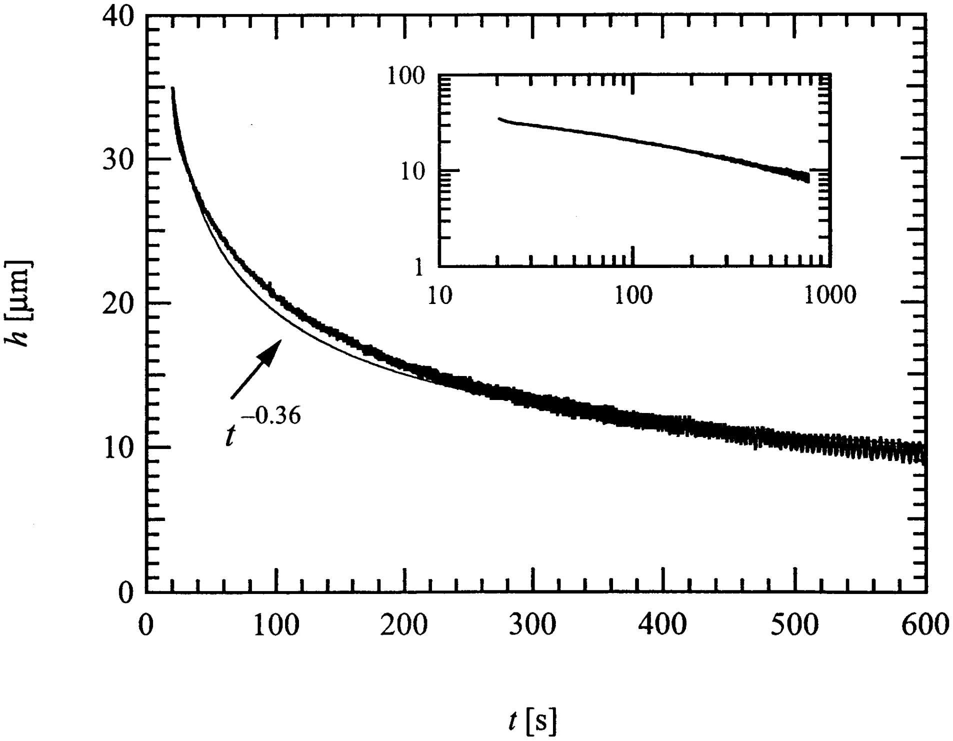
40
30
20
10
0
h [µm]
0
100
200
300
400
500
600
t [s]
$t^{-0.36}$
100
10
1
10
100
1000

(b)

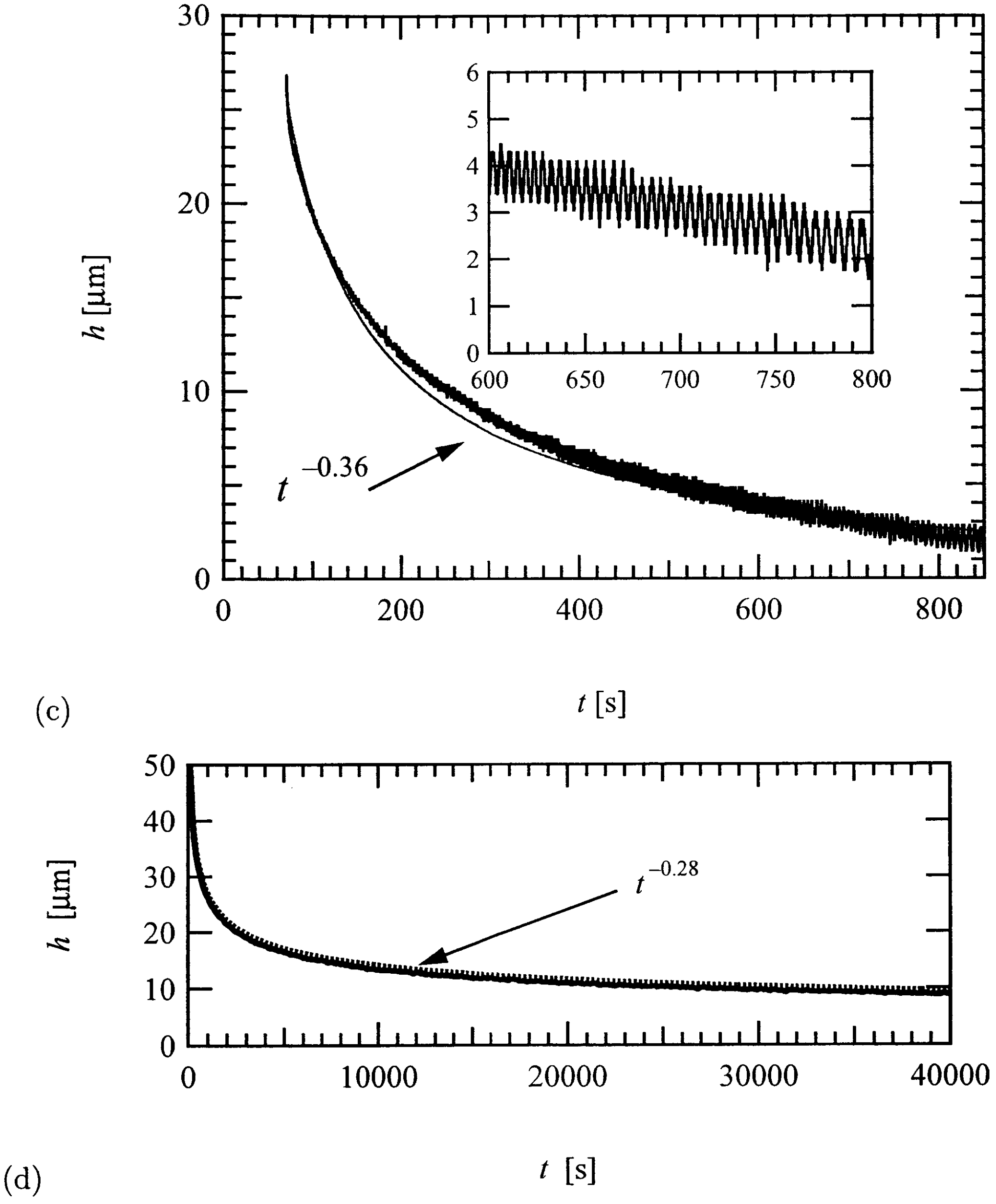

Figure 6-2: Onset of instability for fluids of low, medium and high viscosity (a)L, (Oh = 0.003, ϕ = 1.39); (b) M. (Oh = 0.02,ϕ = 1.35); and (c) H, (Oh = 0.23, ϕ = 1.33). The solid lines show the power-law relation expected for the spreading in the absence of instability. (d) Spreading profile for fluid V, (Oh = 62.9, ϕ = 1.31). No instability can be observed within the resolution of the measuring system. Dotted line is the expected power-law relation expected from the analysis.

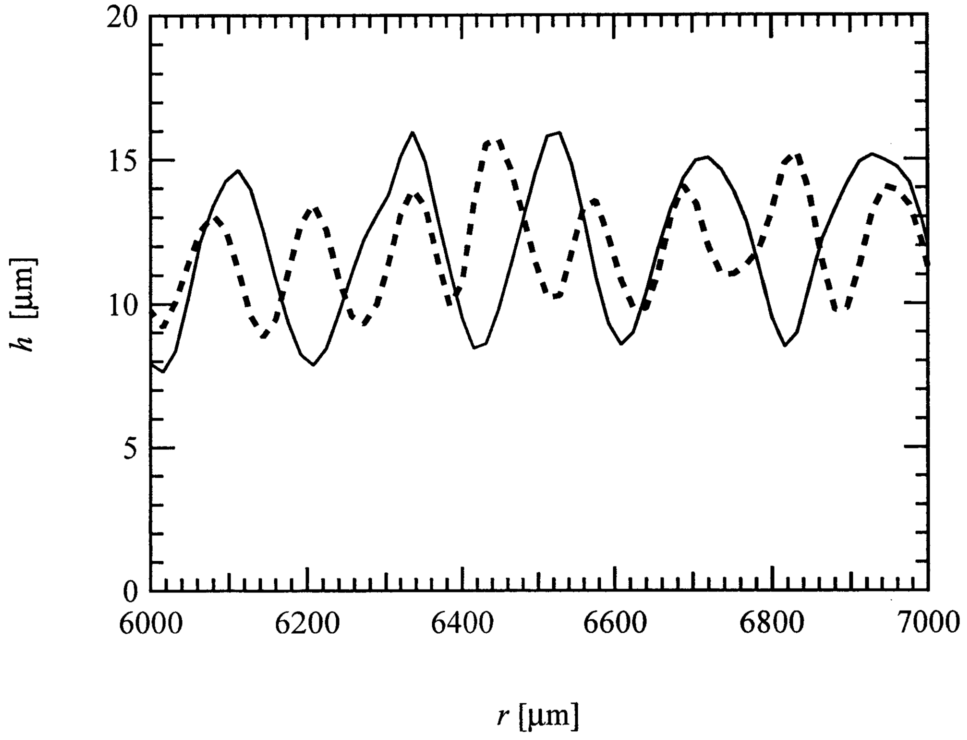

Figure 6-3: Scanning a droplet of silicone oil (L; Oh = 0.003, ϕ = 1.4) spreading on silicon substrate with scanning speed of $320mm/s$ with the direction (–) from contact line toward the center and (– – –) from center toward the contact line.

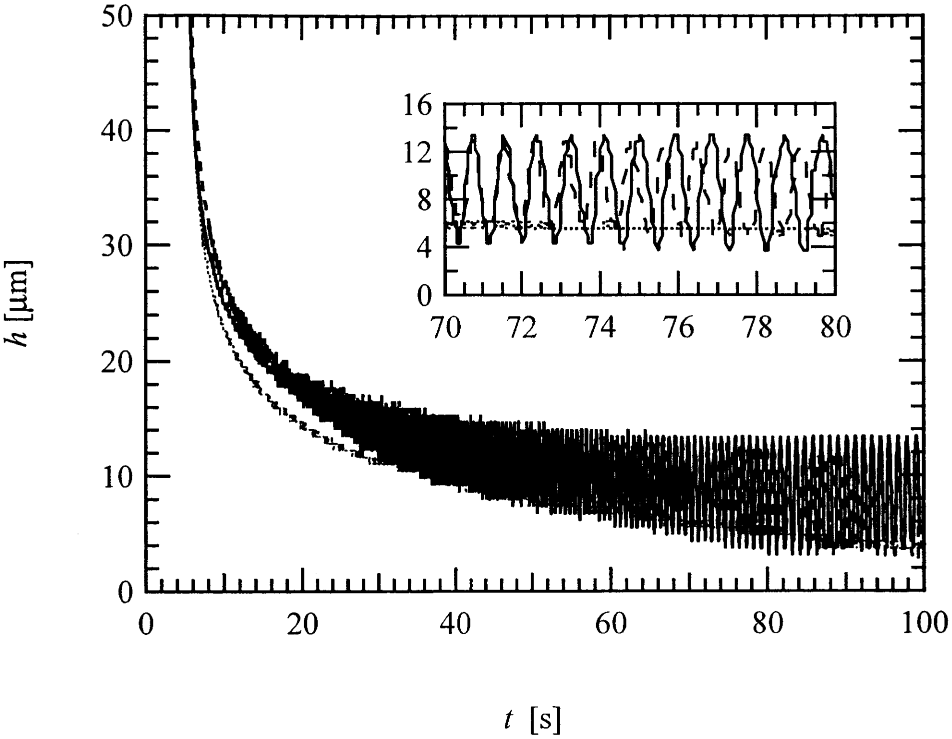

Figure 6-4: Effect of thermal conductivity of substrate on the onset of instability. Spreading of silicone oil (L, Oh = 0.003, ϕ = 1.39) on (...) glass; (– – –) Brass; and (–) silicon substrates.

6.2.3 Effect of Substrate Thermal Conductivity

Several materials have been used as substrates in our experiments and their thermophysical properties are found to have a pronounced effect on this new type of Marangoni instability. In figure 6-4 we show the effect of the thermal conductivity of the substrate on the stability characteristics. Three different smooth substrates were used to observe the spreading of the lowest viscosity silicon fluid (L). The thermal diffusivities of the selected materials are: glass ($\alpha = 3.40 \times 10^{-7} m^2/s$), brass ($\alpha = 3.41 \times 10^{-5} m^2/s$), and silicon ($\alpha = 9.34 \times 10^{-5} m^2/s$). The thermal diffusivity of silicon and brass are close to each other and both are good thermal conductors. The instabilities that develop during the spreading of a volatile liquid on these surfaces are very similar, the amplitudes of oscillation are almost identical and the critical film

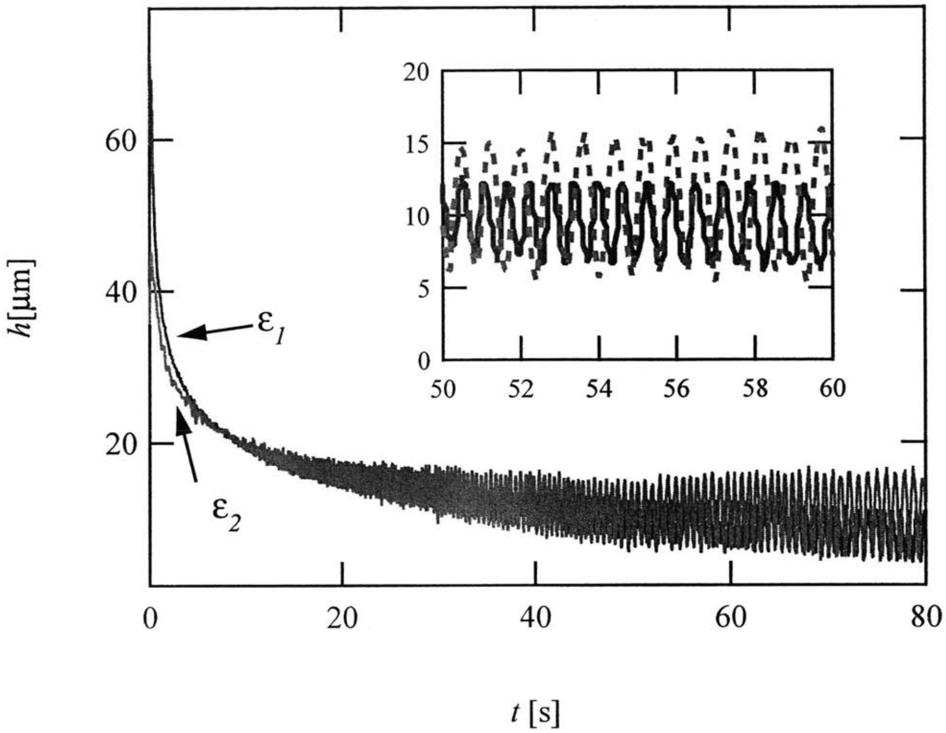

Figure 6-5: Effect of substrate roughness on spreading and instability. Silicone oil (L, Oh = 0.003, f = 1.39) drop spreading on copper substrates of characteristic roughness (−) $\varepsilon_1 = 1.13 \times 10^{-6} m$, and (− − −) $\varepsilon_2 = 1.83 \times 10^{-5} m$.

thickness for onset of instability are very close to each other. However, although the silicon fluid readily wets the smooth glass surface, the substrate material is a thermal insulator with a much smaller thermal diffusivity. No surface oscillations are observed during the steady spreading of the drop across the glass surface. It is thus clear that heat transfer from the underlying substrate is very important in driving the onset of Marangoni instability in the fluid film.

6.2.4 Effect of Surface Roughness

The experiments described above have all been carried out on relatively smooth surfaces. It is already known that changes in surface roughness significantly affect the steady spreading of viscous fluid [18]. The rate of surface area generation will affect the coupled heat and mass transfer rate arising from evaporation of the fluid. Furthermore, our observations above show that the onset of instability occurs at very small film thicknesses; the microscopic surface roughness of the substrate may thus also be expected to affect the onset of instability in a volatile liquid. In order to investigate this, we used two different thermally-conductive copper surfaces with controlled degrees of surface roughness and random orientation. Measurements using a surface profilometer (DEKTAK3) gave average roughness values of $\varepsilon_1 = 1.13 \times 10^{-6} m$ and $\varepsilon_2 = 1.83 \times 10^{-5} m$. These surfaces were then used as substrates to investigate spreading of a liquid micro-droplet of the least viscous and most unstable fluid (L; $Oh = 0.003$, $\phi = 1.39$).

In figure 6-5 we demonstrate the effect of surface roughness on the thermocapillary instability of volatile liquids during the spreading process. Prior to onset of instability, the rate of steady spreading is observed to be slower for the surface with smaller surface roughness than for the substrate with higher surface roughness The critical film thickness at onset of instability appears to be approximately the same for both cases ($h_{crit} \approx 20\mu$m) but the amplitude of oscillations on the rough surface are substantially larger. Details of the surface perturbations are shown in the inset to figure 6-5. Fourier analysis of such local signal segments shows that the waveform of the oscillations for the lower surface roughness case are essentially sinusoidal in nature whereas the disturbances propagating over the substrate with high surface roughness develop strongly non-linear characteristics when the film becomes very thin.

6.2.5 Effect of Liquid Volatility

We have argued earlier that this instability is a Marangoni instability driven not by imposed temperature gradients but by gradients arising naturally as a result of evaporation. The latent heat of evaporation (ΔH_ν) of the spreading liquid should thus play a central role in the critical onset conditions. To investigate this, we utilized a special grade of silicone oil (Gelest Inc., DMS-T07R) with comparable properties to fluids L and M but with a much lower volatility ($\Delta H_\nu^{DMS-T07R} = 108.7 kJ/mole$, cf. For fluid L, $\Delta H_\nu^L = 12.9 kJ/mole$).

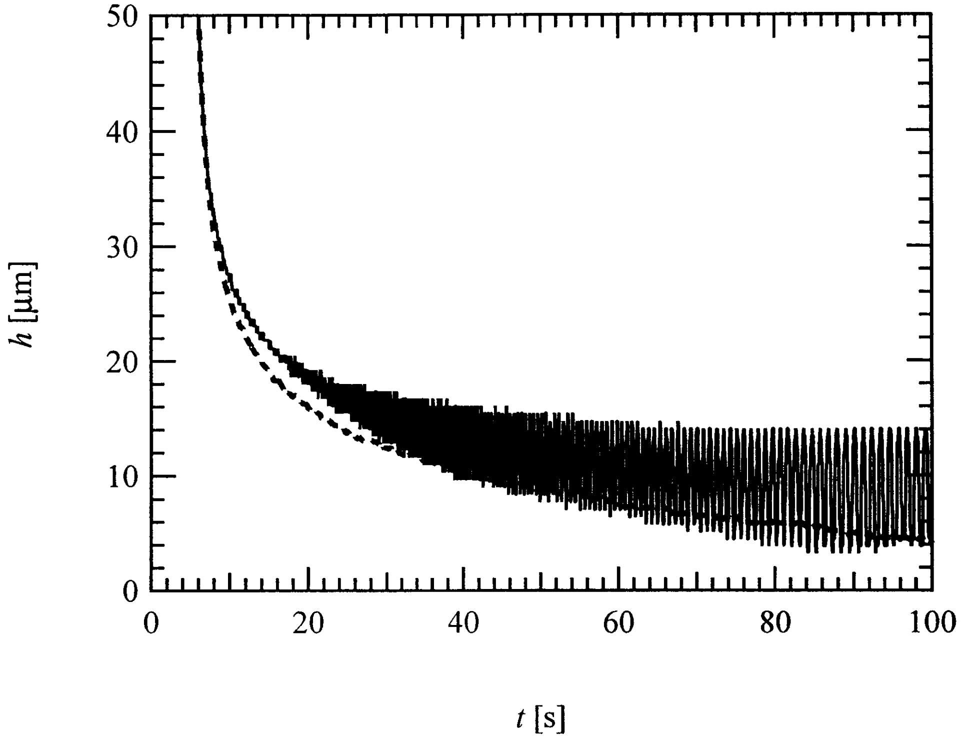

Figure 6-6: Effect of volatility of liquid on the onset of instability. Spreading of volatile silicone oil (–, L, Oh = 0.003, ϕ = 1.39) and non-volatile silicone oil (– – –, NV, Oh = 0.02, ϕ = 1.3) on silicon substrate. No instability was observed for non-volatile silicone oil.

It can be seen from figure 6-6 that the spreading characteristics of the volatile and non-volatile silicone oils on a smooth silicon substrate are dramatically different. At short times, both droplets exhibit the same rapid initial decrease in film thickness. For both fluid droplets the spreading parameters correspond to $\phi > 1$ and $Oh \ll 1$, so that spreading is controlled by a balance of gravitational and inertial forces which are identical for both droplets. As the film spreads out and the surface area increases, evaporative heat and mass transfer losses become increasingly important. The evaporatively-driven Marangoni instability is clearly present for the volatile liquid (L) whereas the non-volatile silicone oil continues to spread steadily on the silicon substrate without indications of surface disturbances.

The parameter controlling onset of instability is the dimensionless interfacial thermal resistance, $\mathcal{R}$. This parameter can be evaluated using the tabulated values of the thermal conductivity, latent heat of evaporation and the known molecular properties of the silicone oil which control the heat/mass transfer coefficient. It will be shown in the next section that this parameter is inverse proportional to the thickness of the drop. As each microdroplet spreads, the local thickness decreases, and consequently the interfacial resistance, $\mathcal{R}$ increases. For the volatile silicone oil, $\mathcal{R}_L$ is two order of magnitudes larger than $\mathcal{R}_{NV}$ (cf. next section) and thus attains the critical value $\mathcal{R}_{critical}$ at a much larger film thickness than the less-volatile fluid.

6.3 The two-dimensional disturbance equation

In this section we provide a two-dimensional model that governs the physics of this problem. We analyzed the instabilities of the system and its important parameters. Finally, the results of the calculations are compared with experimental observations from the previous section.

Consider a drop of liquid on a horizontal surface located at the position $y = 0$ and kept at a constant temperature $T = T_0$. The drop is composed of a volatile Newtonian liquid and surrounded by a passive gas, which viscosity and thermal conductivity are taken to be very small compared to those of the liquid. The far-field temperature

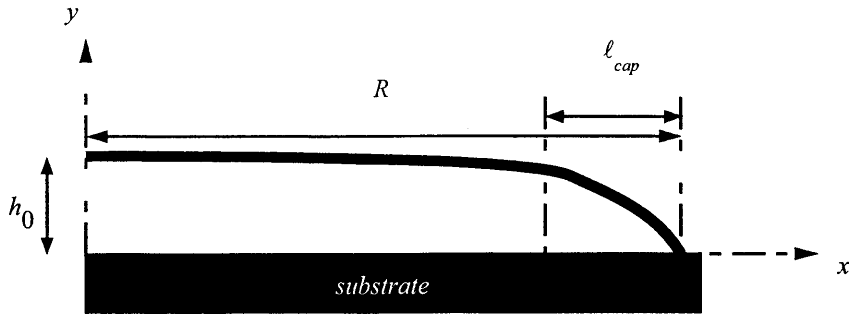

Figure 6-7: The geometry of the spreading film.

is T_0. The drop, shown in figure 6-7, is two-dimensional in Cartesian coordinates (x, y). The shape of the interface between the spreading liquids and the ambient gas is denoted by $y = h$, and the position of the contact line is given by $x = R_0$. We considered the region of the film far enough from the contact line, $x < R_0 - \ell_{cap}$. ℓ_{cap} is the capillary length which is defined as $\ell_{cap} = \sqrt{\sigma/\rho g}$ where g is the magnitude of the gravitational acceleration, and ρ is density of the liquid.

This problem is formulated by using the lubrication analysis. This analysis is only valid for highly viscous films of fluids, which can be identified by the Ohnesorge number, $Oh = \mu/\sqrt{\rho g R} \times (R/h)$, where μ is the viscosity of the liquid. The physical meaning of the ohnesorge number is the ratio of the viscous forces to the inertia forces in the presence of the capillary force. Therefore, large Ohnesorge number correspond to the spreading of a drop when viscous and capillary forces are important and drops with small Ohnesorge numbers are those with inertia and capillary forces interacting. Here we consider the case of a drop with large Ohnesorge number.

If u is the velocity component in the x direction (uniaxial flow), the equation of motion for a spreading viscous film, when gravity effect is negligible can be written as:

$$\mu \frac{\partial^2 u}{\partial y^2} = \frac{\partial P}{\partial x} \tag{6.2}$$

where $P = P(x)$ is the pressure. The rigid plane is considered to be impenetrable, perfectly conducting material. Equation 6.2 is subject to the following boundary conditions:

$$y = 0 \quad : \quad u = 0 \tag{6.3}$$

$$y = h \quad : \quad \mu \frac{\partial u}{\partial y} = \frac{\partial \sigma}{\partial x} \tag{6.4}$$

After integration and applying the boundary conditions, flow rate per unit depth, q', of the spreading liquid is found to be

$$q' = \int_0^h u\, du = \frac{1}{2\mu} \frac{\partial P}{\partial x} \left(-\frac{2h^3}{3} \right) + \frac{h^2}{2\mu} \frac{\partial \sigma}{\partial x} \tag{6.5}$$

Pressure at the interface between the liquid film and the ambient gas is given by

$$P = -\sigma \frac{\partial^2 h}{\partial x^2} \tag{6.6}$$

therefore the pressure gradient in x direction is

$$\frac{\partial P}{\partial x} = -\sigma \frac{\partial^3 h}{\partial x^3} - \frac{\partial \sigma}{\partial x} \frac{\partial^2 h}{\partial x^2} \tag{6.7}$$

Also, evolution of free surface of the film can be derived from continuity equation:

$$\frac{\partial h}{\partial t} + \frac{\partial q'}{\partial x} = -\frac{j''}{\rho} \tag{6.8}$$

where j'' is the evaporative mass flux with unit of kg/sm^2.

By combining equations 6.5, 6.7, and 6.8, the final for of surface evolution of and evaporative liquid drop is given by:

$$\frac{\partial h}{\partial t} + \frac{\partial}{\partial x} \left(\frac{\sigma h^3}{3\mu} \frac{\partial^3 h}{\partial x^3} \right) + \frac{\partial}{\partial x} \left(\frac{1}{\mu} \frac{\partial \sigma}{\partial x} \left(\frac{h^3}{3} \frac{\partial^2 h}{\partial x^2} + \frac{h^2}{2} \right) \right) + \frac{j''}{\rho} = 0 \tag{6.9}$$

The variation of surface tension in x direction, $\partial \sigma / \partial x$, can happened as a result of temperature or concentration gradient in the liquid film. Since the spreading liquid is considered to be a pure substance in this formulation, concentration gradient does not exist in this problem.

For a thin film of liquid spreading on a solid surface, conduction in x direction is negligible, therefore energy equation can be written as

$$\frac{d^2 T}{dy^2} = 0 \tag{6.10}$$

where T is temperature of the liquid. At the free surface boundary, conduction heat transfer inside the liquid is equal to heat that leaves the free surface through evaporation process (convection heat transfer is negligible) and temperature at substrate is assumed to be constant due to the high conductivity of the substrate:

$$y = 0 \ : \ T = T_w \tag{6.11}$$

$$y = h \ : \ -k_f \frac{dT}{dy} = j'' \Delta H_\nu \tag{6.12}$$

where k_f is the thermal conductivity of the liquid, ΔH_ν is the latent heat of evaporation, and T_w is the substrate temperature. It is assumed that the thermal conductivity of the substrate is very high therefore its temperature is always equal to the ambient temperature, $T_w = T_0$.

Solution to the energy equation is a linear temperature profile in y direction:

$$T = T_w + \frac{j'' \Delta H_\nu}{k_f} y. \tag{6.13}$$

To relate the dependence of the interfacial temperature, T_i, and the interfacial mass flux, we have used the analysis by Palmer [89]. The linearized form of this relation is given as [84]:

$$j'' = \mathcal{H}_m (T_i - T_{Sat}) \tag{6.14}$$

where

$$\mathcal{H}_m = \frac{\hat{\alpha} \rho_g \Delta H_\nu}{T_{Sat}^{3/2}} \sqrt{\frac{M_w}{2\pi \bar{R}}} \tag{6.15}$$

T_{Sat} is the absolute saturation temperature, ρ_g is density of the gas, $\hat{\alpha}$ is the accommodation coefficient, $\bar{R}$ is the universal gas constant, and M_w is the molecular weight of the vapor. The unit for $\mathcal{H}_m$ is: $\mathrm{kg\,m^2 s^{-1} K^{-1}}$ in SI unit system.

Let non-dimensionalize temperature, mass flux and thickness of the film as

$$\Theta = \frac{T - T_{Sat}}{T_w - T_{Sat}} \tag{6.16}$$

$$J = \frac{h_0 \Delta H_\nu}{k_f (T_w - T_{Sat})} j'' \tag{6.17}$$

$$h^* = \frac{h}{h_0} \tag{6.18}$$

therefore, the dimensionless form of temperature field and evaporative mass flux can be found as:

$$\Theta = 1 - \frac{y^*}{h^* + \mathcal{R}} \tag{6.19}$$

$$J = \frac{1}{h^* + \mathcal{R}} \tag{6.20}$$

where $y^* = y/h_0$ and $\mathcal{R}$ is the interfacial thermal resistance which is defined as:

$$\mathcal{R} = \frac{k_f}{\mathcal{H}_m h_0 \Delta H_\nu} \tag{6.21}$$

This dimensionless parameter, $\mathcal{R}$, quantifies the relative magnitude of the evaporative resistance to heat transfer at the interface compared to the conductive resistance of the liquid film itself. It is analogous to the inverse of the Biot number encountered in convection-diffusion heat transfer problems, $Bi^{-1} = k_s/h_c\delta$, in which δ is the length scale of the system, h_c is the heat transfer coefficient for convection into a liquid and k_s is the thermal conductivity of the solid boundary.

For a non-volatile liquid, $\mathcal{R} = 0$, there would be no evaporation at the free surface, therefore its temperature will be in equilibrium with the environment and the temperature gradient $(T_w - T_i)/h \rightarrow 0$. if $\mathcal{R} \rightarrow \infty$, it means the conductive resistance inside the liquid film is very small, $h_0/k_f << 1$, thus interface temperature will be very close to the substrate temperature, $T_i = T_w$. In this case the free surface temperature remains constant along the interface between fluid and vapor.

By introducing the following set of dimensionless variables:

$$\epsilon = \frac{h_0}{\ell_{cap}}, t^* = \frac{\sigma_0 t}{\mu h_0}\epsilon, x^* = \frac{x}{h_0}\epsilon \tag{6.22}$$

the equation 6.9 can be written as:

$$\frac{\partial h^*}{\partial t^*} + \frac{E}{h^* + \mathcal{R}} + \frac{1}{3}\frac{\partial}{\partial x^*}\left(h^{*3}\frac{\partial^3 h^*}{\partial x^{*3}}\right) + \mathcal{R}\frac{Ma}{Pr}\frac{\partial}{\partial x^*}\left(\frac{h^{*2}}{(h^* + \mathcal{R})^2}\frac{\partial h^*}{\partial x^*}\right) = 0 \tag{6.23}$$

where Marangoni number, Ma, Prandtl number, Pr, and evaporation number, E, are defined as:

$$Ma = \frac{\Delta T \frac{\partial \sigma}{\partial T}}{\sigma_0}\epsilon \tag{6.24}$$

$$\begin{aligned} Pr &= \frac{\mu}{\rho\alpha} && (6.25) \\ E &= \frac{k_f(T_w - T_{Sat})}{\mu \Delta H_\nu}\epsilon^{-1} && (6.26) \end{aligned}$$

Evaporation number, E, represents the ratio of the viscous time scale, $t_v = h_0^2\rho/\mu$, to the evaporative time scale, $t_e = \rho h_0^2 \Delta H_\nu / k_f(T_w - T_{Sat})$. The latter is a measure of the time required for an initially stationary film to evaporate to dryness on a horizontal substrate.

Here the first term in the right hand side of the equation 6.23 represents the rate of volumetric accumulation, the second term is the mass loss, the third one is the stabilizing capillary term, and the forth term is represent the destabilizing thermocapillary effect.

If the drop is considered to be an evaporating thin layer and does not spread, the evolution equation have a solution of

$$h^* = -\mathcal{R} + \sqrt{(\mathcal{R}+1)^2 - 2Et^*} \tag{6.27}$$

For low evaporation rates however, evaporation number, E, is very small but the thermocapillary effects still play a big role in this problem. We can rewrite equation 6.23 with this assumption as:

$$\frac{\partial h^*}{\partial t^*} + \frac{1}{3}\frac{\partial}{\partial x^*}\left(h^{*3}\frac{\partial^3 h^*}{\partial x^{*3}}\right) + \mathcal{R}\frac{Ma}{Pr}\frac{\partial}{\partial x^*}\left(\frac{h^{*2}}{(h^* + \mathcal{R})^2}\frac{\partial h^*}{\partial x^*}\right) = 0 \tag{6.28}$$

The base solution for equation 6.28 is obviously $h^* = 1$. This solution is valid in the so called ‘pancake region’ which is part of the liquid film far from the contact line.

We employ linear stability theory and perturb the base state by a small amount, $\varepsilon h'$:

$$h^* = 1 + \varepsilon h' \tag{6.29}$$

We assume disturbance quantity, h', of the form

$$h'(x^*, t^*) = \mathrm{Re}(H\,(x^*)\, e^{\mathrm{i}(kx^* - \omega t^*)}) \tag{6.30}$$

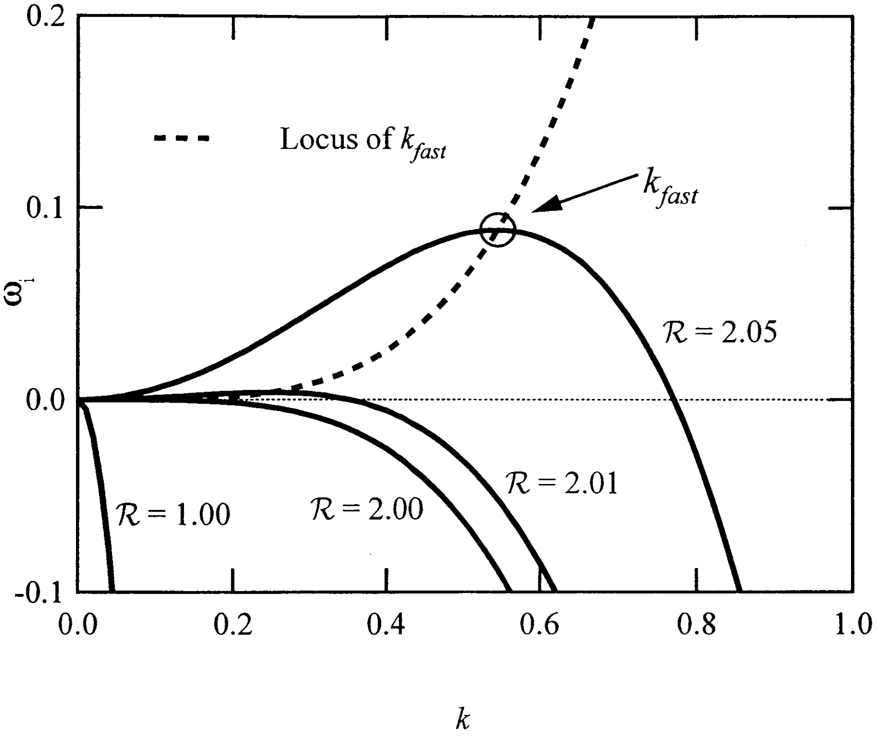

Figure 6-8: The amplitude of the growth rate, ω_i as a function of the dimensionless wave number, k, for various values of the interfacial thermal resistance, $\mathcal{R}$. The value of Ma/Pr is constant, $Ma/Pr = 50$.

where k and $\omega = \omega_r + i\omega_i$ are the dimensionless wave number and the dimensionless complex growth rate of the instability, respectively.

The dispersion relation for the normal modes is find to be:

$$\omega_r = 0, \ \omega_i = -\frac{1}{3}k^4 + \frac{Ma}{Pr}\frac{\mathcal{R} - 2}{\mathcal{R}^2}k^2 \tag{6.31}$$

In the next section we analyze this relation and compare the analytical results with the our experimental results.

6.4 Stability analysis results

In order to analyze the behavior of the instabilities, the dimensionless the growth rate of the amplitude , ω_i, is plotted as a function of dimensionless wave number,

k, using equation 6.31 for different values of the interfacial thermal resistance, $\mathcal{R}$, in figure 6-8. For $0 < \mathcal{R} < 2$, the growth rate of the amplitude, ω_i, is negative for all the values of the modified Marangoni number, $\widetilde{Ma} = Ma/Pr$, and k. $\mathcal{R} = 2$ is the onset of the instability and for $\mathcal{R} > 2$, the growth rate become positive which means the system is unstable.

The fastest growing mode of the instability, k_{fast}, is the wave number which gives the maximum value for the growth rate as it is shown in figure 3. k_{fast} value can be derived from equation 6.31 as

$$k_{fast} = \sqrt{\frac{3}{2}\widetilde{Ma}\frac{\mathcal{R}-2}{\mathcal{R}^2}} \tag{6.32}$$

As it is shown in equation 6.32, k_{fast} depends on both $\mathcal{R}$ and $\widetilde{Ma}$. In figure 6-9(b), k_{fast} is plotted as a function of $\widetilde{Ma}$ for various values of $\mathcal{R}$. For any $\mathcal{R}$, when the modified Marangoni number increases, the fastest growing mode of instability increases. This shows when liquid spreads faster, or its surface tension is more sensitive to change of temperature, $\partial\sigma/\partial T$, there will be more surface waves on the interface.

In figure 6-9(b), k_{fast} is plotted as a function of $\mathcal{R}$ for various values of $\widetilde{Ma}$.We indicated in the previous section that $\mathcal{R} = 0$ means non-evaporating film, and as expected no instability is predicted by the analysis. As seen in this figure, for $\mathcal{R} < 2$, $k_{fast} = 0$ because the system is stable. At $\mathcal{R} = 2$, for any value of the Marangoni number, flow become unstable and k_{fast} increases rapidly ($\partial k_{fast}/\partial\mathcal{R} = \infty$). Then k_{fast} reaches its maximum value and decays for larger values of $\mathcal{R}$ and as $\mathcal{R} \to \infty$, $k_{fast} \to 0$. It is interesting to notice system will be unstable for all the values of $\mathcal{R} > 2$ but it is stable at $\mathcal{R} = \infty$. As we mentioned in the previous section, when $\mathcal{R} = \infty$, interface temperature, T_i, will be same as substrate temperature, T_w, therefore there is no temperature gradient in x direction to initiate the instability.

In order to confirm our analysis, we compare these results with the experimental results which have been presented in this chapter. These experiments have been performed by putting a drop of silicone oil liquid (provided from Gelest Inc.) on silicon substrate. Evolution of the interface, $h(t)$, was measured as the drop spread on the surface by a confocal surface metrology system (Keyence, LT-8110).

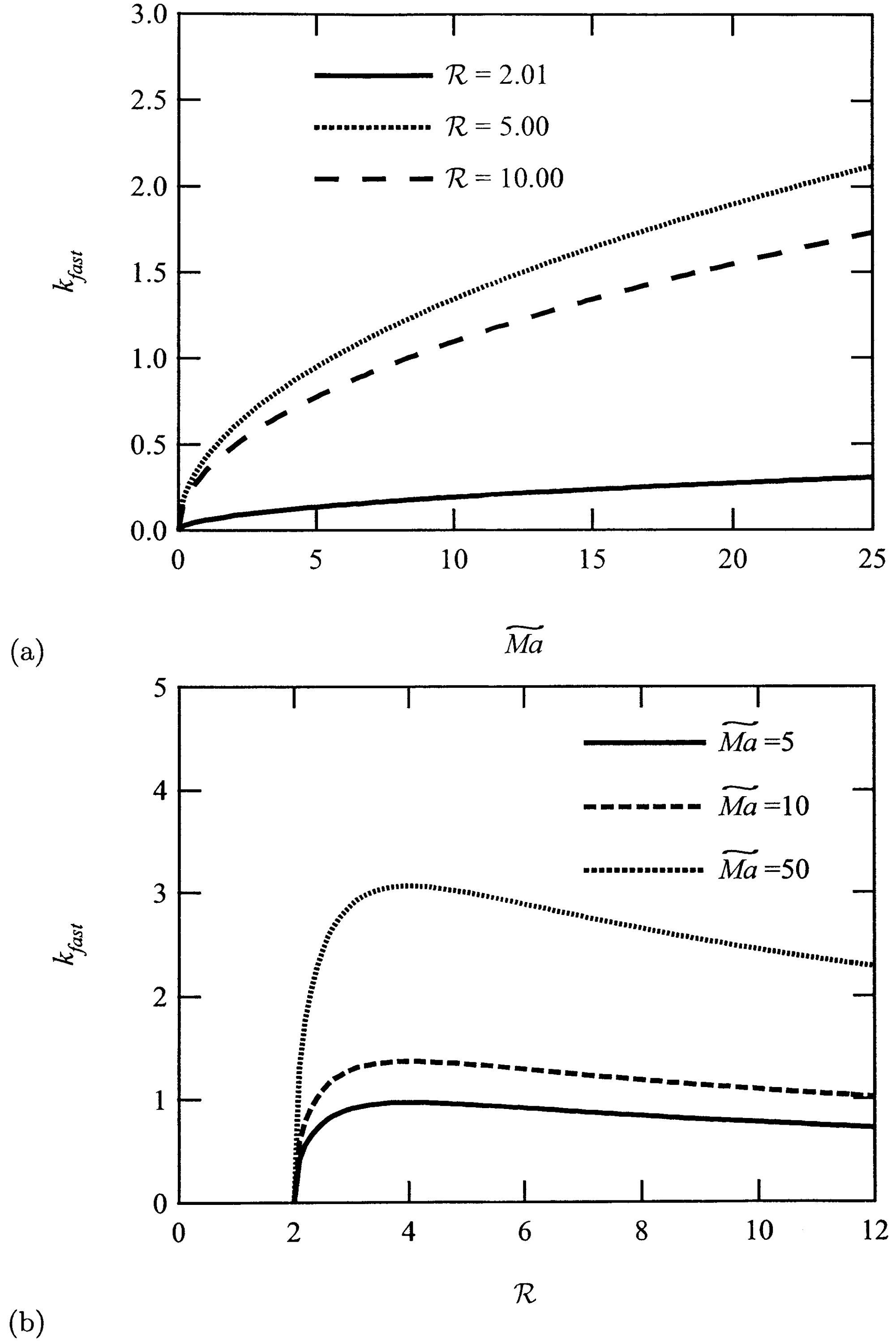

Figure 6-9: Effect of (a) the Marangoni number, $\widetilde{Ma}$, and (b) the interfacial thermal resistance, $\mathcal{R}$ on the fastest growing wave number.

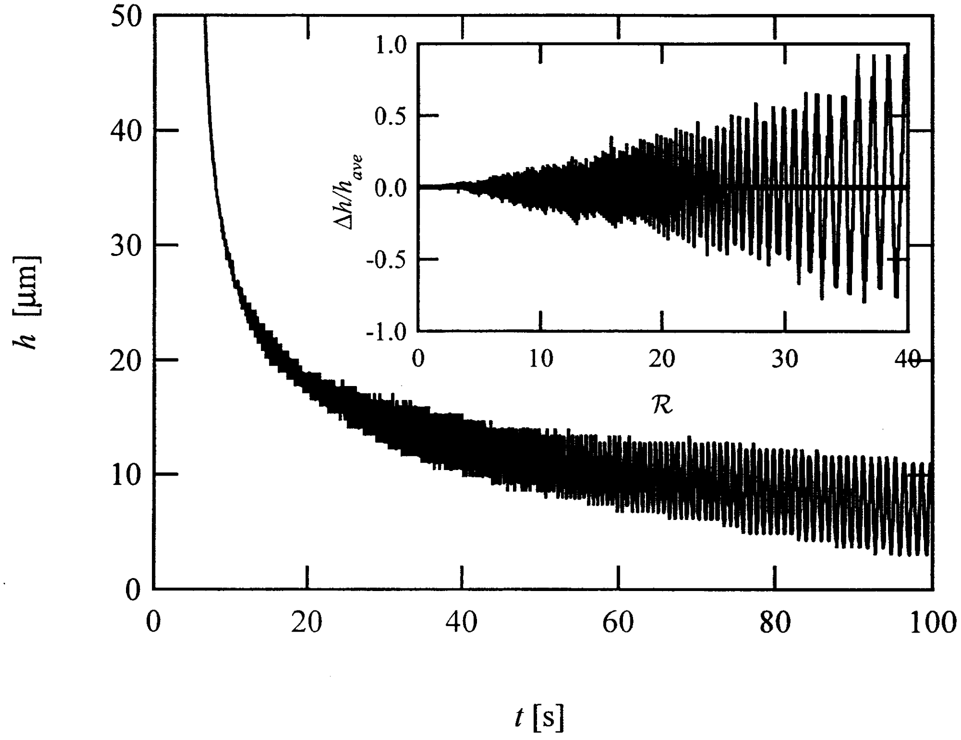

Figure 6-10: Onset of instability for a spreading drop slightly volatile of silicone oil on a silicon substrate. The inset plot is deviation from the average thickness as a function of the interfacial thermal resistance.

In figure 6-10, we show the evolution in the height of the spreading droplet close to onset of instability for a drop of silicone oil (DMS-T01, $\mu = 0.001$ Pa.s, $\sigma = 0.017$ N/m, and $\mathcal{R} = 5.25 \times 10^{-5}/h$). The evaporation number, E, for this liquid is approximately equal to 0.08 which justifies our assumption on neglecting the mass loss term in equation 6.23. The onset of the instability is at the height of $h = 27 \times 10^{-6}$ which gives $\mathcal{R} = 1.94$. This is very close to the prediction of the theory for $\mathcal{R}_{critical} = 2$. The inset of figure $5(a)$, is another presentation of the same data. The vertical axis is deviation of the free surface from its average value, $\Delta h/h_{ave}$ where h_{ave} is fitted power law to the data and $\Delta h = h - h_{ave}$. The horizontal axis is the interfacial thermal resistance, $\mathcal{R}$. As it shown, deviation from h_{ave} starts at approximately $\mathcal{R} = 2$ as it was predicted by our analysis.

6.5 Discussions

A non-invasive optical technique based on confocal microscopy has been developed and been used to investigate steady spreading and the onset of an evaporatively-driven Marangoni instability of spreading liquid microdroplets.

Time-resolved point-wise measurements of the evolution in the free surface of spreading fluid drops have been used to investigate the onset of an evaporatively-driven Marangoni instability. The onset of instability occurs once the height of the liquid film has fallen below a critical value and it results in periodic surface fluctuations which appear to travel radially-inwards towards the droplet center. Experiments with a range of fluids have shown that as the viscosity of the fluid is increased (and the rate of spreading concomitantly decreased) the amplitude of the disturbances is progressively dampened.

The effects of substrate thermal diffusivity and surface roughness on the disturbance characteristics have also been shown in this paper. When droplets spread over substrates with a low thermal diffusivity (such as glass) no instability can be detected whereas for highly thermally-conducting substrates (for example silicon, copper and brass), ripples were present on the free surface of the spreading droplet. Increasing the surface roughness of the substrate leads to larger amplitude and more nonlinear waveforms.

Mathematical modeling of this interfacial instability is complicated due to the coupled mass and heat transfer from the evaporating fluid droplet and the unsteady base flow of the spreading film. A detailed linear stability analysis is currently being performed using the lubrication framework developed by Ehrhard & Davis [39] and Oron et al. [84]. Physically, the mechanism of instability appears to be the following: evaporation of the volatile material from the fluid film results in a loss of thermal energy from the fluid droplet and a consequent cooling in the droplet. The heat and mass flux are largest near the singular contact line and consequently the liquid is coldest here; a surface temperature gradient thus exists along the surface of the thin fluid film which can drive a secondary flow. Under quasi-steady state conditions this evaporative heat and mass flux from the free surface is provided by heat transfer from the underlying substrate and conduction through the insulating liquid film; there is thus also a temperature gradient normal to the fluid layer. The resulting temperature gradients within the drop drive secondary thermocapillary surface flows which can be unstable if the temperature gradient is large enough, although since the gradients exist both parallel and normal to the free surface it is not clear a priori whether to refer to them as Marangoni or hydrothermal instabilities [100]. The experimental observations showing that the waves propagate towards the central (warmer) region of the droplet suggest that the waves are principally hydrothermal in nature [105].

The observed sensitivity of the instability to the thermal properties of the substrate is consistent with the picture above as the magnitude of the heat and mass transfer rate from the surface and thus the temperature profile within the film are constrained by the energy supply from the substrate below. It should be noted that although the free surface instability documented in this paper shares some characteristics with the steady and unsteady secondary flows documented in the coffee drop problem [31] or in tear-ducts of wine [60], it is fundamentally different in origin. The interfacial Marangoni stresses that drive the disturbances are not compositional in nature since the spreading silicone oils are single-component liquids. The destabilizing Marangoni stresses arise from the coupled heat and mass transfer resulting from evaporation. Although the thermal dependence of the material properties (especially the surface tension) are essential in this instability, it is not simple to define a critical capillary or Marangoni number since the spreading velocity of the droplet is continuously decreasing with time. Analysis shows that the parameter controlling the temperature profile in the film and thus controlling the onset condition of the thermocapillary instability is the dimensionless interfacial thermal resistance, $\mathcal{R}$. Since the relative magnitude of this interfacial resistance is inversely proportional to the thickness of the liquid droplet, $\mathcal{R}$ increases as the film spreads and thins. When $\mathcal{R}$ is larger than a critical value, $\mathcal{R}_{critical}$, infinitesimal disturbances on the surface of the spreading drop grow spontaneously. More volatile liquids have larger values of $\mathcal{R}$ in comparison to non-volatile liquids, due to the smaller latent heat of evaporation. As a consequence, instabilities develop at larger film thicknesses for more volatile materials. In our experiments, a non-volatile silicone oil did not show instability even at thicknesses of order $1mm$ whereas a more volatile silicone oil became unstable at thickness of approximately 20μm. From the definitions of $\mathcal{R}$ and $\mathcal{H}_m$ it can be seen that $\mathcal{R} \sim \Delta H_v^{-2}$ and thus it would be expected that the non-volatile liquid film will not become unstable until the thickness falls below approximately 0.4μm.

Chapter 7

Characteristics of the moving contact line for non-Newtonian liquids

7.1 Introduction

In the previous chapters, we have presented the macroscopic and microscopic features of spreading viscous drops on solid surfaces. Those studies, however, only focused on Newtonian fluids. In many important commercial operations, the coating fluid may be non-Newtonian and the rheological properties of the fluid can have very important effects in the region of high shear rate close to the moving contact line. Due to the complicated physics of this problem, until recently only relatively few studies have focused on this challenging issue. However, the interest in this subject is growing in the coating and paint industries. Polymer melts with high molecular weight, dilute polymer solutions (e.g. Boger fluids), and photo-resist solutions in the microfabrication process are examples of such fluids. The effect of the non-Newtonian rheology of a fluid can have significant effect at the vicinity of the moving contact line where the singularity in force occurs. For example viscosity of a shear-thinning fluid would be reduced in the high shear rate region which increase the spreading rate.

The shear-thinning effect close to the moving contact line was also used to remove the singularity at the moving contact line [119].

In this chapter, we focus on the macroscopic and microscopic characteristics of non-Newtonian fluids in the spreading process. We have chosen to investigate the spreading of two families of non-Newtonian fluids:

Highly entangled polymer melts: This type of non-Newtonian fluid is used to examine the effect of polymeric entanglements on the spreading of fluids on solid surfaces. The impact of molecular length scales and entanglement close to the contact line (in the high shear rate region) and the shape of the free surface of the drop are of interest. Due to very high molecular weight, these fluids are very viscous as we discuss in next section.

High viscosity dilute polymer solutions: These visco-elastic fluids are usually referred to as 'Boger fluids' [13]. They are studied to investigate the effect of visco-elasticity in the spreading process. Due to the large (and constant) viscosity of these fluids, the Ohnesorge numbers for spreading of these fluids are larger than one and shear-thinning effects are minimal. This means that the effect of inertia is eliminated and the effect of elasticity on spreading process can be determined. The spreading power-laws and the visco-elastic effects in the vicinity of the contact line are of interest.

In this chapter, the basic physics of highly entangled polymer melts and Boger fluids will be briefly reviewed. Also, available theories on spreading of these types of fluids on solid surfaces are presented. Subsequently, the experimental results on the spreading of these liquids on solid substrate are presented. For highly entangled polymer melts, we have used a high molecular weight entangled polydimethylsiloxane (PDMS) and for the ideal elastic dilute polymer solution (Boger fluid), a high molecular weight polystyrene dissolved in an oligomeric styrene oil (PS025) has been used.

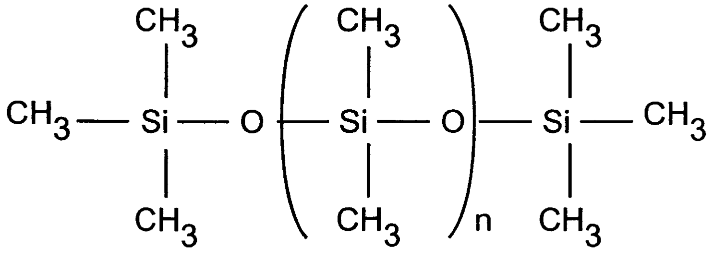

Figure 7-1: The chemical formulation of the PDMS, trimethylsiloxy terminated.

7.2 Theoretical background on non-Newtonian fluids

7.2.1 Rheology of the polymer melts

A polymer consists of one or more repeating subunits that are usually called *monomers*. These units are connected to each other to generate a long chain. This long chain is a macromolecule with a length that depends on the number of monomers. Along this chain, many different side groups or substituents as simple as hydrogen or CH_3 or as complex as cyclic ring structures can be attached. These side branches will change the properties of the polymers drastically. In this thesis, however, we restrict our study of polymer melts to polydimethylsiloxane (PDMS) obtained from Gelest Inc. As shown in figure 7-1, the repeating unit in this polymer is $SiO(CH_3)_2$ with n as the number of repeating subunits in the polymer chain. Since we are using a trimethylsiloxy terminated PDMS, the additional end groups are $SiO(CH_3)_3$ and $Si(CH_3)_3$. The molecular weight of the repeating unit m_0 is calculated to be 74 g/mole.

Flexible molecules permit rotational motions of one bond about another therefore a large number of configurations is available. The distribution of configurations in the melt can be modeled by a random walk. From this formula the time averaged mean-square distance, $\langle R^2 \rangle_0$, can be determined which characterizes the size of the molecule in its most probable or equilibrium configuration:

$$\langle R^2 \rangle_0 = n b_n^2 \tag{7.1}$$

where n is the number of repeating monomers of the primary chain backbone and b_n is the length of an "effective" random walk step. This model is usually called the freely jointed chain. However, clearly the bonds of a real macromolecule do not have complete freedom to rotate because of the bond angle restrictions that depend on the the orientation of a bond and its neighbors. Therefore, a new length scale (b_n) larger than the monomer length (l) is needed to represent an idealized random walk. Since bond angle restrictions make $\langle R^2 \rangle_0$ more expanded, b_n is larger than average bond length, l. Therefore, we can write:

$$\langle R^2 \rangle_0 = C_\infty n l^2 \tag{7.2}$$

where C_∞ is the characteristic ratio given by $C_\infty = (b_n/l)^2$.

One can also define a fully extended length, L_{max}, of the molecule, then another effective random walk step size b_K, which is also called Kuhn length, is defined as:

$$\langle R^2 \rangle_0 = L_{max} b_K \tag{7.3}$$

The effective freely jointed chain of length L_{max} would have $N_K = L_{max}/b_K$ rigid links, with length of b_K. Hence,

$$\langle R^2 \rangle_0 = N_K b_K^2 \tag{7.4}$$

Since the bonds are not collinear in ordinary polymers, L_{max} is less than nl. For tetrahedral bonding angles:

$$L_{max} = \sin\left(\arctan\sqrt{2}\right) nl = 0.816nl \tag{7.5}$$

By combining these equations, the number of Kuhn steps is given by $N_K = n(0.816^2/C_\infty)$ and the length of a Kuhn step is $b_K = l(C_\infty/0.816)$. Finally the mass of a Kuhn segment is $M_K = M_w/N_K$. A very comprehensive explanation of these derivations can be found in [71].

At this point, we would like to apply the preceding to the PDMS melts used in this study. First, we used the rheology data taken from the Gelest Inc. manual for PDMS and present the viscosity, η_0, of the PDMS as a function of the molecular

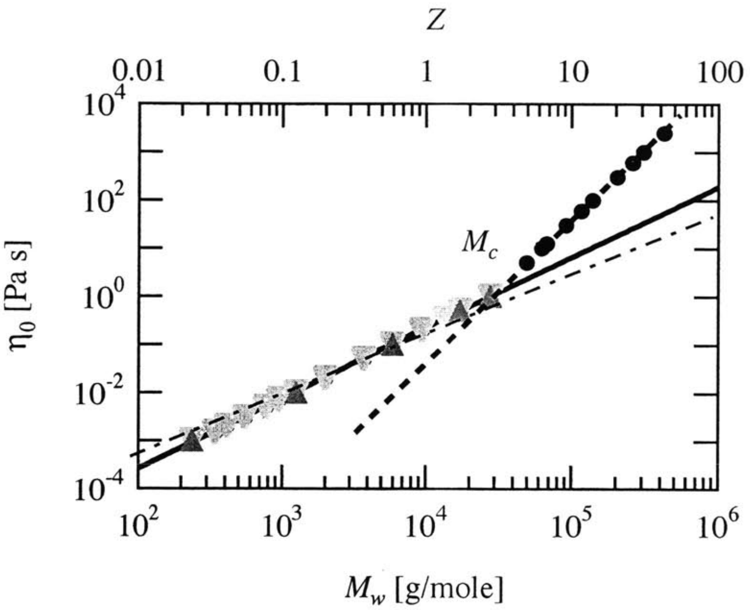

Figure 7-2: Relationship between the viscosity, η, and the molecular weight, M_w, of PDMS (From Gelest PDMS Manual). The solid line is $\eta \sim M_w^{1.3}$ and the dashed line is $\eta \sim M_w^3$. The dotted line is the linear scaling predicted by the Rouse model. Symbols with up triangles indicates those PDMS used in our experiments in previous chapters. Other triangles indicate Newtonian behavior of the fluids. The cross over point at which the polymer molecules start to entangle is called M_c.

weight, M_w, in figure 7-2. For PDMS with low molecular weights, the viscosity has a power-law relation with the molecular weight $\eta_0 \sim M_w^{1.3}$ shown with a solid line in the figure 7-2. The Rouse theory [71] for monodisperse linear chains predicts a linear relation in this regime as indicated by the dotted line. These fluids are used in our experiments in previous chapters.

At a critical molecular weight, usually denoted M_c, this functionality crosses over to a different power-law. In this region, the relation between the molecular weight of the fluid and its viscosity commonly is expected to have the following form [11]:

$$\eta \sim M_w^{3.4} \tag{7.6}$$

The regression to the data in this region, shown in figure ?? gives $\eta \sim M_w^3$. This power-law is shown by a dashed line in figure 7-2. The steep increase of viscosity with the molecular weight is caused by molecular entanglements, which are restrictions on molecular motion caused by the fact that molecules can not move through each other. Thus, molecules surrounded by others can not move freely but must reptate past each other. The theoretical power law exponent can be derived from reptation theory [71].

The theoretical Kuhn step expressions given above for the ideal Kuhn chain can be applied to these PDMS fluids. From the available data for PDMS [71, 43], we obtain $m_0 = 74$ g/mol, $j = 2$, and $C_\infty = 6.3$. Therefore, we can calculate the number of Kuhn steps, N_K, and mass of the Kuhn step, M_K, from the following relations:

$$N_K = \frac{M_w}{m_0/j}\frac{0.816^2}{C_\infty} = \frac{M_w}{350} \tag{7.7}$$

$$M_K = \frac{m_0}{j}\frac{C_\infty}{0.816^2} = 4.73 m_0 \tag{7.8}$$

The value of the mass of the Kuhn step for PDMS is thus calculated to be 350. The ratio of n/N_K is calculated to be 9.46 indicates that every Kuhn step contains approximately 10 monomer molecules. The values of N_K plotted in figure 7-3 are calculated using equation 7.7. As shown, the number of Kuhn steps at cross over point is $N_e = N_K \approx 80$ which corresponds to the molecular weight of $M_c = 28000$. From theoretical calculation [10], for PDMS $M_c = 28141$ which is very close to the experimental result.

The molecular weight between entanglements, M_e, for PDMS is given by Larson [71] and Ferry [43] to be approximately $M_e \approx 12263$. According to these references, M_e is usually about a fifth to a half as large as M_c. Also theoretical results [10] predicts $M_e = M_c/2$. According to our calculation, $M_c = 2.28 M_e$ which is within the range of conventional estimates. The magnitude of M_e depends on the "bulkiness" of the polymer molecules and the extent of the excluded volume. The bulkier the molecules are, the less free volume will be available for chain. The magnitude of M_e for PDMS is larger than most of the common polymers due to this effect.

The number of entanglements in the polymer is defined as $Z = M_w/M_e$. We also show this values on the top axis of figure 7-3 to represent the number of entanglement

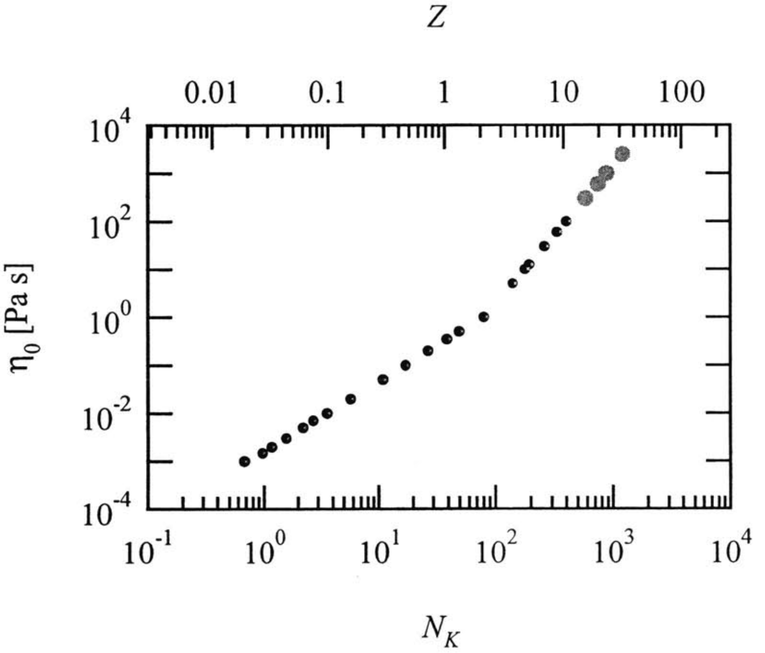

Figure 7-3: Relationship between the viscosity, η, and the Kuhn step, N_K, and the number of entanglements, Z, of PDMS. Data is reproduced from figure 7-2. The last four data points are those which are highly entangled polymer melts used in this chapter.

for high molecular weight PDMS. As shown, the last four samples in this data set are fully entangled molecules ($10 < Z < 35$). From the regression to the data, $\eta_0 = 3.32 \times 10^{-14} M_w^3$ and $\eta_0 = 0.06 Z^3$. Thus, we have used these fluids as working fluids in our experiments. In the next section, previous theoretical work on the spreading of entangled fluids will be reviewed.

7.2.2 Steady spreading of polymer melts

In chapter 3, the spreading of Newtonian fluids on solid surfaces was reviewed. Experimental measurements show that unentangled polymer melts with small molecular weights behave as Newtonian fluids except at very high shear rates. A perfectly wetting non-entangled polymer melt would thus be expected to follow the spreading power-laws derived in chapter 3.3 and the HVT law (equation 3.58). The effects of drop size and viscosity should scale in the same way as other Newtonian fluids and the different regimes of spreading still exist. However, earlier experiments by Schonhorn et al. [101] for the spreading of polymers with high molecular weights on solid substrates have demonstrated totally different behavior compared to Newtonian fluids. The measured dynamic contact angle did not have the same power-law relation as Newtonian fluid (the HVT law, table 3.1). Also it was reported by several groups [83, 99] that new foot-like structures have been detected close to the moving contact line for PDMS which were not present for Newtonian fluids. Polymer melts with high molecular weight (highly entangled molecules) may have significantly different behavior close to the moving contact line where the high shear rates lead to a loss of entanglements. The non-Newtonian behavior of these fluids can have drastic effects on the spreading rate and shape of the free surface of the drop especially in the vicinity of the moving contact line. In this section a review of the theoretical predictions on the spreading of the highly entangled polymer melts is presented.

First, let's revisit the idea of slip in the vicinity of the moving contact line. In presence of slip, for a simple shear flow with a velocity only in x direction (figure 7-4) using the Navier slip condition, the shear stress at the wall is proportional to the velocity at the wall :

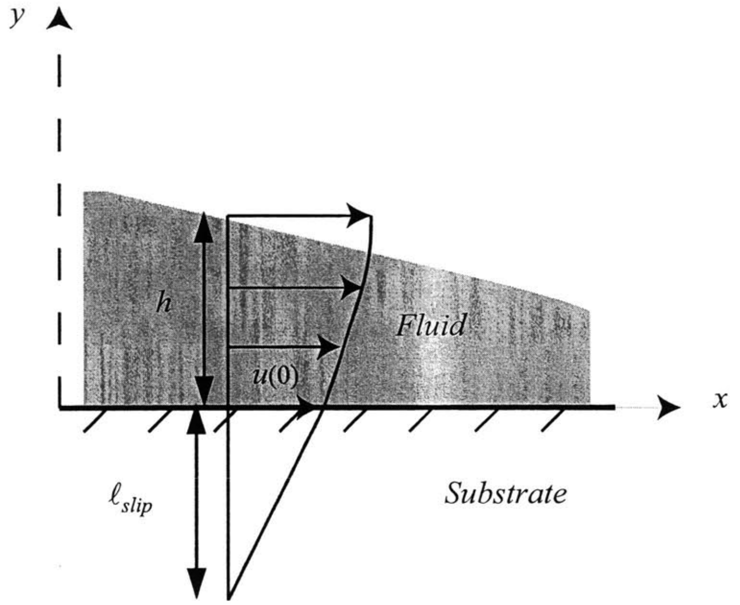

Figure 7-4: Velocity profile close to the moving contact line with slip at the wall.

$$\tau_w = Ku(0) \tag{7.9}$$

where K is the coefficient of proportionality and is independent of the molecular weight, M_w of the polymer melt [16]. As mentioned in the previous section, the high viscosity of polymer melts is caused by entanglement between the polymer molecules which must be absent for the molecules immediately adjacent to the smooth surface. Since the effect of entanglement is not present, we can expect K to scale as:

$$K = \frac{\eta_{mon}}{\ell_{mic}} \tag{7.10}$$

where η_{mon} is the viscosity of the monomer and ℓ_{mic} is the molecular length scale as defined before (equation 3.49). From the definition of shear stress, we know $\tau = \eta \partial u / \partial y$. The slip length ℓ_{slip} is defined as [16]:

$$\ell_{slip} = \frac{u(0)}{\left(\frac{\partial u}{\partial y}\right)_{y=0}} \tag{7.11}$$

Putting together equations 7.9, 7.10, and 7.11, one obtains the following relation for the slip length:

$$\ell_{slip} = \ell_{mic} \frac{\eta}{\eta_{mon}} \tag{7.12}$$

we can rewrite the equation 7.12 as a function of degree of polymerization, N_K. It is known [16, 71], $\eta \sim \eta_{mon}(N_K^3/N_e^2)$ where N_e is number of Kuhn steps at the cross over from non-entangle to entangled region. Therefore equation 7.12 can be written as:

$$\ell_{slip} = \ell_{mic}\frac{N_K^3}{N_e^2} = \ell_{mic}Z^3N_e \tag{7.13}$$

It is noted by Bruinsma [17] that the mobility of the polymer molecules [29] close to the surface can be different depending on their location in the bulk to close to the contact line. Bruinsma made a modification to equation 7.13 to include the effect the mobility. If $\mathcal{M}$ is the ratio of mobility of polymer monomer to the mobility of the polymer molecules on the surface, then:

$$\ell_{slip} = \frac{1}{\mathcal{M}}\ell_{mic}\frac{N^3}{N_e^2} \tag{7.14}$$

According to the estimates done by Bruinsma [17], if $\mathcal{M} \ll N_K^{3/2}/N_e$ then slip regimes assumption is valid and the thickness of the foot can be calculated from equation 7.14. We will show later that the thickness of the foot is of the order of ℓ_{slip}. However if $N_K^{3/2}/N_e \ll \mathcal{M} \ll (N_K/\theta_a N_e)^{3/2}$, there exists a new regime that includes the reptation and a local slip flow in the foot. The thickness of the foot in this case is of the order of the radius of gyration of the polymer melt. One must note that the mobility $\mathcal{M}$ can only be measured experimentally and we have not been able to find any data in the available literature for its value.

Now that we have a definition for the slip length, we return our attention to the spreading process. Using the lubrication analysis and applying the velocity slip boundary condition at the wall, the average velocity inside the spreading drop can be written as [16]:

$$\bar{u} = -\frac{dp}{dx}\frac{h}{\eta}\left(\ell_{slip} + \frac{h}{3}\right) \tag{7.15}$$

were p is pressure, and h is the thickness of the drop. Far from the contact line, where $h \gg \ell_{slip}$, we can neglect the effect of the slip and the relation for velocity at the bulk of the spreading drop becomes:

$$\bar{u} = -\frac{1}{\eta}\frac{dp}{dx}\frac{h^2}{3} \tag{7.16}$$

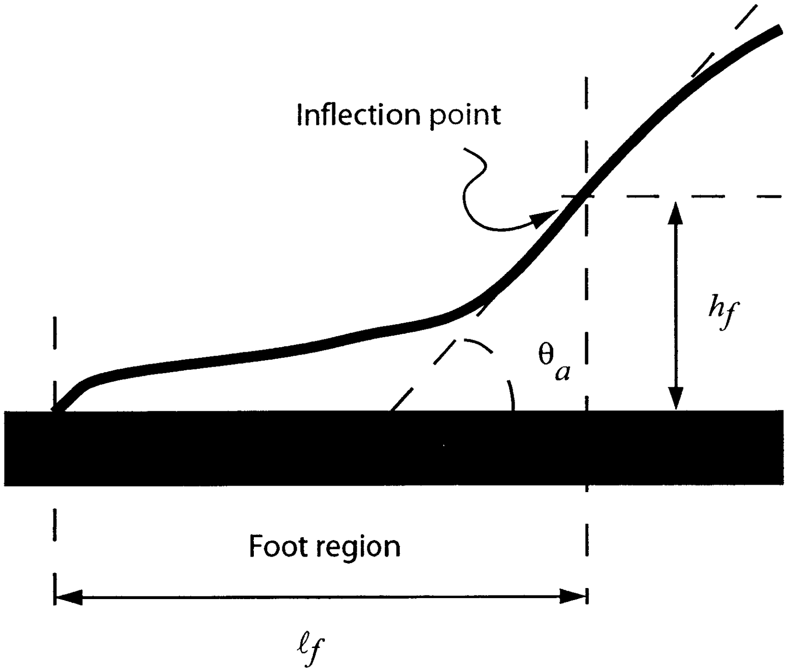

Figure 7-5: The schematic of the important features close to the moving contact line of polymer melts.

If we substitute $p = -\sigma d^2h/dx^2$, then the well-known relation of equation 3.25 will be recovered. The solution to this equation is a spherical cap as mentioned before.

Closer to the moving contact line, the thickness of the drop is much smaller than the slip length ($h \ll \ell_{slip}$). In this case, the average velocity, $\bar{u}$, can be calculated by the following relation:

$$\bar{u} = \frac{\sigma}{\eta}\frac{d^3h}{dx^3}h\ell_{slip} \tag{7.17}$$

One can rewrite equation 7.17 by using $Ca = \eta\bar{u}/\sigma$ as:

$$Ca = \ell_{slip}h\frac{d^3h}{dx^3} \tag{7.18}$$

Solution to equation 7.18 gives the local profile of the drop near the moving contact line. If $X = R - x$ is the distance from the moving contact line, then one obtains:

$$h = \left(\frac{8Ca}{3\ell_{slip}}\right)^{1/2} X^{3/2} \tag{7.19}$$

or in dimensionless form:

$$h/\ell_{slip} = \left(\frac{8Ca}{3}\right)^{1/2} (X/\ell_{slip})^{3/2}. \tag{7.20}$$

This relation shows that in the region where $h \ll \ell_{slip}$, the free surface shape of the spreading drop does not follow the spherical cap shape which is the solution to the macroscopic part of the drop. Therefore there is a new feature close to the moving contact line which is not as thin as the precursor layer but thinner than the slip length which can be as big as tens of microns. This region is called the "foot" [16, 30]. The length of the foot region, ℓ_f, is defined as the distance from the moving contact line to the point where $h = \ell_{slip}$. Thus,

$$\ell_f = \ell_{slip}\left(\frac{3}{8Ca}\right)^{1/3} \tag{7.21}$$

As seen in equation 7.21, ℓ_f is proportional to the slip length, ℓ_{slip}, and it is inversely proportional to $Ca^{1/3}$. Since the slip length increases with the molecular weight of the polymer melts (equation 7.13), therefore the length of the 'foot' region increases for higher molecular weight polymers. Since $\ell_{slip} \sim Z^3$ and $Ca \sim \eta_0 \sim Z^3$, therefore $\ell_f \sim Z^{8/3}$.

7.2.3 Boger fluid

'Boger fluids' are named after David Boger who developed them as a class of model elastic liquids in the late 1970s [13]. These fluids are very important for understanding the effects of elasticity on flow of non-Newtonian fluids [76]. Boger fluids are dilute polymer solutions with a nearly constant shear viscosity, but highly elastic behavior. This is achieved by dissolving high molecular weight polymers into a viscous Newtonian solvent. The viscous Newtonian solvent eliminates shear-thinning effects, whilst the high molecular weight polymers provide the elastic behavior of the solution. The rheological properties of Boger fluids can be approximately described by the elastic dumbbell model [71]. The first Boger fluids were made by dissolving polyacrylamide (PAA) in corn syrup and water mixtures. However, experiments showed that PAA degrades very fast, is polydisperse, and it is a polyelectrolyte which makes the solution very sensitive to the ionic strength of the solvent [3].

Several other Boger fluids have been formulated since 1980. The most commonly used are those based on polystyrene and polyisobutylene. Having linear and uncharged molecules, these systems are resistant to degradation and electrolyte effects. For our experiments, we have used a polystyrene Boger fluid. These are formulated from anionically polymerized, monodisperse high molecular weight polystyrene dissolved in a low molecular weight styrene resin. The characterization of these fluids has been a focus of several recent works in non-Newtonian fluids. A detailed study of shear and extensional rheology and modeling of this fluid can be found in [98, 3].

As noted previously, spreading of Boger fluids are of interest for applications involving elastic fluids in paint and coating industries. However, few published works are available that deal with the spreading of the viscoelastic fluids. Most of these studies are experimental or numerical, and they focus on the effect of fluid elasticity on global evolution and stability of the axisymmetric spreading of fluids during the spin coating process [46, 14]. In these works, the authors found no qualitative differences between the long term dynamic response of the Newtonian and viscoelastic films. This is partly because the fluids studied were dilute polymer solutions and elastic effects are relatively unimportant. However in many applications (for example spin-coating), the solvent is volatile and as the experiment proceeds and the area of the coated film increases, the solvent evaporates and the film becomes increasingly elastic in nature as the concentration increases. These evaporative losses can dominate the spreading at long times and significantly affect the final thickness of profile of the coated film [72].

Work by Spaid & Homsy [108, 109] focused on the drop profile in the vicinity of the moving contact line for viscoelastic fluids. Their numerical simulations were shown the effect of elasticity on the free surface of the drop for both outer and inner regions of drop by performing perturbation theory for the first order effects of elasticity. The effect of fluid viscoelasticity on the local evolution of the shape of the free surface and the stability of this motion is shown; however no experimental measurements of the free surface profiles for viscoelastic fluids at the vicinity of the contact line exists.

In the following section, we will present results on the spreading of highly entangled polymer melts and Boger fluid on a solid surface. The characteristics of the free surface especially in the vicinity of the moving contact line is investigated. These results are compared with available theoretical predictions.

7.3 Results and discussion

The geometry of the spreading experiments in this chapter are the same as the geometry is explained in chapters 3 and 4. We have used the psLFI microscope as the measurement system. The working fluids are high molecular weight silicone oils which serve as entangled polymer melts ($10 < Z < 35$) and a polystyrene Boger fluid denoted PS025. It was shown earlier in this chapter that the silicone oils are highly entangled polymer melts. The PS025 is a polystyrene based Boger fluid that has 0.25 wt% of high molecular weight polystyrene dissolved in a low molecular weight styrene resin. The preparation of PS025 is explained in detail by [3].

These fluids are deposited on a previously cleaned silicon wafer (same as those used for experiments in chapter 3) by using a needle tip. Due to the high viscosity of these fluids, the force required to push the fluids through the needles were so high that our syringe pump could not provide it. The volume of the drop can be adjusted by using a smaller or larger needle tip. The drop volume is measured by taking a picture of the drop before depositing it on the surface. The silicon wafer was placed on a XY translation stage. After the drop was deposited on the surface, the free surface profile of the spreading drop was scanned repeatedly as it spread by utilizing the XY stage and psLFI system. Using this method we were able to measure the evolution of the drop thickness and its radius, simultaneously.

7.3.1 Highly entangled polymer melts

To identify the microscopic features at the vicinity of the highly entangled polymer melts ($Z > 10$) (for simplicity from here on they are called *polymer melts*), we have defined the expected features on the schematic of the spreading fluid in figure 7-5. In the presence of the 'foot' region at the moving contact line, the distance between the point where the moving front is located by the psLFI system and the inflection point at the free surface of the fluid (located by numerical differentiation of the measured

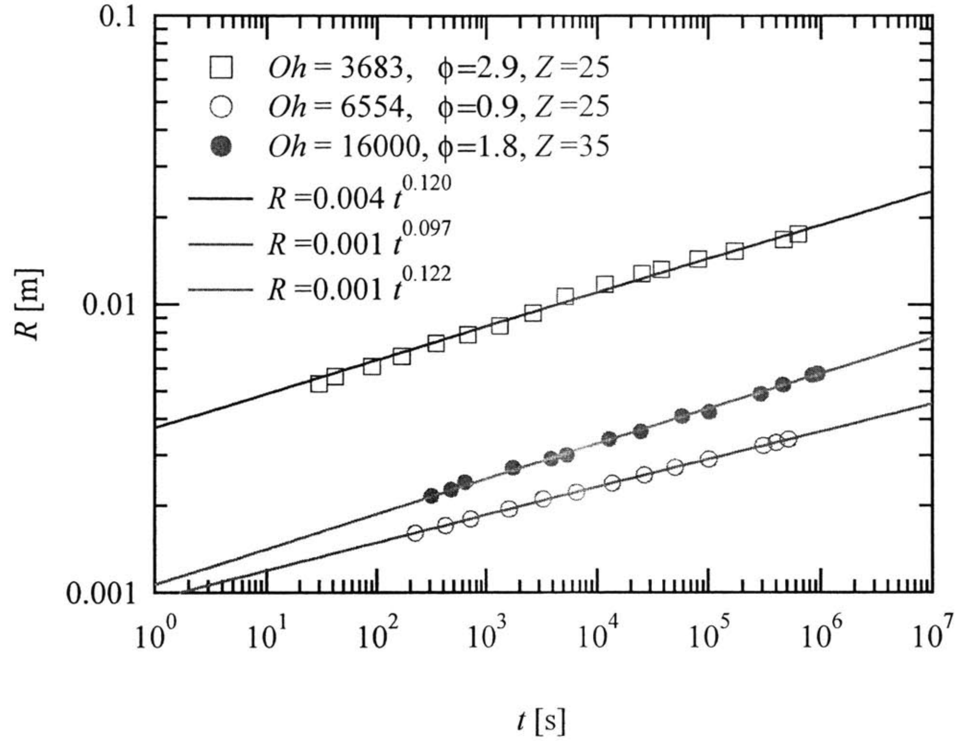

Figure 7-6: The radius of polymer melt drop, R, as a function of time, t, for different sizes and viscosity of polymer drop.

profile; see chapter 3) is called ℓ_f. The thickness of the drop at the inflection point is called h_f as shown in figure 7-5.

We used four different polymer melts with viscosities ranging from 300 Pa s $<$ η_0 $<$ 2500 Pa s. The rheological properties of these fluids are given in appendix A. The velocity of the contact line, $\dot{R}$, is measured by observing the radius of the drop as a function of time and using a power-law regression and differentiating this expression with respect to time. It is important to note that in the case of polymer melts, we consider the radius of the drop as the distance from the center of the spreading drop to the measured inflection point. The results for the radius of the polymer drops as a function of time, for different drop sizes (different ϕ) and different viscosity (different Z) are shown in figure 7-6. For large drops $\phi > 1$, the effect of capillarity is negligible and the spreading of the drop is driven by the gravitational force and resisted by the viscous force. As noted in chapter 3, the resulting power-

Table 7.1: Power-laws for viscous-capillary and gravity current spreading droplet of polymer melts on smooth solid surface. Comparison between the analytical spreading results and the experimental spreading results.

Z	Oh	ϕ	Analytical result	Experimental result
25	3683	2.9	$A = 3.97$, $n = 1/8$	$A = 3.82$, $n = 0.121$
25	6554	0.9	$A = 1.24$, $n = 1/10$	$A = 0.91$, $n = 0.097$
35	16000	1.8	$A = 2.30$, $n = 1/8$	$A = 1.31$, $n = 0.122$

law for Newtonian drops with $\phi > 1$ are $R \sim t^{1/8}$. Also for small drops, $\phi < 1$, the radius has the familiar power-law relation of $R \sim t^{1/10}$ since the gravitational force is negligible. It is noteworthy that since we choose to define the radius in such way to neglect the foot region, we eliminated the effect of the entanglement in the spreading and as a result, the spreading of the drops have the same relations as for the drop of Newtonian fluids. The calculated velocity will be used in the calculation of the capillary number, $Ca = \eta_0\dot{R}/\sigma$. We can also show these power-laws in the dimensionless form of $R^* \sim At^{*n}$ where for gravity current:

$$R^* = \frac{R}{\ell_{cap}}, \quad t^* = \frac{t}{\mu/\rho g\ell_{cap}}, \quad A \simeq \pi^{3/8}\phi^{9/8}, \quad n = 1/8 \tag{7.22}$$

and for capillary-viscous:

$$R^* = \frac{R}{\ell_{cap}}, \quad t^* = \frac{t}{\mu\ell_{cap/\sigma}}, \quad A \simeq \pi^{3/10}\phi^{9/10}, \quad n = 1/10 \tag{7.23}$$

The results for these constants from theory (chapter 3, table 3.2) and experiments is given in the table 7.1

After careful measurement of the free surface of the polymer melt drops close to the moving contact line, we were able to detect a feature which was similar to the precursor layer (chapter 4) but much thicker than the precursor layer ($\sim 10\mu$m rather than 100nm). In figure 7-7(a), a profile of a spreading drop ($Z = 25$) on a silicon wafer is shown. The left vertical axis is the thickness of the drop h in micrometers. The right vertical axis is the fringe visibility, m, of the drop during the measurement using psLFI microscope. As shown, the value of m decreases

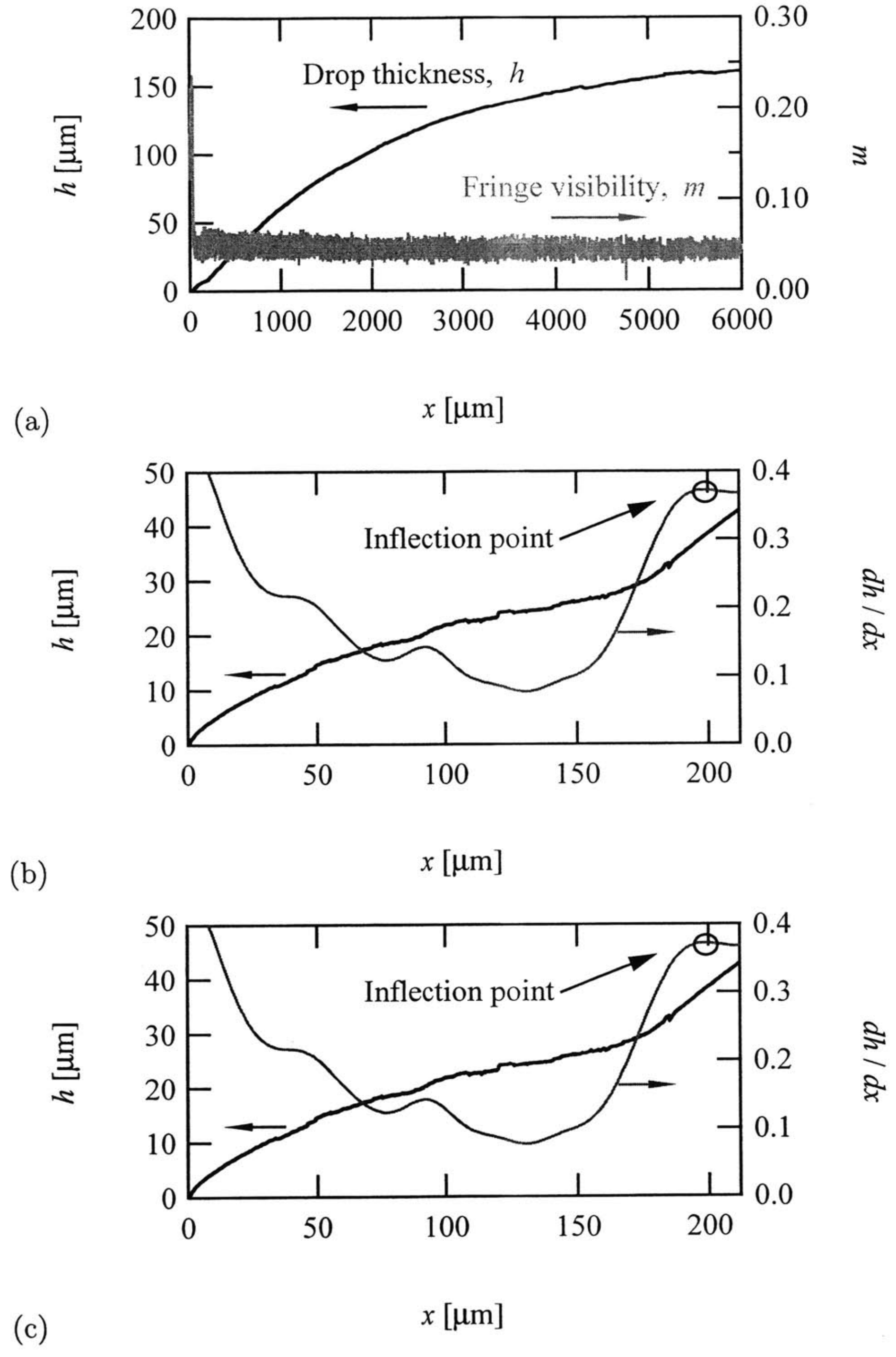

Figure 7-7: (a) The profile of a drop of polymer melt ($Z = 25$, $Ca = 1.3 \times 10^{-3}$, $\phi = 1.2$) and the fringe visibility, m, as it is measured from the moving contact line to the center of the drop. The profile of a polymer melt drop at the vicinity of the contact line, (b), for the same drop and (c) $Ca = 1.01 \times 10^{-3}$, $\phi = 1.8$, $Z = 35$. The thin line shows the numerical differentiation of the free surface profile.

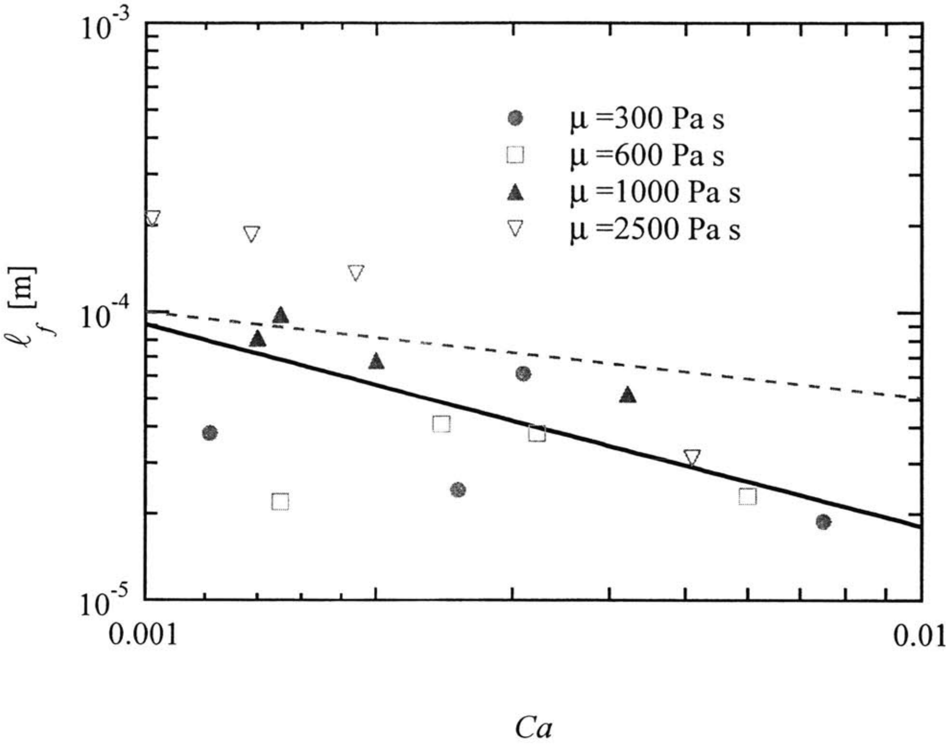

Figure 7-8: The length of the foot region as a function of the capillary number. The experimental data is shown by (•). The best regression fit (solid line) to this data is $\ell_f = 7.2 \times 10^{-0.7} Ca^{-0.7}$. The theoretical prediction (Dashed line) by [16] gives $\ell_f \sim Ca^{-1/3}$.

rapidly at the point that the drop is first detected. In contrast to spreading of unentangled polymers ($Z < 1$, cf. chapter 4), no precursor film was seen for this system. However, a new feature is present very close to the moving contact line. In figure 7-7(b-c), we present examples of these features in an enlarged region close to the contact line that, following [16], we call the 'foot'. The thin line is the numerical differentiation of the free surface profile (dh/dx). The length of the foot, ℓ_f, is the distance from the point the fluid is detected and the inflection point at the free surface of the drop (location of the maximum slope of the free surface).

To compare these results with the theoretical prediction, we plot the length of the foot ℓ_f as a function of capillary number in figure 7-8. According to equation 7.21, the length of the foot has a power-law relation with the capillary number ($\ell_f \sim Ca^{-1/3}$).

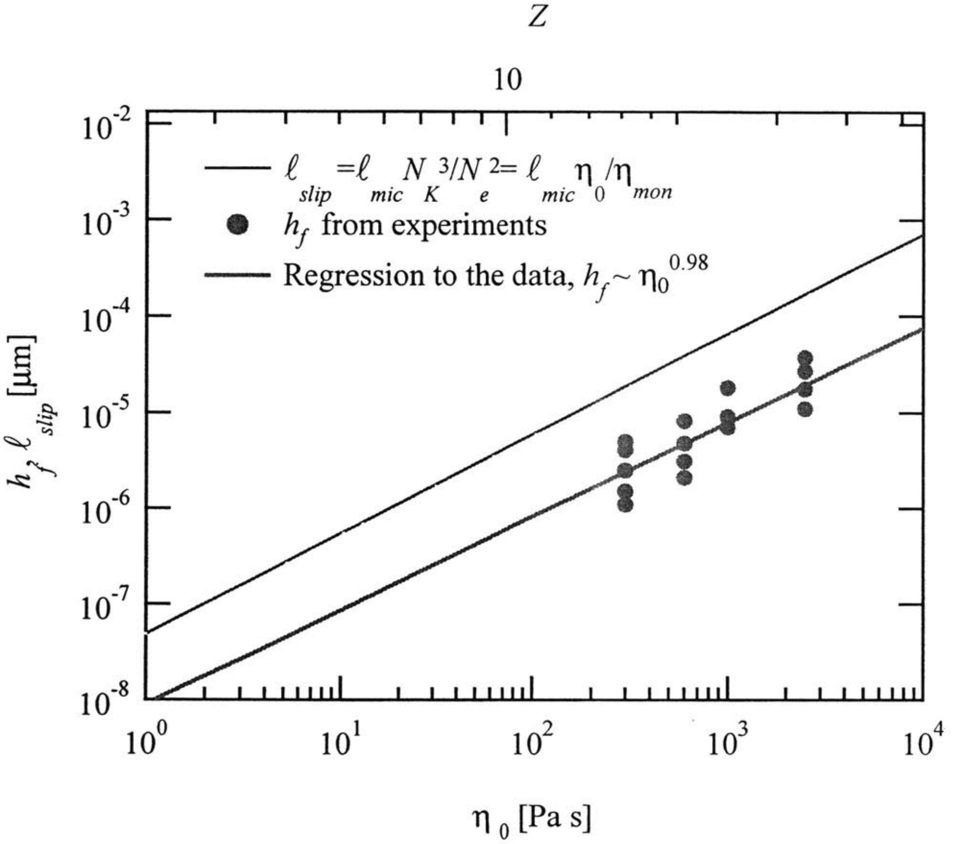

Figure 7-9: The maximum thickness of the foot, h_f, as a function of the viscosity of the polymer melt,η. The theoretical prediction of the slip length, ℓ_{slip}, is presented by the thin solid line. The thick solid line is the best fit to the experimental data. The top axis is the number of entanglements, Z.

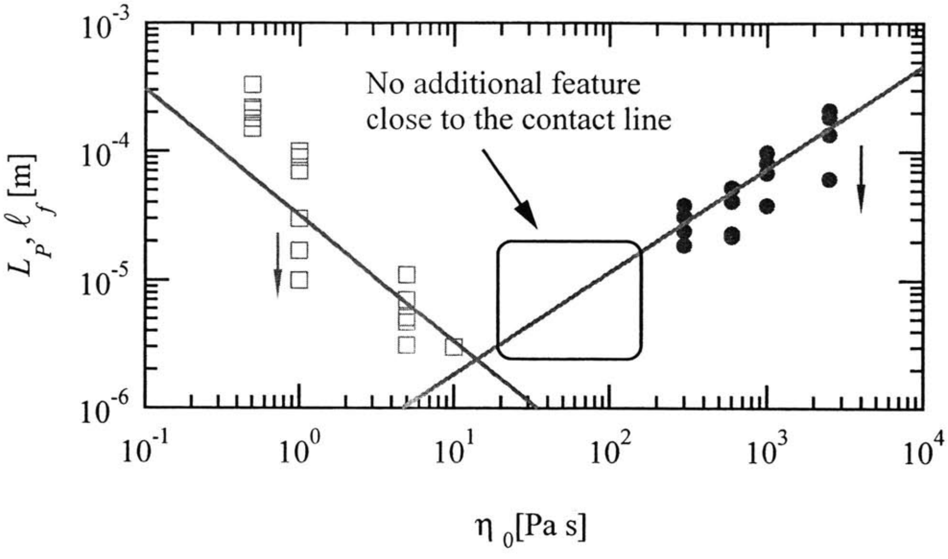

Figure 7-10: The comparison of the length of the foot region, ℓ_f, and the length of the precursor layer, L_P, (from chapter 4) as a function of the viscosity, η_0. The arrows indicate the direction of increasing Ca (or decreasing time).

The thick line in this figure is the best regression fit to the experimental data (●) which shows a relation as $\ell_f = 1180\ell_{mic}Ca^{-0.7}$ where ℓ_{mic} is the microscopic length scale of the fluid as defined in equation 3.49. The thin dashed line is the predicted relation (equation 7.21) for polymer melts. As shown, the length of the foot decreases when capillary number increases, but the power-law is much faster than the one predicted by the theory.

In figure 7-9, the measured thickness of the drop at the inflection point, h_f, as a function of viscosity is presented. According to the theory (equation 7.15), the cross over from the foot region to the macroscopic spherical cap happens at the thickness which is in the order of the slip length of the polymer melt, ℓ_{slip}. In order to examine this prediction, we have also plotted the calculated slip length from equation 7.13 as a thin solid line in this graph. According to the equation 7.13, the slip length is a linear function of the viscosity of the polymer melt as $\ell_{slip} = \ell_{mic}\eta_0/\eta_{mon}$ where $\eta_{mon} = 0.001$ Pa s for PDMS. Along the top abscissa, the number of entanglements Z is also presented for these fluids. By fitting a power-law function to these data point, the best fit was found to be $h_f = 16.23\ell_{mic}\eta^{0.98}$. To employ the modification to equation 7.13 which is equation 7.14, we have used the front factor of the fitted function and the theoretical results to calculate the mobility relation from the offset in the data. The condition for the validity of Brochard & de Gennes theory is $\mathcal{M} \ll Z^{3/2}N_e^{1/2}$ according to Bruinsma [17]. The range of this parameter for these fluids is $378 < Z^{3/2}N_e^{1/2} < 1255$. From our experiments, by dividing the ℓ_{slip} relation form the theory to the fitted function for h_f, we found $\mathcal{M}= 7.5$. Validity of the condition of the slip regime [17] is confirmed since $\mathcal{M}\ll Z^{3/2}N_e^{1/2}$ for these polymer melts.

Finally to review the length of the structure for highly entangled polymer melts and non-entangled polymer melts, they are presented together in figure 7-10 as a function of the viscosity of the fluid, η_0. For unentangled polymer melts (low viscosity, $\eta_0 < 1$Pa s), which are represented by the rectangles in this figure, the length of the the structure close to the moving contact line (precursor layer), L_P, is inversely proportional to the viscosity as shown in chapter 4 since $L_P \sim Ca^{-1}$. The length of the foot, ℓ_f, for the highly entangled polymer melts, which are shown by the solid circles, increases when the viscosity of the fluid increases $\ell_f \sim \eta^{-0.7}$.

The gap between these data sets are due to the fact that for the intermediate viscosities, the length of adiabatic precursor films, if it exists, are smaller than the lateral resolution of our optical system and it is not detectable with our optical system ($\sim 10^{-6}$m). As shown before, the foot structure for polymer melts only appears for highly entangled polymers ($Z > 10$). For fluids with $Z < 10$, the molecules of the intermediate viscosity fluids are not highly entangled to generate the foot (figure7-3). The cross over point between the solid lines (fit to the experimental data) moves as times increases. This is due to the different functionality of these length with time. As shown in chapter 4, the length of the precursor film is inversely proportional to Ca. Therefore $L_P \sim U^{-1} \sim t^{0.9}$.

7.3.2 Boger fluid

In the previous section, the effect of entanglement of molecules on microscopic structures at the moving contact line was investigated. In this section, we present the characteristics of the spreading of Boger fluids on a silicon wafer substrate. An important note about this ideal elastic dilute polymer solution (PS025) is that it partially wets the silicon surface. Therefore unlike silicone oils, for which the equilibrium contact angle θ_e is equal to zero, there exists a non-zero equilibrium contact angle. Existence of a non-zero equilibrium contact angle affects the microscopic features of spreading [69]. In chapter 4, it was noted that precursor films are only present for fluids that wet the surface completely ($S \gg \sigma\theta_a$). This affects the universal spreading law (the HVT law) as this relation is also for the perfectly wetting fluids. A modification to this law is needed for fluids with a finite equilibrium contact angle. More on this subject will be discussed in the results section. Previous published work on these solutions [74] have shown a different behavior compared to the HVT law 3.31.

To investigate the effect of viscoelasticity on the spreading phenomena, the first logical step is to run a bench mark experiment on a Newtonian fluid (non-viscoelastic) with very similar physical properties to the Boger fluid as a reference for our experiment. The ideal fluid is the oligomeric styrene which is used as a solvent to formulate the PS025 Boger fluid. The value of viscosity of oligomer oil is 46 Pa s. However, it is weakly elastic ($\lambda_{PS} \approx 2.5 \times 10^{-4}$ s) due to the lack of the large molecules of polystyrene.

To measure the surface tension of the oligomer oil and the ideal elastic dilute solution (PS025), we have performed a tensiometry test using a Wilhelmy Platinum plate on our tensiometer (Krüss, K10). The plate is lowered to touch the fluid surface and the force exerted by the fluid on the plate is measured as a function of time. This force is converted to the surface tension and it is measured for PS025 and the oligomer oil of these fluids as a function of time. This is because the fluid meniscus takes a long time to evolve to its equilibrium configuration and reaches it static form. After a long time the surface tension stay constant and it is the equilibrium surface tension that is used through out this research.

The result of this experiment is presented in figure 7-11. The solid line is an exponential fit to the oligomer oil result and the dashed line is an exponential fit to PS025 result. The resulting equations for the regression to the data are :

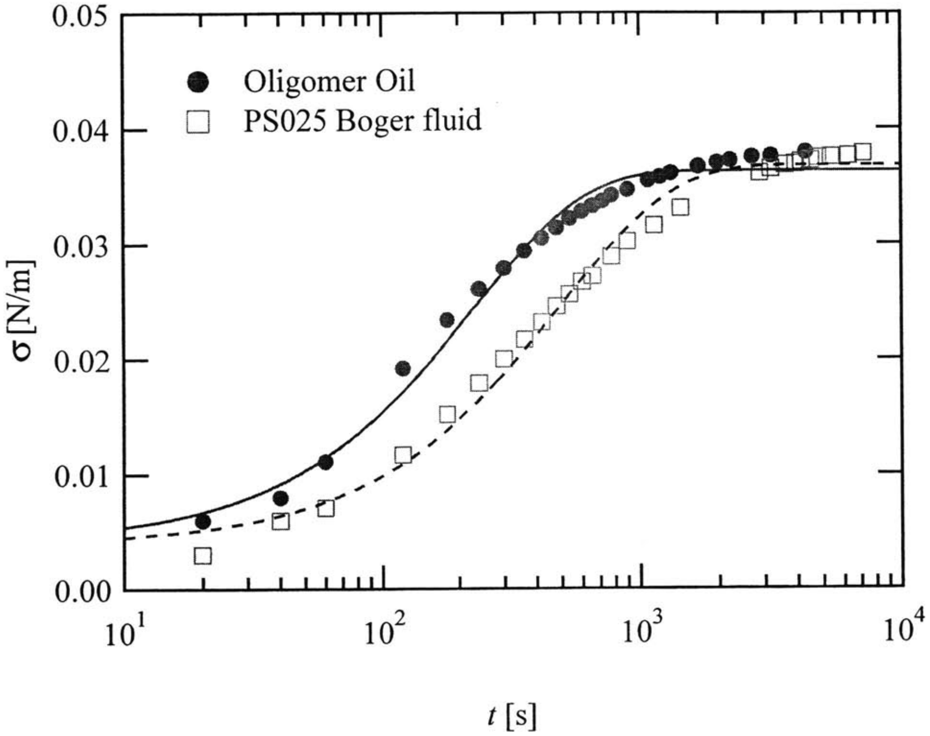

Figure 7-11: Evolution of the measured surface tension of PS025 Boger fluid (□) and the oligomer oil (•) as a function of time when it is measured using a Wilhelmy plate tensiometer.

$$\sigma_{Oligomer} = 0.036 - 0.031exp(-t/263) \qquad (7.24)$$

$$\sigma_{Boger} = 0.036 - 0.031exp(-t/555) \qquad (7.25)$$

The characteristic time to approach steady state are found from these exponential fits are 263 s for the oligomer oil and 555 s for PS025 Boger fluids. This means it takes almost twice as long for PS025 to approach the steady state value of surface tension as for the oligomer oil. This difference on the characteristic time in wetting the Wilhelmy plate can possibly be the source of generation of the thin film in front of the moving contact line of PS025 Boger fluid as we will discuss later in this chapter.

Two drops of the oligomer oil were deposited on the silicon surface and the evolution of their radius as a function of time were recorded. As noted in chapter 3, the effect of drop size on the spreading of a viscous drop is very important, therefore a range of drop volumes were chosen. The characteristic drop size for these drops are $\phi = 0.65$ and 2.3. The capillary length of this fluid is $\ell_{cap} = \sqrt{\sigma/\rho g} = 1.9$ mm. In figure 7-13, the evolution of the radius of these drops as a function of time is presented. The best fit for the data of the largest drop ($\phi = 2.3$), shows that this drop is in the gravity current region of the spreading diagram (figure 3-2) and as expected the power-law relation of this drop is $R = 3 \times 10^{-3} t^{0.128}$. For the other drop, the power-law is $R = 10^{-3} t^{0.1}$ as expected since this drop is small and are in the spherical cap region of spreading diagram. Using the dimensionless forms for R and t used in equations 7.23 and 7.22:

$$R^* = 3.05 t^{*0.128} \qquad (7.26)$$

$$R^* = 1.05 t^{*0.10} \qquad (7.27)$$

These regressions (solid lines) are carried out for the data of the earlier stages ($t <$ 5000s) of spreading.

Since the oligomer is not a perfectly wetting fluid on the silicon surface, the drops stopped spreading at the time they reach their ultimate equilibrium contact angle. This deviation from the power-laws in the spreading process are also shown in the

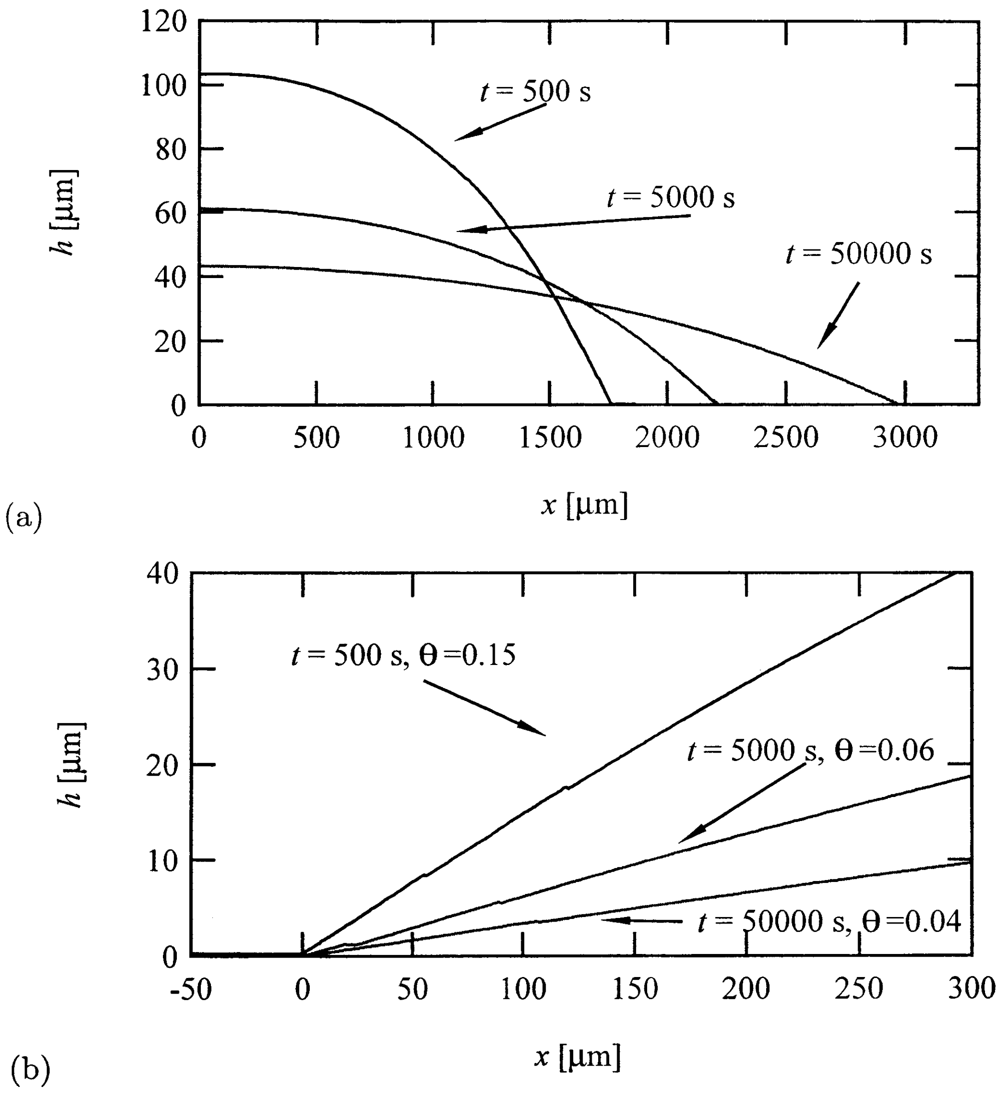

Figure 7-12: (a)The evolution of the free surface (h) of a spreading droplet of oligomer styrene oil, $\phi = 0.65$, on silicon substrate at t = 500, 5000, and 50000 s. (b) The same profiles are shown very close to the contact line to the contact angle comparison. The contact angle decreases with time as expected. No precursor film is observed.

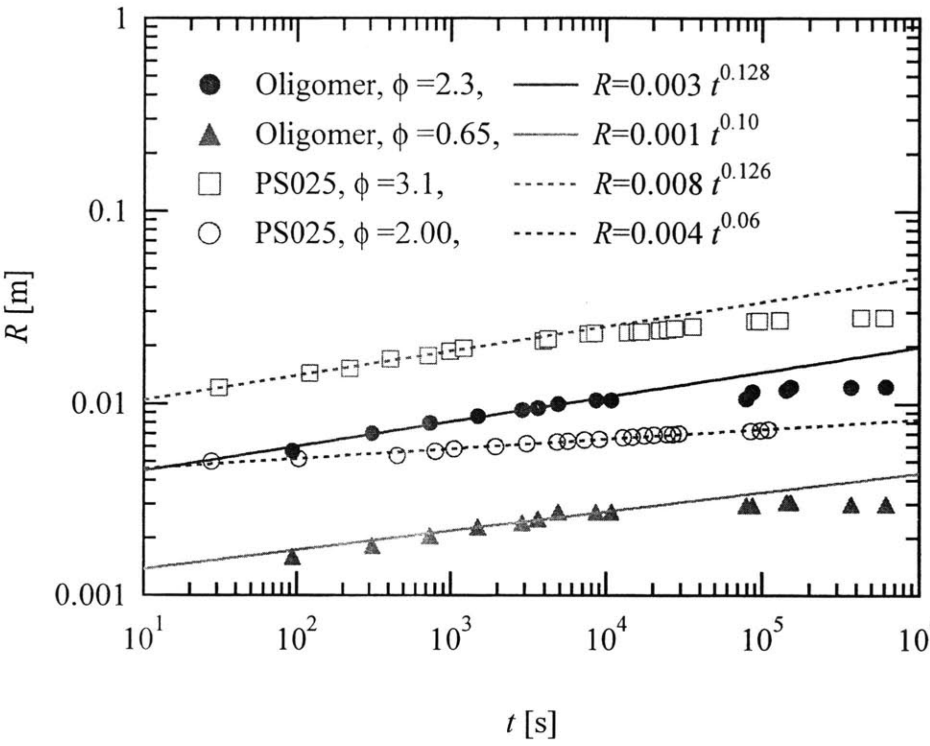

Figure 7-13: The spreading of the oligomeric styrene and PS025 Boger fluid on silicon surface. The solid symbols represent the oligomer and the hollow symbols represent PS025 Boger fluid. The lines are best fit to the early time data before equilibrium approached for the oligomer (solid lines) and PS025 (dashed line). Spreading stops after the drops reach their equilibrium contact angle.

figure 7-13. For small drops with the spherical cap shape, we showed in equation 3.32 that $\Omega \cong \pi R^3 \theta_a / 4$. Thus, for fluids with an equilibrium contact angle , a minimum volume is required that leads to $\theta_a > \theta_e$. Therefore there is a limitation for the volume (or ϕ) for these drops to spread on the surface.

The evolution of a drop of oligomer is shown in figure 7-12. The global evolution of the drop is shown in figure 7-12(a) as a function of time. The thickness of the drop decreases and its radius increases with time (as it is shown in figure 7-13 as well). In figure 7-12(b), these profiles are replotted by setting the coordinate origin ($x = 0$) at the moving contact line. As seen in this figure, the dynamic contact angle decreases with time as is expected from previous discussions. Also no precursor film is observable in front of the moving contact line. This is due to the fact that the oligomer is not a perfectly wetting fluid on a silicon surface. It was indicated before that an important condition for existence of the precursor film is a perfectly wetting fluids [30].

To further investigate the evolution of the dynamic contact angle of the spreading of the oligomer of silicon surface, we have plotted the measured contact angles of the drop as a function of capillary number in figure 7-14(a). These measurements are compared with the HVT law which is presented with a solid line in this figure. As it is shown, for low capillary numbers, the dynamic contact angle, θ_a, deviates from the HVT prediction (for a perfectly wetting fluid, $\theta_e = 0$) and becomes almost constant approaching $\theta_e \approx 0.04$rad. For the spreading of fluids with non-zero equilibrium contact angle, the following modifications to HVT law have been suggested [69]:

$$\theta_a^3 - \theta_e^3 = K_1 Ca \tag{7.28}$$

$$\theta_a(\theta_a^2 - \theta_e^2) = K_2 Ca \tag{7.29}$$

where K_1 and K_2 are constants depend on the slip length [69]. We have plotted our results using both of these relations in figure 7-14(b). The regression to the the data for equation 7.28, gives $K_1 = 11.6 \pm 0.3$ with the confidence level of $R^2 = 0.999$. The regression to the data for equation 7.29, gives $K_2 = 13.2 \pm 5.4$ with the confidence level of $R^2 = 0.997$. Due to the small equilibrium contact angle for the oligomer, $\theta_e \approx 0.04$ rad, the difference between these models are negligible.

From the spreading experiments of the oligomer, we confirmed that the behavior of these fluids is like the low viscosity silicone oils as they follow the spreading regimes depend on the size of the drop (ϕ). When fluid is not perfectly wet the surface, evolution of the dynamic contact angle does not follow the conventional HVT law. However in figure 7-14, we showed that using the modified versions of HVT law (equations 7.28 and 7.29) this behavior can be captured as well.

Now that we have quantified the behavior of the oligomer oil, the spreading results of PS025 Boger fluid are presented. The drops of PS025 Boger fluid were deposited

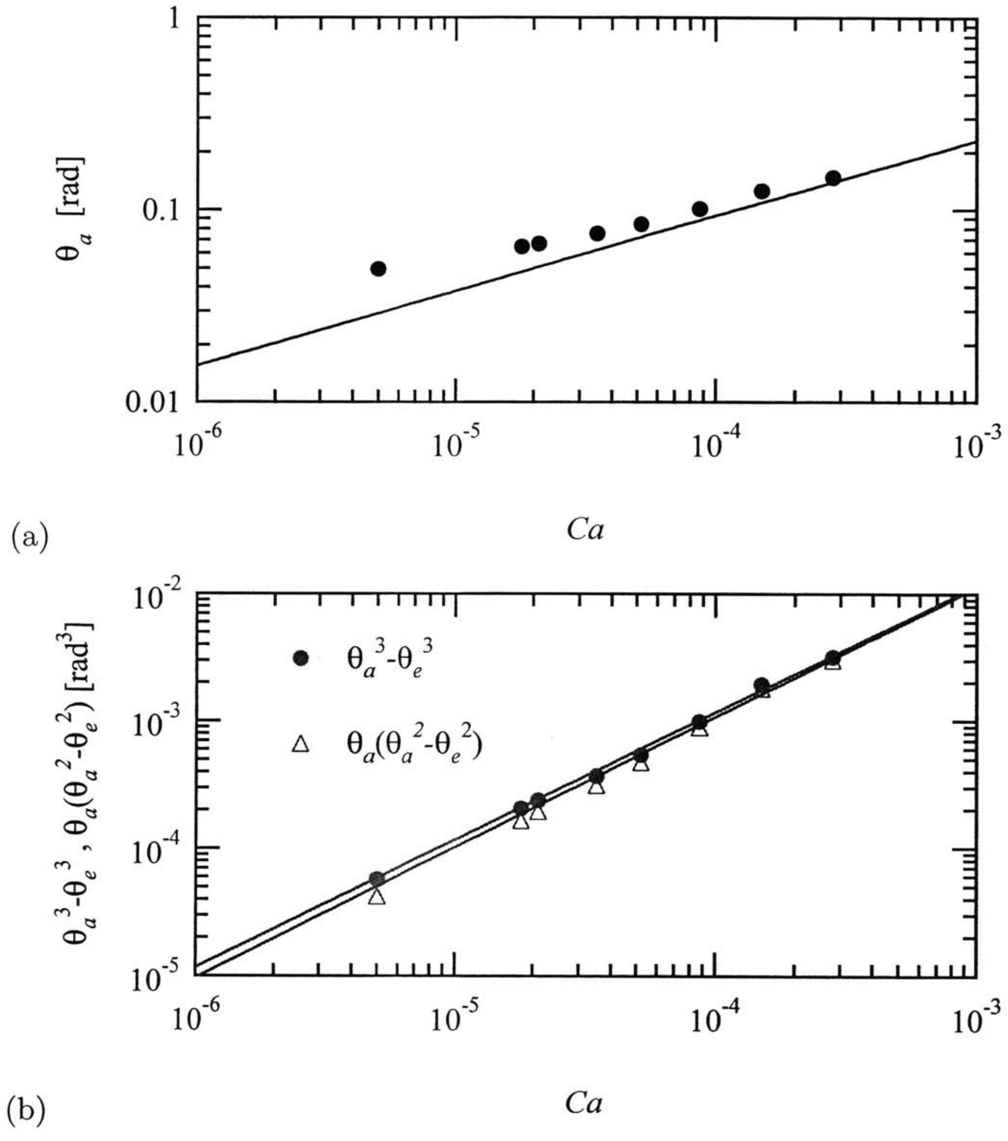

Figure 7-14: (a) The measured dynamic contact angle, θ_a, shown by (•) as a function of capillary number. The solid line is the HVT law for the comparison. (b) represents the same data by using $\theta_a^3 - \theta_e^3$ (•) and $\theta_a(\theta_a^2 - \theta_e^2)$ (△) as suggested by [69]. The solid lines are the best regression fit to the data.

on a clean silicon wafer and the evolution of their radius and thickness as a function of time is measured. In figure 7-13 the spreading of PS025 with different sizes of $\phi = 2.0$ (○), and $\phi = 3.1$ (□) are shown. The smaller drop spreads much slower than the drop of similar size of oligomer fluid. A regression fit (dashed line) to the data gives $R \sim t^{0.06}$ which is slower than the power-law for Newtonian fluids of the same size. The larger drop however, spreads at a faster rate in earlier stage of spreading, $R \sim t^{0.126}$, but the rate of spreading soon decreases and the drop spreads at a slower pace. Both of these drops stop after their contact angle reach the equilibrium value in the same way as the oligomer oil. It is important to notice that PS025 Boger fluid is not a perfectly wetting fluid on silicon surface as well and when it reaches a non-zero equilibrium contact angle, the spreading process stops.

The effect of capillary number on spreading of PS025 Boger fluid is shown in figure 7-15(a). The symbols represent experimental measurements of the dynamic contact angle, θ_a, as the drop of a PS025 Boger fluid ($\phi = 2.1$) spread on a silicon surface. The solid line represent the HVT law. The values of the measured contact angles are less than the values predicted by HVT law for higher capillary numbers but as the drop spreads and the capillary number decreases, the contact angle approaches a constant value of $\theta_e = 0.057$, asymptotically. Once again we have used the modification to the HVT law from equations 7.28(●) and 7.29 (△) to further analyze this behavior in figure 7-15(b). The solid lines are regression fits that give $\theta_a^3 - \theta_e^3 = 34Ca^{1.1}$ with the confidence level of $R^2 = 0.988$ and $\theta_a(\theta_a^2 - \theta_e^2) = 90Ca^{1.2}$ with the confidence level of $R^2 = 0.985$. These results are similar to those of oligomer fluid however the front factor and the power are larger than the oligomer fluid. This can be due to different values of exponents for PS025 and oligomer oil.

To further investigate the dynamic contact angle of PS025 Boger fluid, the region close to the moving contact line is shown in figure 7-16(a). The profiles of the drop during the spreading process are plotted in this figure. The last profile is the static shape of the drop after it reaches the equilibrium shape. As seen in this figure, at the earlier stages of spreading, there exists a film of liquid that spreads in front of the macroscopic profile of the drop. This observation is somehow unexpected since the

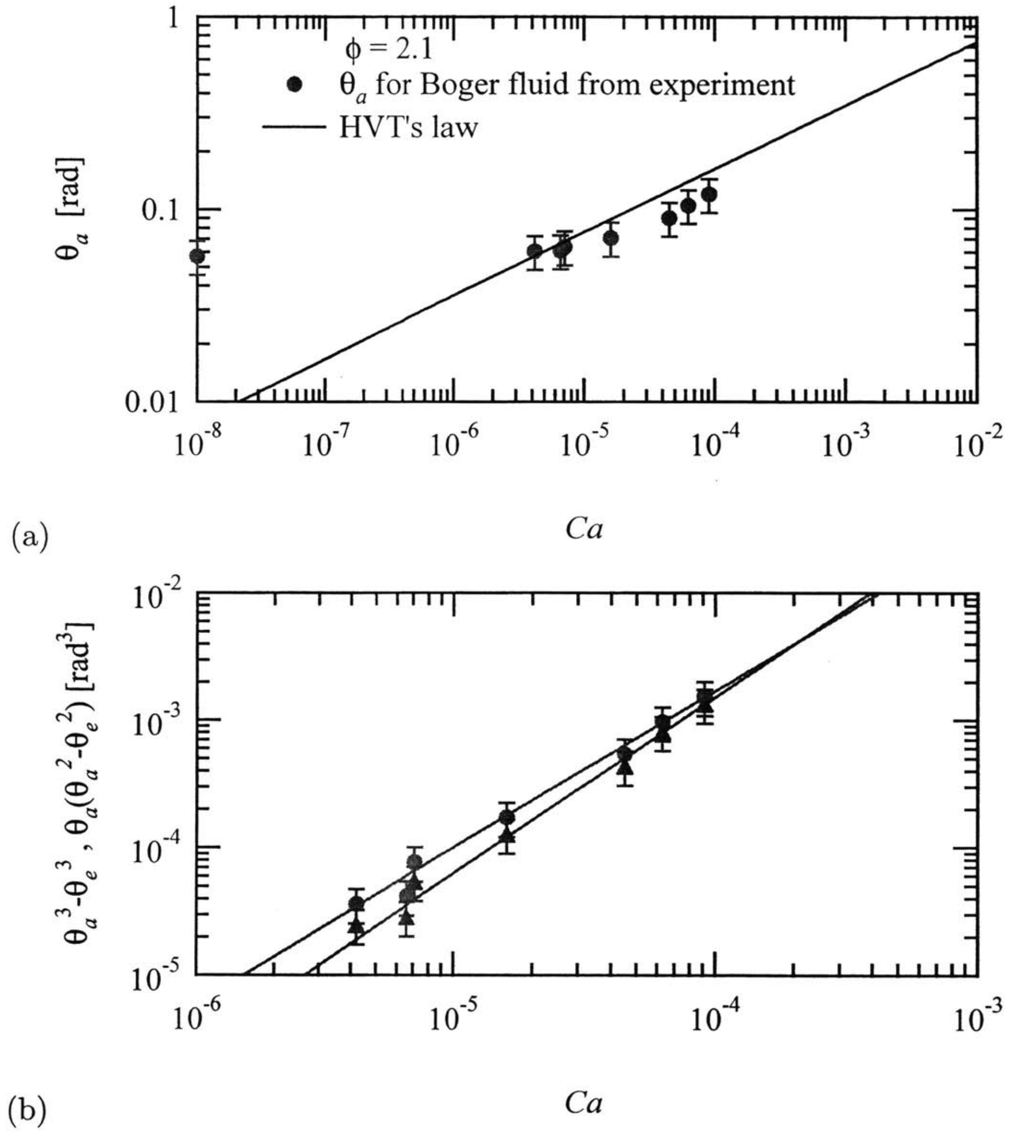

Figure 7-15: (a) The measured dynamic contact angle, θ_a, shown by (•) as a function of capillary number for PS025 Boger fluid. The solid line is the HVT law for the comparison. (b) The same data by using $\theta_a^3 - \theta_e^3$ (•) and $\theta_a(\theta_a^2 - \theta_e^2)$ (△) as suggested by [69]. The solid lines are the best regression fit to the data.

existence of this film is not predicted by theory. This film can not be the precursor film because PS025 Boger fluid does not perfectly wet the silicon surface and thus is not expected to produce a precursor film. Also the thickness of this film ($\sim 5\mu$m) is much larger than a typical precursor film ($\sim$ 100 nm) as shown in chapter 4. The PS025 Boger fluid is a dilute polymer solution and the effect of entanglement, which is important for highly entangled polymer melts, to generate the "foot" in front of the moving contact line does not apply to this problem.

As it is shown in figure 7-16(b), the length of this foot-like film is decreasing when capillary number decreasing. To see this relation clearer, the length ℓ_f and the thickness h_f of this film is plotted as a function of capillary number in figure 7-17. The length of this film is the distance from the inflection point at the drop to the moving contact line (the point that the fringe visibility m drops rapidly) which is the same method that was used for the highly entangled polymer melts. The thickness of this film h_f is the average thickness of the film along its length. The average thickness of the film is approximately constant for all of the capillary numbers while its length decreases as capillary number decreases.

Since PS025 Boger fluid is a viscoelastic fluid, another possible source of this feature can be the effect of viscoelasticity close to the contact line. To characterize this effect, we define the following parameters:

$$De = \frac{\lambda}{t_{spread}} = \frac{\lambda \dot{R}}{R} \tag{7.30}$$

$$Wi = \frac{\lambda \dot{R}}{h_f} \tag{7.31}$$

where De is the Deborah number which is the ratio of the longest relaxation time of the fluid λ to the characteristic time scale of the flow along the radius of the drop, which is $R/\dot{R}$. The Weissenberg number, Wi, is defined as the relaxation time multiplied by a characteristic shear rate of the flow. In the film the shear rate is $\dot{R}/h_f$ for shear flow where $\dot{R}$ is the average velocity of the moving front. The Deborah number and Weissenberg number are dimensionless parameters that can be used to identify the effect of viscoelasticity in the flow. If $De \to 0$ the effects of viscoelasticity

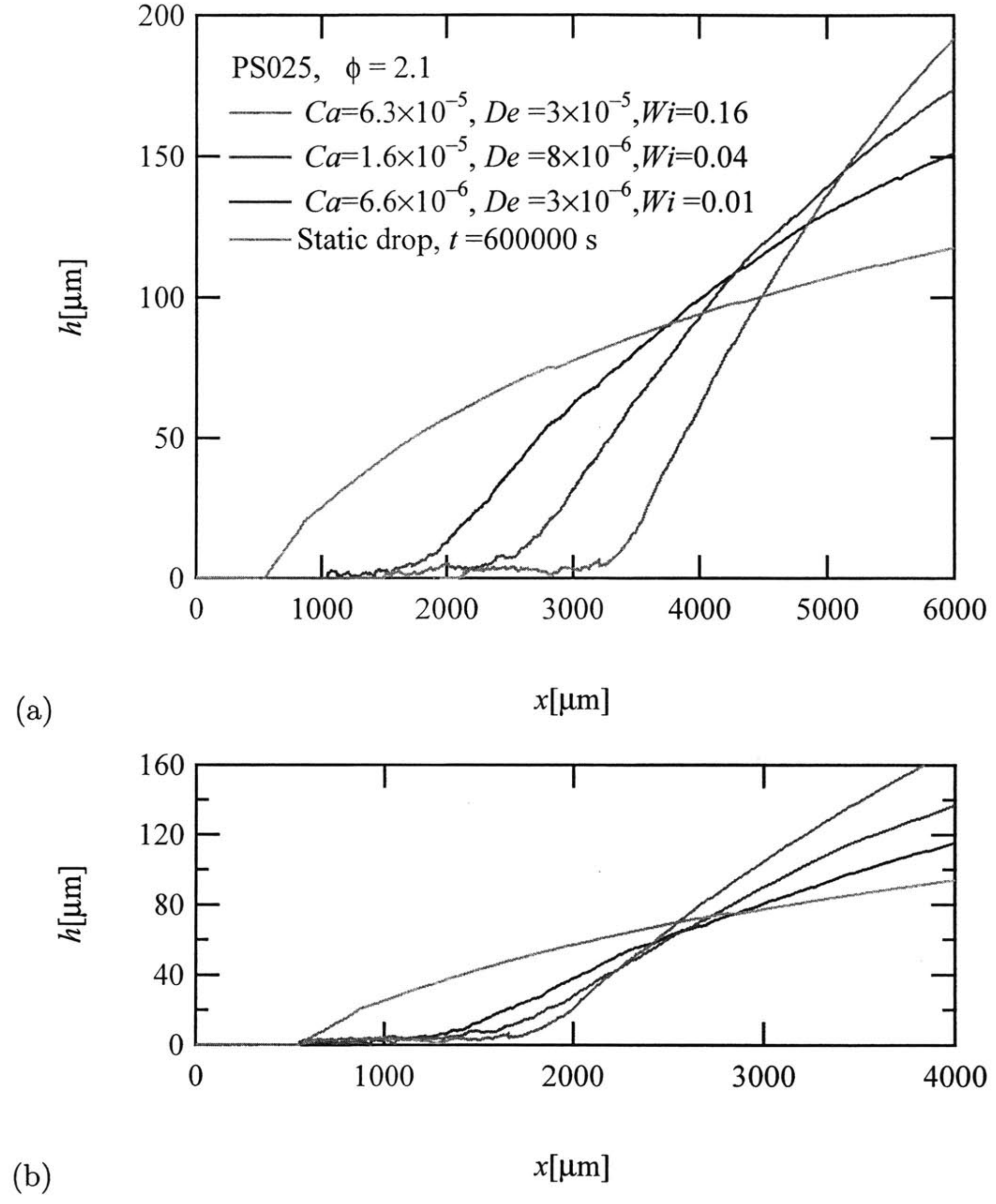

Figure 7-16: The evolution of the free surface of PS025 Boger fluid at the vicinity of the moving contact line (a) at their original position (b) when shifted to the same origin. The values of capillary number, Deborah number, and Weissenberg number is given for each profile. A thin film of fluid can be observed ahead of the macroscopic moving fronts.

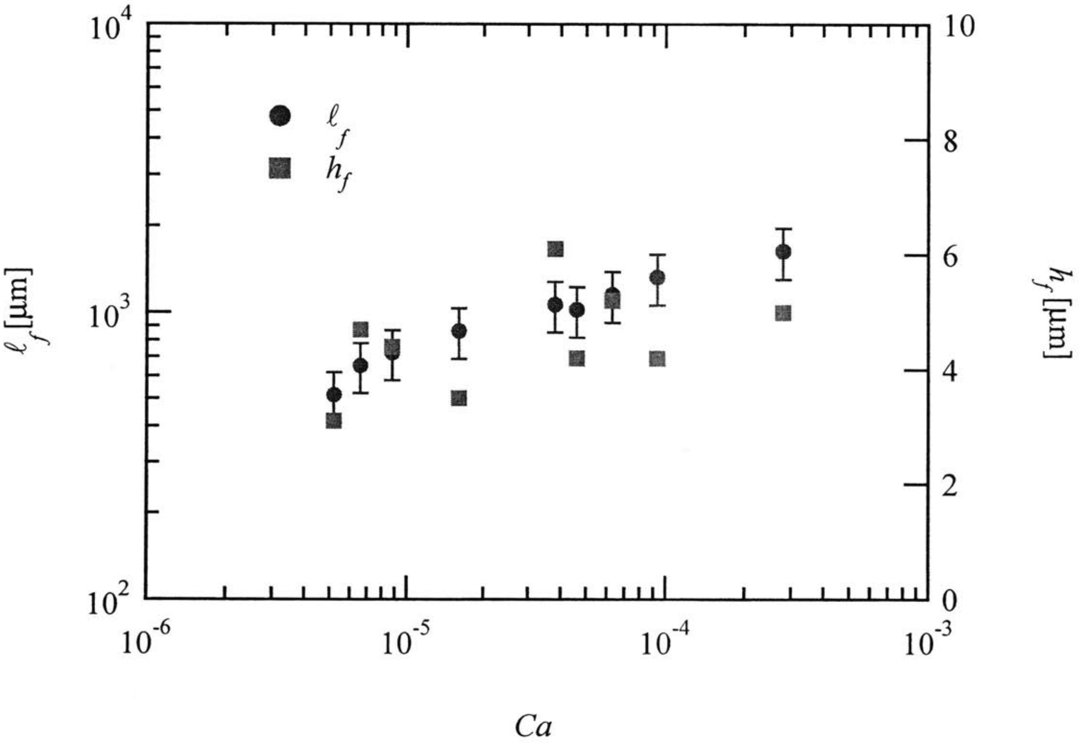

Figure 7-17: Length ℓ_f (•) and thickness h_f (□) of the foot-like feature for PS025 Boger fluids as a function of capillary number.

at extensional flows are negligible and if $Wi \to 0$, the effect of viscoelasticity in shear flow is negligible and the fluid behaves like a Newtonian fluid. If $De \sim O(1)$ or $Wi \sim O(1)$, the non-Newtonian effects become important. Using the available data for PS025 ($\lambda = 4$ s) from [98], Deborah number and Wissenberg number are calculated for this process.

These numbers along with the corresponding capillary number is given at the legend of figure 7-16(a). For this spreading process, the values of Deborah number and Weissenberg number are much smaller than one. The largest Deborah number is $De = 3 \times 10^{-5}$ and largest Weissenberg number is $Wi = 0.16$. Thus, there is no evidence that the non-Newtonian effects can cause the the appearance of this thin film.

There is another possible source for the generation of the foot-like film. If we look back to the rate of spreading, figure 7-13, for the oligomer oil and PS025 Boger fluid, for drops with approximately the same size, Boger fluids spread slower than the oligomer oil.

Earlier in this section in figure 7-11 the results of dynamic surface tension measurement for Oligomer oil and ideal dilute solution was presented. The solid line is an exponential fit to the oligomer oil result and the dashed line is an exponential fit to PS025 result. The relaxing time scale found from these exponential fits are 263 s for the oligomer oil and 555 s for PS025 Boger fluids. This difference on the relaxation time in wetting the Wilhelmy plate can possibly be the source of generation of the thin film in front of the moving contact line of PS025 Boger fluid.

It is possible that at the beginning of spreading process, a thin film of the oligomer fluid separates itself from the dilute solution of PS025 and advance in front of the moving front of PS025. Thus early in the process there would be a film in front of the moving front. However, since the oligomer oil is not a perfectly wetting fluid on silicon wafer, and its spreading rate decreases with time, the bulk of PS025 fluid spreading on a prewetted surface of the oligomer oil eventually catches up with the film until an equivalent contact angle is approached 7.3.2. This c

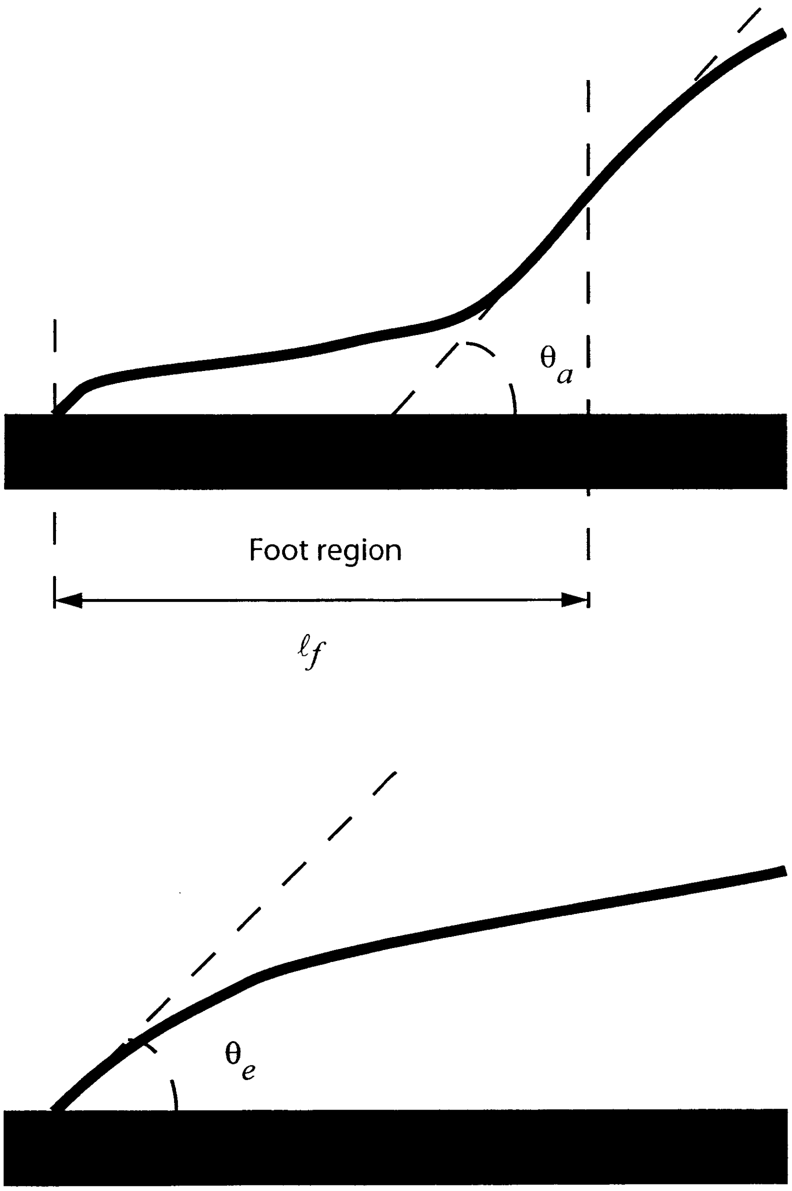

Figure 7-18: The schematic of phase separation and foot region for spreading of the Boger fluid. The top figure is early in the spreading process and a foot structure exists at the moving contact line. The the equilibrium state with no foot is presented in the bottom figure.

Chapter 8

Conclusions

The development of high resolution measurement techniques with high lateral and/or vertical resolution over the last 30 years has provided a major breakthrough in the understanding of microscale phenomena in various subjects in science. Techniques such as interferometry, Atomic Force Microscopy (AFM), Scanning Electron Microscopy (SEM), confocal microscopy, X-ray diffraction, and ellipsometry have been widely used in material science, surface science, physics, and biology. Concurrent developments in computers (hardware and software) especially assisted the evolution of these instruments, not only as a reliable control systems, but also as data acquisition systems that can acquire accurate experimental information in very short spans of time (high sampling rates). Optical systems have also made great contributions to these subjects. New precision production techniques in optics industry have enabled researchers to use high quality optical elements. Optical techniques are of special interest for investigations of phenomena which are sensitive to external disturbances. For example to quantitatively understand the physics of fluid flow, a non-invasive measurement system is desired to in order to keep the flow undisturbed. The work presented in this thesis takes advantage of modern optical measuring techniques and data acquisition systems to quantify the dynamics of spreading liquids.

The capabilities of the optical systems used in our experiments for characterizing the free surfaces of fluid films were demonstrated in chapter 2. The confocal surface metrology system (LT-8110, Keyence Inc.) was shown to be a non-invasive measurement system with lateral resolution of 7μm and vertical resolution of 0.5μm. This system is based on the confocal principle and is calibrated to measure changes of height on a surface with a response time of $\sim$ 2.2ms. It was shown that this system can be used in experiments when macroscopic features such as the radius of a spreading drop, or the thickness of the drop (especially far from the contact line) are of interest. The large working distance (25mm) and wide dynamic range of measurements in the vertical direction ($\pm$1mm) combined with the fast response time, makes the confocal technique a useful tool in our experiments.

The other optical system which was widely used throughout this thesis is a phase-shifted interference microscope which was based on the phase-shifted laser feedback interferometry principle [87]. It was shown that by using a phase-shifting algorithm, the lateral resolution of the feedback interferometer could be improved drastically. Our calibrations showed that the system has a lateral resolution of 0.9μm (diffraction limited) and vertical resolution of 10nm. The dynamic response of this system was shown to be $\sim$ 1ms. The broad dynamic range of this system enables us to not only investigate the microscopic structure of the moving contact line but also simultaneously measure the thickness of transparent liquid samples with thicknesses of up to 100μm, in sharp contrast to other high resolution optical systems such as ellipsometry which has a resolution of tens of Angstroms but the maximum measured thickness of approximately 500 Å.

The steady spreading of perfectly wetting fluids ($S > 0$) on smooth solid substrates was presented in chapter 3. We have shown that the physical properties of the fluid, such as viscosity, surface tension, and density, as well as the characteristic size of the drop (as quantified by the dimensionless scale $\phi = (\Omega/\pi)^{1/3}/\ell_{cap}$) have profound effects on the spreading process. To compare the resisting force of spreading, we introduced the Ohnesorge number $Oh = \mu/\sqrt{\rho R \sigma} \times R/h$, which quantifies the ratio of the viscous time scale for spreading to the inertial time scale in the presence of the capillary effect. If $Oh \ll 1$, inertia is the dominant resisting force and conversely if $Oh \gg 1$, then the viscous force is the dominant dissipating force. The shape of the free surface of the spreading drop, $R(t)$, and the rate of spreading of drop, $\dot{R}(t)$, depend on the relative importance of these parameters. We have separated these regimes into three major categories for spreading of viscous drops. For large viscous drops, $\phi > 1$ and $Oh > 1$, the effect of gravity is important and the gravitational force becomes the main driving force in the spreading with viscous forces resisting the spreading of these gravity current. If the viscous drop is small ($\phi < 1$, $Oh \gg 1$), then the gravitational forces are negligible and capillarity acts as the driving force. Due to the shape of drop in this case, this regime of spreading is usually called the spherical cap regime. For drops with small Ohnesorge number it is inertia, instead of viscosity, that initially provides the resistance to the spreading. However, the Ohnesorge number increases with time and eventually viscosity becomes the dominant resisting force. We have shown that drops in all of these regimes ultimately spread to have the shape of an approximately constant film of fluid except in a region close to the moving contact line (on a lateral distance of order of ℓ_{cap}). This type of spreading is called the pancake regime due to the shape of the drop. All of these regimes are summarized in figure 3-2.

We used scaling analysis and direct solution of the governing equations to show the power-law relations that connect the radius of spreading drop and time. We have shown that each of these regimes has a different power-law exponent due to the interaction of different driving and resisting forces. For the gravity current regime, this relation was found to be $R \sim t^{1/8}$, however for the spherical cap and the pancake regimes, the power-law relations become $R \sim t^{1/10}$ and $R \sim t^{1/7}$, respectively. For the case of $Oh < 1$ where inertia resists the spreading, the power-law is $R \sim t^{2/3}$. We also demonstrated that as a result of conservation of mass of the spreading drop, the maximum thickness of drop has closely related power-law relations for the different regimes that can be derived using the expression $h \cong \Omega/2\pi R^2$. Finally, the dynamic contact angle of the drop can be determined from $\theta_a \sim h(t)/R(t)$, and the corresponding power-laws for each regime can be derived accordingly. We used the confocal system to compare the power-laws derived from theoretical analysis with the experimental results and showed that the front factors and exponents are in quantitative agreement with predictions.

We have also applied the psLFI measuring system to investigate the inter-relation between the microscopic and macroscopic structure of the free surface at the vicinity of contact line. These results were shown in chapters $3-5$. In chapter 3, the evolution of the dynamic contact angle, θ_a, is documented for a wide range of capillary numbers ($10^{-7} < Ca < 10^{-3}$). The resolution (lateral and vertical) and dynamic range of psLFI is sufficient to enable us to quantify the drop profile from very close distances to the substrate ($\sim$ 10nm) until the macroscopic thickness of the spreading drop is attained ($\sim 10\mu$m). This feature allowed us to locate and quantify the inflection point on the free surface of the drop. The slope at this point is, by common definition, the dynamic contact angle [79]. The coupling between the microscopic and macroscopic regimes that is observed in our measurements is in good agreement with theoretical analysis and numerical simulation. The variation of measured dynamic contact angle with capillary number shown in chapter 3, is roughly consistent with the Hoffman-Voinov-Tanner law ($\theta_a \sim Ca^{1/3}$);however we were able to confirm the existence of an additional logarithmic dependence on the capillary number, which was predicted by de Gennes [30], Pismen et al. [93], and Eggers & Stone [37]. This logarithmic function has not only a capillary number dependence, but also a geometric factor which can be interpreted as the ratio of a macroscopic length scale (ℓ_{mac}) to a microscopic length scale (ℓ_{mic}). This is additional evidence of the importance of an experimental technique that can measure both the microscopic and macroscopic scale of the drop. We also demonstrated the presence the so-called size effect by performing the same experiments using silicon strips that laterally constraint the spreading to generate a two dimensional flow instead of axisymmetric spreading. The results of two dimensional spreading have better agreement with the HVT law because this law is derived under the assumption of two dimensional spreading.

In addition to the measurements of the dynamic contact angle, we were able to observe a microscopic film that exists in front of the moving contact line. This film is often called the adiabatic precursor film. The length of this film is measured by observing the interferometric fringe visibility, m, and the measured thickness of the drop. We have shown that the value of m decreases rapidly before the macroscopic droplet moves past the measurement point. This sudden drop in m is due to the thin precursor film of fluid in front of the moving contact line. We showed that the length of the adiabatic precursor film, L_P, is inversely proportional to the capillary number of the spreading drop as was first predicted by Joanny & de Gennes [68]. The thickness of this film ($\sim$ 100 nm) was found to be approximately constant for our range of experimental parameters.

Spreading of viscous drops on inclined plates were considered in chapter 5. The effect of an additional driving force due to the new resolved component of gravitational force were demonstrated. The profiles and rate of spreading of drops for a range of inclination angles ($0 < \alpha < 25°$) were measured. The dimensionless form of these profiles were plotted using the similarity parameters given by Huppert [64] and are in fair agreement with the theoretical prediction far enough from the contact line and from the point of maximum thickness. This is due to the fact that the theory is only valid for regions close enough to the contact line but only considers a contact angle of 90° which is not in agreement with measured contact angles. The variation of the dynamic contact angle with capillary number for these drops have a fair agreement to our results in chapter 3 for small Ca. However for $Ca > 0.01$, a new power-law with higher exponent is found to control the spreading behavior. We showed that for $Ca \ll 1$, the lubrication approximation is valid due to the small dynamic contact angles and $Ca \equiv Bo = \rho g h_N^2 \sin\alpha/\sigma$ where h_N is the maximum thickness of the drop. However for $Ca > 0.01$, due to the breakdown of lubrication approximation, the measured capillary number $Ca_{exp} = \mu U/\sigma$, where U is the measured velocity of moving contact line, is not equal to the measured Bond number $Bo_{exp} = \rho g h_N^2 \sin\alpha/\sigma$ which is calculated by measuring h_N. This breakdown in the lubrication approximation needs more experimental and analytical investigation in the future.

During our spreading experiments (chapter 3), we discovered surface waves that develop along free surface of spreading drops when the fluids are slightly volatile. These waves were due to evaporatively-driven Marangoni instabilities that induced by lateral surface tension gradients because of local evaporation of the fluid. In chapter 6, we showed that the viscosity and volatility of the fluid control the onset of the instability. Our experiments also showed that the surface roughness, and substrate thermal diffusivity can affect the dynamic characteristics of the waves. For substrates such as glass with very low thermal diffusivity, the instability is eliminated. We performed a linear stability analysis to characterize these effects and we showed that there is a parameter, interfacial thermal resistance $\mathcal{R}$, that has a major contribution to the onset of the instability. For $\mathcal{R}$ larger than a critical value, ($\mathcal{R}_{crit} = 2$, surface perturbations are linearly unstable and grow. Since $\mathcal{R}$ is inversely proportional to the thickness of the drop, there is a thickness for each drop that set the onset of the instability and depends on the material properties of the liquid. In our analysis, we assumed the surface temperature remains constant throughout the process and we neglected the effect of enhanced evaporation at the moving contact line. The analysis used here was essentially a one dimensional problem. As future work, these parts can be integrated into a general two-dimensional system that couples substrate and film and contact line region and include mass transfer, heat transfer, conduction in solid substrate, and fluid mechanics of the system.

The working fluids in chapter $3-6$ are all Newtonian fluids. In chapter 7, we presented the features of spreading of non-Newtonian fluid on a solid substrate. The spreading characteristics of highly entangled polymer melts ($10 < Z < 35$) and viscoelastic polymer solutions (Boger fluids) were shown to be different form unentangled polymer melts ($Z < 1$). Macroscopically, the spreading regimes both exhibit power-law spreading characteristics at short times. However, the Boger fluid is not a perfectly wetting fluid on the silicon substrate surface and spreading slows down before eventually stopping after a long time, whereas PDMS is a perfectly wetting fluid and spreads the surface until it fully covers the surface. It was shown that the variation of the dynamic contact angle as a function of capillary number for Boger fluid (and oligomer oil) follows a modified HVT law (equation 7.28). Microscopically, the existence of the 'foot' feature first predicted by Brochard & de Gennes [16] was confirmed for the highly entangled polymer melts. We were able to characterize this structure and we showed that the length and thickness of the foot roughly agree with the theoretical predictions. The length of the foot decreases with increasing Ca substantially faster than the theoretical prediction. The thickness of the foot, h_f, is on the same order as the slip length ℓ_{slip} according to the theory, however the measured value of h_f in our experiments are significantly lower than estimated values of the slip length $\ell_{slip} = \ell_{mic} N_e Z^3$. We also shown that the modified version of the theory by Bruinsma [17] who included the effect of polymer mobility and predicted lower thickness for h_f.

A foot-like structure close to the moving contact line of spreading Boger fluid was also observed and documented in chapter 7. However, unlike the foot for highly entangled polymer melts, the length of this foot-like structure decreases as Ca decreases. We argued that this structure arises from differential mobility of the large polymer molecules and smaller oligomeric solvent molecules across the solid substrate close to the moving contact line.

In this thesis, we have demonstrated the close connection between the microscopic and the macroscopic regions of the spreading viscous drop in the vicinity of moving contact lines. The validity of the Hoffman-Voinov-Tanner law and its modifications were investigated. As shown, several parameters can affect the spreading of drops on solid surfaces. We chose silicon wafer as our solid substrate due to the fact that it has a very smooth surface (elimination of roughness effects) and it is very clean when purchased. In future, to further explore the effect of spreading coefficient S (equation 1.2), one might choose high energy or low energy surfaces as substrate. Another effect observed in our experiments was the 'size effect' which leads to the geometry dependence of the modified HVT law as shown in table 3.1. We only considered spontaneous spreading of drop on a flat substrate. Other type of spreading such as forced spreading and spreading on curved surfaces, such as inside or outside of a capillary tube, are good examples for future direction of these experiments [69].

Another aspect of our experiments that can be expanded is the theoretical analysis of the foot region in front of the moving contact line as shown in chapter 7. Even though we confirmed the existence of the foot structure for spreading of highly entangled polymer melts, the predicted scaling and experiments did not fully agree with each other. Also the shape of the foot is different than the predicted shape [16], as the measured profiles have an extra inflection point very close to the moving contact line (figure 7-7), we plan to explore the this further. The existence of a new 'foot-like' structure for spreading of a dilute ideal elastic polymer solution was also reported in this thesis. However, the physics behind this new structure is still unclear and need more detailed experiments and analysis.

It is unlikely that progress with such free surface flows of multicomponent viscoelastic fluids will require collaboration between microscale experimentation, asymptotic analysis, and molecular dynamic simulations.

Appendix A

Material properties

In this appendix, the properties of all of the materials used throughout this thesis are tabulated and plotted.

Table A.1: Physical properties of PDMS fluids used in the spreading experiments.

Fluids	M_w [kg/kmol]	η_0 [Pa s]	σ [N/m]	N_K	Z
DMS-T01	237	0.001	17.4×10^{-3}	1	<1
DMS-T01.5	340	0.0015 *	18.0×10^{-3}*	1	<1
DMS-T02	410	0.002 *	18.7×10^{-3}*	1	<1
DMS-T03	550	0.003 *	19.2×10^{-3}*	2	<1
DMS-T05	770	0.005 *	19.7×10^{-3}*	2	<1
DMS-T07	950	0.007 *	19.9×10^{-3}*	3	<1
DMS-T11	1250	0.01	20.1×10^{-3}	4	<1
DMS-T12	2000	0.02 *	20.6×10^{-3}*	6	<1
DMS-T15	3780	0.05 *	20.8×10^{-3}*	11	<1
DMS-T21	5970	0.1	20.9×10^{-3}	17	<1
DMS-T22	9430	0.2 *	21.0×10^{-3}*	27	<1
DMS-T23	13650	0.35	21.1×10^{-3}*	39	1
DMS-T25	17250	0.5	21.1×10^{-3}	49	1
DMS-T31	28000	1.0	21.3×10^{-3}	80	2
DMS-T35	49350	5.0	21.5×10^{-3}	141	4
DMS-T41	62700	10.0	21.5×10^{-3}	179	5
DMS-T41.2	67700	12.5 *	21.5×10^{-3}*	193	6
DMS-T43	91700	30.0 *	21.5×10^{-3}	262	7
DMS-T46	116500	60.0 *	21.5×10^{-3}*	333	10
DMS-T51	139000	100.0	21.5×10^{-3}	397	11
DMS-T53	204000	300.0	21.5×10^{-3}*	583	17
DMS-T56	260000	600.0	21.6×10^{-3}*	743	21
DMS-T61	308000	1000.0	21.6×10^{-3}*	880	25
DMS-T63	423000	2500.0	21.6×10^{-3}*	1208	35

Data include (M_w) molecular weight; (η_0) viscosity; (σ) surface tension; (N_K) number of Kuhn steps; and (Z) number of entanglements in polymer chain. A number $Z < 1$ corresponds to a non-entangled fluid. Values of properties indicated by ($*$) are provided by the manufacturer (Gelest Inc.).

Table A.2: Thermal and physical properties of silicon oils used in chapter 6.

Fluids	DMS-T01	DMS-T11	DMS-T21	DMS-T41	DMS-T07R
a.k.a	L	M	H	V	NV
μ [Pa s]	0.001	0.01	0.1	10	0.007
ρ [kg/m^3]	818	935	966	977	920
σ [N/m]	0.0174	0.0201	0.0209	0.0210	0.0180
k [W/mK]	0.1256	0.1256	0.1256	0.1256	0.1256
α [m^2/s]	10^{-7}	9.2×10^{-8}	8.9×10^{-8}	8.8×10^{-8}	9.1×10^{-8}
Pr	1.2×10^{1}	1.16×10^{2}	1.16×10^{3}	1.07×10^{5}	8.3×10^{1}
$d\sigma/dT$ [N/mK]	-7.63×10^{-5}	-8.28×10^{-5}	-9.5×10^{-5}	-3.77×10^{-5}	–
$\Delta H_\mu/R$ [K]	1093.5	1660.4	2138.9	5582.9	–
μ_0 [Pa s]	8.7×10^{-4}	9.6×10^{-3}	9.8×10^{-2}	6.74	–
ΔH_v [J/mol]	12896	60837	66531	82903	108653
M_w [kg/kmol]	237	1250	5970	62700	950
T_{sat} [K]	284	290	295	573	510

data include (μ) viscosity; (ρ) density; (k) thermal conductivity; (α) thermal diffusivity; (Pr) Prandtl number; ($d\sigma/dT$) variation of surface tension with temperature; ($\Delta H_\mu/R$) and (μ_0) constants for variation of viscosity with temperature; (ΔH_ν) heat of evaporation; (M_w) molecular weight; and (T_{sat}) saturation temperature.

Figure A-1: Dependence of (a) surface tension and (b) viscosity of the working fluids on temperature. Data include (□) L; (•) M; (△) H, from table A.2

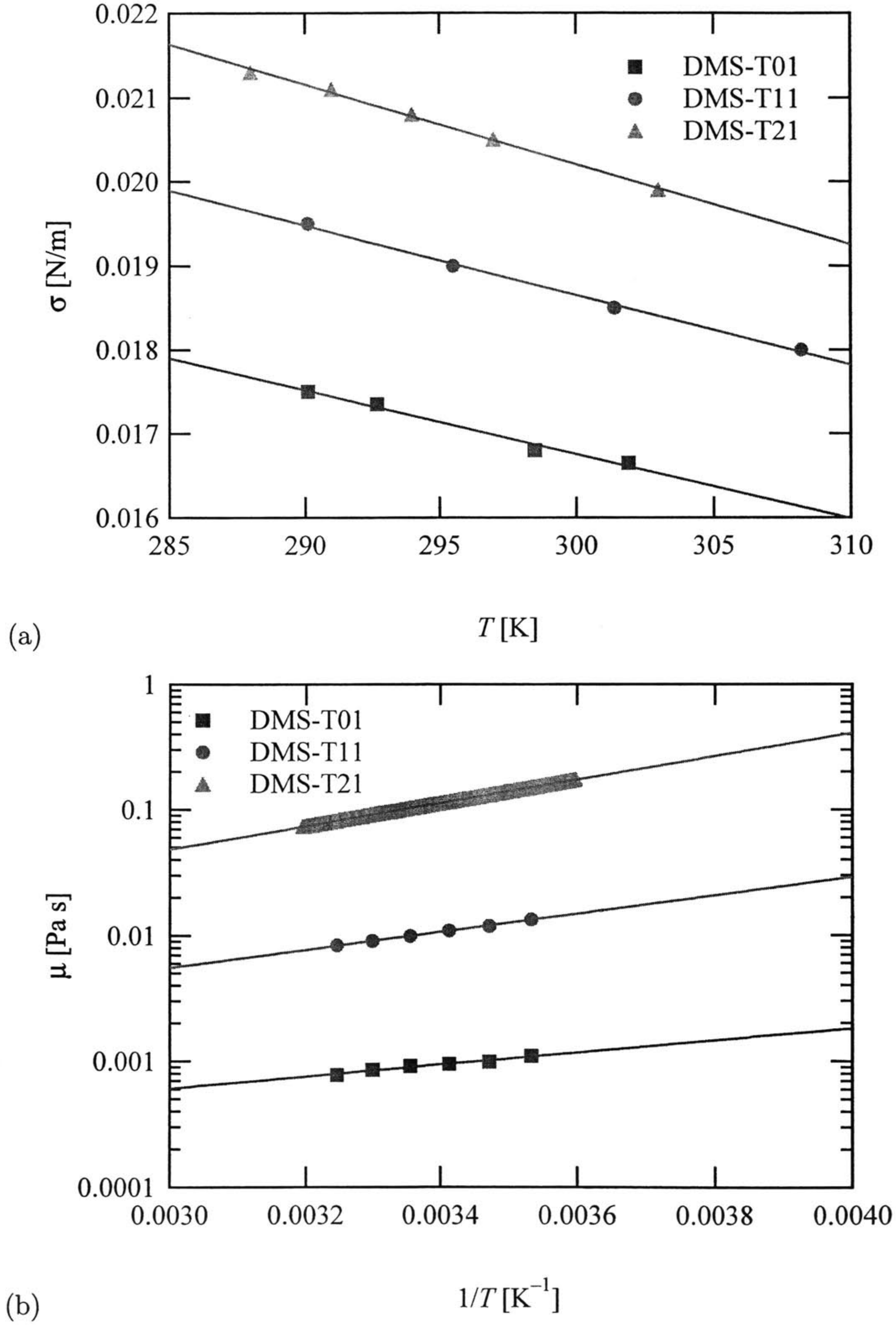

Table A.3: Thermal and physical properties of substrate materials.

Substrate	Copper	Silicon	Brass	Glass
k [W/mK]	399	153	111	0.81
α [m^2/s]	1.16×10^{-4}	9.34×10^{-5}	3.41×10^{-5}	3.40×10^{-7}
C_P [J/kgK]	383	703	385	800
ε_s [µm]	10, 1	0.01	1	0.01

Data include (k) thermal conductivity; (ϵ_s) average roughness; (C_P) specific heat; and (α) thermal diffusivity. Copper substrates with two surface roughness were used in the experiments.

Figure A-2: Dependence of steady shear viscosity of PDMS fluids on shear rate. The number of entanglements of these fluids are given in table A.1. These curves are truncated due to onset instability when shear stress reaches a maximum value.

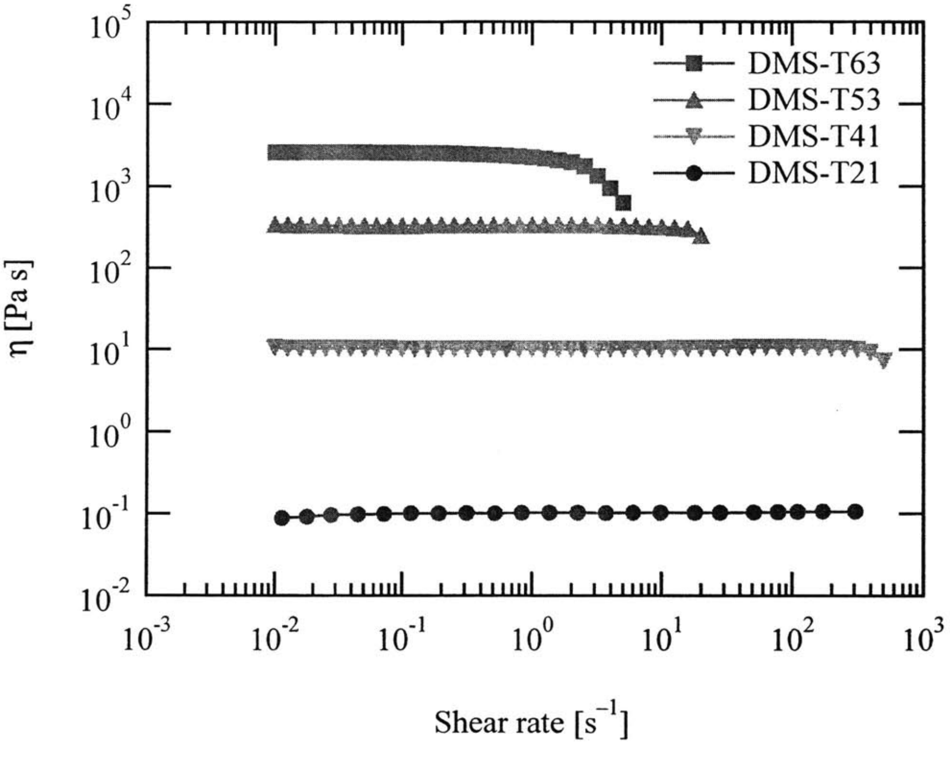

Bibliography

[1] *FTÅ measurement capabilities.* http://www.firsttenangstroms.com.

[2] A.W. Adamson and A.P. Gast. *Physical chemistry of surfaces.* Wiley, New York, 1997.

[3] S.L. Anna. *Filament stretching of model elastic liquids.* PhD thesis, Harvard university, Cambridge, Massachusetts, USA, 2000.

[4] D. Ausserré, A.M. Picard, and L. Léger. Existance and role of the precursor film in the spreading of polymer liquids. *Phys. Rev. Lett.*, 57(21):2671–2674, 1986.

[5] G.I. Barenblatt. *Scaling, self-similarity, and intermediate asymptotics : Dimensional analysis and intermediate asymptotics.* Cambridge Univ. Press, London, 1996.

[6] W.D. Bascom, R.L. Cottington, and C.R. Singleterry. *Contact Angle, Wettability, and Adhesion*, volume 43 of *Advances in Chemistry Series.* ACS, Washington, DC, 1964.

[7] D. Beaglehole. Profiles of the precursor of spreading drops of siloxane oil on glass, fused silica, and mica. *J. Phys. Chem.*, 93:893–899, 1989.

[8] H. Bénard. Les tourbillions cellulaires dans une nappe liquide transportant de la chaleur par convection en régime permanent. *Ann. Chim. Phys.*, 23:62–144, 1901.

[9] A. Bertozzi and M. Brenner. Linear stability and transient growth in driven contact lines. *Phys. Fluids*, 9(3):530–539, 1997.

[10] J. Bicerano. *Prediction of polymer properties.* Marcel Dekker, Inc., New York, USA, 1996.

[11] R.B. Bird, R.C. Armstrong, and O. Hassager. *Dynamics of polymeric liquids, Vol. 1.* John Wiley & Sons, Inc., New York, USA, 1987.

[12] T.D. Blake, C. Decamps, J. De Coninck, M. de Ruijter, and M. Voué. The dynamics of spreading at the microscopic scale. *Coll. Sur. A.*, 154:5–11, 1999.

[13] D.V. Boger. A highly elastic constant-viscosity fluid. *J. Non-Newtonian Fluid Mech.*, 3:87–91, 1977/78.

[14] A.V. Borkar, J.A. Tsamopoulos, S.A. Gupta, and R.K. Gupta. Spin coating of viscoelastic and novolatile fluids over planar disk. *Phys. Fluids*, 6(11):3539–3553, 1994.

[15] M. Brenner and A. Bertozzi. Spreading of droplets on a solid surface. *Phys. Rev. Lett.*, 71(4):593–596, 1993.

[16] F. Brochard and P.-G. de Gennes. Spreading laws for liquid polymer droplets: interpretation of the "foot". *J. Physique Lett.*, 45:596–602, 1984.

[17] R. Bruinsma. Slow spreading of polymer melts. *Macromolecules*, 23:276–280, 1990.

[18] A.M. Cazabat and M.A. Cohen Stuart. Dynamics of wetting: Effects of surface roughness. *J. Phys. Chem.*, 90:5845–5849, 1986.

[19] J.-D. Chen. Experiments on a spreading drop and its contact angle on a solid. *J. Coll. Inter. Sc.*, 122(1):60–72, 1988.

[20] J.-D. Chen and N. Wada. Wetting dynamics of the edge of a spreading drop. *Phys. Rev. Lett.*, 62(26):3050–3053, 1989.

[21] J.-D. Chen and N. Wada. Edge profiles and dynamic contact angle of spreading drop. *J. Coll. Inter. Sc.*, 148(1):207–222, 1992.

[22] Q. Chen, E. Ramé, and S. Garoff. The breakdown of asymptotic hydrodynamic models of liquid spreading at increasing capillary number. *Phys. Fluids*, 7(11):2631–2639, 1995.

[23] T.R. Corle and G.S. Kino. *Confocal scanning optical microscopy and related imaging systems.* Academic Press, San Diego, 1996.

[24] R.G. Cox. The dynamics of the spreading of liquids on a solid surface. part 1. surfactants. *J. Fluid Mech.*, 168:195–220, 1986.

[25] R.G. Cox. The dynamics of the spreading of liquids on a solid surface. part 1. viscous flow. *J. Fluid Mech.*, 168:169–194, 1986.

[26] J. Daillant, J.J. Benattar, and L. Léger. Ultrathin films in wetting evidenced by x-ray reflectivity. *Phys. Rev. A*, 41(4):1963–1977, 1990.

[27] S.H. Davis. Thermocapillary instabilities. *Annu. Rev. Fluid Mech.*, 19:403–435, 1987.

[28] P.-G. de Gennes. Reptation of a polymer chain in the presence of fixed obstacles. *J. Chem. Phys.*, 55:572–579, 1971.

[29] P.-G. de Gennes. *Scaling concepts in polymer physics.* Cornell Univ. Press, Ithaca, NY, 1978.

[30] P.-G. de Gennes. Wetting: Statics and dynamics. *Rev. Mod. Phys.*, 57:827–863, 1985.

[31] R.D. Deegan, T.F. O. Bakajin, G. Dupont, and S.R. Nagel Huber, and T.A. Witten. Capillary flow as the cause of ring stains from dried liquid drops. *Nature*, 389:827–829, 1997.

[32] B.V. Derjaguin. Definition of the concept of, and magnitude of the disjoining pressure and its role in the statics and kinetics of thin layers of liquids. *Colloid J. USSR (English translation)*, 10:191–197, 1955.

[33] N. Didden and T. Maxworthy. The viscous spreading of plane and axisymmetric gravity currents. *J. Fluid Mech.*, 121:27–42, 1982.

[34] P.G. Drazin and W.H. Reid. *Hydrodynamics instabilities.* Cambridge Univ. Press, London, 1981.

[35] E.B. Dussan V. On the spreading of liquids on solid surfaces: static and dynamic contact lines. *Ann. Rev. Fluid Mech.*, 11:371–400, 1979.

[36] E.B. Dussan V., E. Ramé, and S. Garoff. On identifying the appropriate boundary conditions at a moving contact line: an experimental investigation. *J. Fluid Mech.*, 230:97–116, 1991.

[37] J. Eggers and H.A. Stone. Characteristic lengths at moving contact lines for a perfectly wetting fluid: the influence of speed on the dynamic contact angle. *J. Fluid Mech. Under consideration for publication*, 2003.

[38] P. Ehrhard. Experiments on isothermal and non-isothermal spreading. *J. Fluid Mech.*, 257:463–483, 1993.

[39] P. Ehrhard and S.H. Davis. Non-isothermal spreading of liquid drops on horizontal plates. *J. Fluid Mech.*, 229:365–388, 1991.

[40] X. Fanton and A.M. Cazabat. Spreading and instabilities induced by a solutal marangoni effect. *Langmuir*, 14:2554–2561, 1998.

[41] J.A. Fay. *The spreading of oil slicks on a calm sea*, chapter Oil on the sea, pages 53–63. New York, d. p. hoult ed. edition, 1969.

[42] A. Ferry, T. Pompe, and S. Herminghaus. *Nanometer resolution of liquid surface topography by scaning force microscopy*, chapter Apparant and microscopic contact angles, pages 13–25. 2000.

[43] J.D. Ferry. *Viscoelastic properties of polymers.* John Wiley & Sons, Inc., New York, New York, USA, 1980.

[44] D. Fischer and B. Ovryn. Surface profilometry of a thick liquid lens on a solid surface using a high numerical aperture phase-shifted laser feedback interferometer. *SPIE*, 3782:378–389, 1999.

[45] R. Fondecave, A. Buguin, and F. Brochard. Effet parasite en ellipsometrie. *C. R. Acad. Sci. Paris*, 327(II B):407–414, 1999.

[46] N. Fraysse and G.M. Homsy. An experimental study of rivulet instabilities in centrifugal spin-coating of viscous newtonian and non-newtonian fluids. *Phys. Fluids*, 6(4):1491–1504, 1994.

[47] G. Friz. Uber den dynamischen randwinkel im fall der voll standigen benetzung. *Zeit. fur angew. Physik*, 19:374–378, 1965.

[48] R. Goodwin and G.M. Homsy. Viscous flow down a slop in the vicinity of a contact line. *Phys. Fluids A*, 3(4):515–528, 1991.

[49] W.P. Hardy. The spreading of fluids on glass. *Philos. Mag.*, 38:49–55, 1919.

[50] P. Hariharan, B.F. Oreb, and T. Eliju. Digital phase-shifting interferometry: a simple error-compensating phase calculation algorithm. *Appl. Opt.*, 26(13):2504–2507, 1987.

[51] E. Hecht. *Optics.* Addison Wesley, Reading, Massachusetts, 1998.

[52] H. Hervet and P.-G. de Gennes. Surface and interphase physics.-the dynamics of wetting: Precursor films in the wetting of “dry”solids. *C. R. Acad. Sci. Paris*, 299(11):499–503, 1984.

[53] F. Heslot, A.M. Cazabat, P. Levinson, and N. Fraysee. Experiments on wetting on the scale of nanometers: influence of the surface energy. *Phys. Rev. Lett.*, 65(5):599–602, 1990.

[54] F. Heslot and and P. Levinson Cazabat, A.M. Dynamics of wetting on thiny drops: ellipsometric study of the late stages of spreading. *Phys. Rev. Lett.*, 62(11):1286–1289, 1989.

[55] F. Heslot, N. Fraysee, and A.M. Cazabat. Molecular layering in the spreading of wetting liquid drops. *Nature*, 338(6217):640–642, 1989.

[56] P. Hiemenz and R. Rajagopalan. *Principles of Colloid and Surface Chemistry.* New York, Marcel Dekker, 1997.

[57] L.M. Hocking. The spreading of a thin drop by gravity and capillarity. *Q. J. Appl. Math.*, 36:55–69, 1983.

[58] L.M. Hocking and A.D. Rivers. The spreading of a drop by capillary action. *J. Fluid Mech.*, 121:425–442, 1982.

[59] R.L. Hoffman. A study of the advancing interface. *J. Coll. Inter. Sci.*, 50(2):228–241, 1975.

[60] A.E. Hosoi and J.W.M. Bush. Evaporative instabilities in climbing films. *J. Fluid Mech.*, 442:217–239, 2001.

[61] D.P. Hoult. Oil spreading on the sea. *Ann. Rev. Fluid. Mech.*, 4:341–368, 1972.

[62] H. Hu and R.G. Larson. Micro-fluid dynamics in an evaporating sessile droplet. In *Fifth microgravity fluid physics and transport phenomena conference*, Cleveland, Ohio, U.S.A., 2000.

[63] H. Hu and R.G. Larson. Evaporating of a sessile droplet on a substrate. *J. Phys. Chem. B*, 106:1334–1344, 2002.

[64] H.E. Huppert. Flow and instability of a visocus current down a slope. *Nature*, 300:427–429, 1982.

[65] H.E. Huppert. The propegation of two-dimensional and axisymmetric viscous gravity currents over a rigid horizontal surface. *J. Fluid Mech.*, 121:43–58, 1982.

[66] H. Jeffreys. The stability of a layer of fluid heated from below. *Phil. Mag.*, 2:833–844, 1926.

[67] H. Jeffreys. Some cases of instability in fluid motion. *Proc. Roy. Soc. A*, 118:195–208, 1928.

[68] J.F. Joanny and P.-G. de Gennes. Upward creep of a wetting fluid: a scaling analysis. *J. Phys. (Paris)*, 47:121–127, 1986.

[69] S.F. Kistler. *Wettability*, chapter Hydrodynamics of wetting, pages 311–429. Surfactant science series.49. Marcel Dekker Inc., 1993.

[70] J.F. Klausner, L.Z. Zeng, and D.M. Bernhard. Development of a film thickness probe using capacitance asymmetrical two-phase flow with heat addition. *Rev. Sci. Instrum.*, 63(5):3147–3152, 1992.

[71] R. G. Larson. *The structure and rheology of complex fluids.* Oxford Univ. Press, New York, New York, USA, 1999.

[72] C.J. Lawrence and W. Zhou. Spin coating of non-newtonian fluids. *J. Non-Newtonian Mech.*, 39:12–23, 1991.

[73] L. Léger, M. Erman, Guinet-Picard, D. A.M., Ausserré, and C. Strazielle. Precursor film profiles of spreading liquid drops. *Phys. Rev. Lett.*, 60(23):2390–2393, 1988.

[74] F.Y. Lewandowski and D. Dupuis. Dynamic measurements of surface tension of solutions of polyisobutylene in mixtures of polybutene oil and decalin. *J. Non-Newtonian Mech.*, 52:233–248, 1994.

[75] A.R. Low. On the criterion for stability of a layer of a fluid heated from below. *Proc. Roy. Soc. A*, 125:180–195, 1929.

[76] M.E. Mackay and D.V. Boger. An explanation of the rheological properties of boger fluids. *J. Non-Newtonian Fluid Mech.*, 22:235–243, 1987.

[77] J.A. Marsh, S. Garoff, and E.B. Dussan V. Dynamic contact angles and hydrodynamics near a moving contact line. *Phys. Rev. Lett.*, 70(18):2278–2281, 1993.

[78] G. McHale, M.I. Newton, S.M. Rowan, and M. Banerjee. The spreading of small viscous stripes of oil. *J. Phys. D: Appl. Phys.*, 28:1925–1929, 1995.

[79] S. Middleman. *Modeling axisymmetric flows.* Acadenic Press, Inc., San Diego, Ca, 1995.

[80] A.V. Mirzamoghadam and I. Catton. Holographic interferometry investigation of enhanced tube meniscus behavior. *Journal of Heat Transfer*, 110:208–213, 1988.

[81] C.G. Ngan and E.B. Dussan V. On the nature of the dynamic contact angle: an experimental study. *J. Fluid Mech.*, 118:27–40, 1982.

[82] D.A Nield. Surface tension and buoyancy effects in cellular convection. *J. Fluid Mech.*, 19:341–352, 1964.

[83] V.A. Ogarev, T.N. Timonina, V.V. Arsalanov, and A.A. Trapeznikov. Spreading of polydimethylsiloxane drops on solid horizontal surfaces. *J. Adhesion*, 6:337–355, 1974.

[84] A. Oron and and S.G. Bankoff S.H. Davis. Long-scale evolution of thin films. *Reviews of Modern Physics*, 69(3):931–980, 1997.

[85] B. Ovryn and J.H. Andrews. Phase-shifted laser feedback interferometry. *Opt. Lett.*, 23(14):1078–1080, 1998.

[86] B. Ovryn and J.H. Andrews. Measurement of changes in optical path length and reflectivity with phase-shifting laser feedback interferometry. *Appl. Opt.*, 38(10):1959–1967, 1999.

[87] B. Ovryn, J.H. Andrews, and S. Eppell. Phase-measuring laser feedback interferometry: application to microscopy. *SPIE*, 2655:153–163, 1996.

[88] B. Ovryn, J.H. Andrews, S. Eppell, and J. Khydarov. Phase-shifted, real-time laser feedback interferometry. *SPIE*, 2860:263–275, 1996.

[89] H.J. Palmer. The hydrodynamic stability of rapidly evaporating liquids at reduced pressure. *J. Fluid Mech.*, 75:487–511, 1976.

[90] H. Pascal. Gravity flow of a non-newtonian fluid sheet on an inclined plane. *Int. J. Engng. Sci.*, 29(10):1307–1313, 1991.

[91] R.E. Pattle. Diffusion from a point source with a concentration-dependent coefficient. *Q. J. Mech. Appl. Math.*, 12:407–409, 1959.

[92] J.R.A. Pearson. On convection cells induced by surface tension. *J. Fluid Mech.*, 4:489–500, 1958.

[93] L.M. Pismen, B.Y. Rubinstein, and I. Bazhlekov. Spreading of a wetting film under the action of van der waals forces. *Phys. Fluids*, 12(3):480–483, 2000.

[94] T. Pompe, A. Ferry, and S. Herminghaus. *Apparant and microscopic contact angles*, chapter Measurement of contact line tension by analysis of the three-phase boundary with nanometer resolution, pages 480–483. 2000.

[95] Lord Rayleigh. On the convection currents in a horizontal layer of liquid when the higher temperature is on the under side. *Phil. Mag.*, 32:529–546, 1916.

[96] C. Redon, F. Brochard-Wyart, and F. Rondelez. Festoon instabilities of slightly volatile liquids during spreading. *J. Phys. II France*, 2:1671–1676, 1992.

[97] S.N. Reznik and A.L. Yarin. Spreading of a viscous drop due to gravity and capillarity on a horizontal or an inclined dry wall. *Phys. fluids*, 14(1):118–132, 2002.

[98] J.P. Rothstein and G.H. McKinley. Extensional flow of a polysyrene boger fluid through a 4:1:4 axisymmetric contraction/expansion. *J. Non-Newtonain Fluid Mech.*, 86:61–88, 1999.

[99] G.C. Sawicki. *Wetting, Spreading, and adhesion*, pages 351–375. 1978.

[100] M.F. Schatz and G.P. Neitzel. Experiments on thermocapillary instabilities. *Annu. Rev. Fluid Mech.*, 33:93–127, 2001.

[101] Frisch H.L. Schonhorn, H. and T.K. Kwei. Kinetics of wetting of surfaces by polymer melts. *J. Appl. Phys.*, 37(13):4967–4973, 1966.

[102] L.E. Scriven and C.V. Sternling. The marangoni effects. *Nature*, 187:186–188, 1960.

[103] L.E. Scriven and C.V. Sternling. On cellular convection driven by surface-tension gradients: effects of mean surface tension and surface viscosity. *J. Fluid Mech.*, 19:321–340, 1964.

[104] N. Silvi and E.B. Dussan V. On the wetting of an inclined solid surface by a liquid. *Phys. fluids*, 28(1):5–7, 1985.

[105] M.K. Smith. Instability mechanisms in dynamic thermocapillary liquid layers. *Phys. fluids*, 29(10):3182–3186, 1986.

[106] M.K. Smith and S.H. Davis. Instabilities of dynamic thermocapillary liquid layers. part 1. convective instabilities. *J. Fluid Mech.*, 132:119–144, 1983.

[107] M.K. Smith and S.H. Davis. Instabilities of dynamic thermocapillary liquid layers. part 2. surface-wave instabilities. *J. Fluid Mech.*, 132:145–162, 1983.

[108] M.A. Spaid and G.M. Homsy. Viscoelastic free surface flows: spin coating and dynamic contact lines. *J. Non-Newtonian Mech.*, 55:249–281, 1994.

[109] M.A. Spaid and G.M. Homsy. Stability of newtonian and viscoelastic dynamic contact lines. *Phys. Fluids*, 8(2):460–478, 1996.

[110] L.H. Tanner. The spreading of silicon oil drops on horizontal surfaces. *J. Phys. D: Appl. Phys.*, 12:1473–1484, 1979.

[111] S.M. Troian, E. Herbolzheimer, S.A. Safran, and J.F. Joanny. Fingering instabilities of driven spreading films. *Europhys. Lett.*, 10(1):25–30, 1989.

[112] S.M. Troian, X.L. Wu, and S.A. Safran. Fingering instability in thin films. *Phys. Rev. Lett.*, 62(13):1496–1499, 1989.

[113] G. Udupa, M. Singaperumal, R.S. Sirohi, and M.P. Kothiyal. Characterization of surface topography by confocal microscopy: I. principles and the measurement system. *Measurement Science & Technology*, 11(3):305–314, 2000.

[114] G. Udupa, M. Singaperumal, R.S. Sirohi, and M.P. Kothiyal. Characterization of surface topography by confocal microscopy: I. principles and the measurement system. *Measurement Science & Technology*, 11(3):315–329, 2000.

[115] M.P. Valignat, N. Fraysee, A.M. Cazabat, and F. Heslot. Molecular newtworks in the spreading of microdroplets. *Langmuire*, 9:601–603, 1993.

[116] O.V. Voinov. Asymptote to the free surface of a viscous liquid creeping on a surface and the velocity dependence of the angle of contact. *Sov. Phys. Dokl.*, 23(12):891–893, 1978.

[117] M. Voué, S. Rovillard, J. De Coninck, M.P. Valignat, and A. M. Cazabat. Spreading of liquid mixtures at the microscopic scale: a molecular dynamic study of the surface-induced segregation process. *Langmuire*, 16:1428–1435, 1986.

[118] M. Voué, M.P. Valignat, G. Oshanin, A.M. Cazabat, and J. De Coninck. Dynamics of spreading of liquid microdroplets on substrates of increasing surface energies. *Langmuire*, 14:5951–5958, 1998.

[119] D.E. Weindner and L.W. Schwartz. Contact-line motion of shear-thinning liquids. *Phys. Fluids*, 6(11):3535–3538, 1994.

[120] S. Whitaker and R.L. Pigford. An approach to numerical differentiation of experimental data. *Ind. Eng. Chem.*, 52(2):185–187, 1960.

[121] T. Young. *Micelleous Works*, volume 1. Murray, London, 1855.